**Robert Teubenbacher, BSc**

# Determination of Spin-Axis Offset of a Fluxgate Magnetometer Using Data from the Electron Drift Instrument Onboard the Cluster Satellite

## MASTER THESIS

For obtaining the academic degree
Diplom-Ingenieur

Master Programme of
Technical Physics


**Graz University of Technology**

Supervisor:

Ao.Univ.-Prof. Dipl.-Ing. Dr.phil. Martin Heyn

Institute of Theoretical Physics

Graz, August 2013

Deutsche Fassung:
Beschluss der Curricula-Kommission für Bachelor-, Master- und Diplomstudien vom 10.11.2008
Genehmigung des Senates am 1.12.2008

## EIDESSTATTLICHE ERKLÄRUNG

Ich erkläre an Eides statt, dass ich die vorliegende Arbeit selbstständig verfasst, andere als die angegebenen Quellen/Hilfsmittel nicht benutzt, und die den benutzten Quellen wörtlich und inhaltlich entnommenen Stellen als solche kenntlich gemacht habe.

Graz, am …… ……..
(Unterschrift)

Englische Fassung:

## STATUTORY DECLARATION

I declare that I have authored this thesis independently, that I have not used other than the declared sources / resources, and that I have explicitly marked all material which has been quoted either literally or by content from the used sources.

…… ……..
date (signature)

# Contents

# List of Figures

# List of Tables

# Abbreviations

| | |
|---|---|
| **MHD** | **M**agnetohydrodynamics |
| **MMS** | **M**agnetospheric **M**ultiscale **M**ission |
| **FGM** | **F**luxgate **M**agnetometer |
| **EDI** | **E**lectron **D**rift **I**nstrument |
| **GDU** | **G**un **D**etector **U**nit |
| **TOF** | **T**ime **O**f **F**light |
| **CRF** | **C**ode **R**epitition **F**requency |
| **DPU** | **D**igital **P**rocessing **U**nit |
| **CPU** | **C**entral **P**rocessing **U**nit |
| **GSE** | **G**eocentric **S**olar **E**cliptic |
| **CAA** | **C**luster **A**ctive **A**rchive |
| **CDF** | **C**ommon **D**ata **F**ormat |
| **CEF** | **C**luster **E**xchange **F**ormat |

# Physical Constants

| | | | |
|---|---|---|---|
| Elementary charge | $e$ | = | $1.602\ 176\ 565\ 35 \times 10^{-19}$ C (exact) |
| Electron rest mass | $m_e$ | = | $9.109\ 382\ 154\ 4 \times 10^{-31}$ kg (exact) |
| Reduced Planck constant | $\hbar$ | = | $1.054\ 571\ 726\ 47 \times 10^{-34}$ J · s (exact) |
| Boltzmann constant | $k_B$ | = | $1.380\ 648\ 813 \times 10^{-23}$ J · K$^{-1}$ (exact) |
| Vacuum permittivity | $\epsilon_0$ | = | $8.854\ 187\ 817\ 620 \times 10^{-12}$ A$^2$ · s$^4$ · kg$^{-1}$ · m$^{-3}$ |
| Vacuum permeability | $\mu_0$ | = | $1.256\ 637\ 061\ 4 \times 10^{-6}$ kg · ms$^{-2}$ · A$^{-2}$ |

# Symbols

| | | |
|---|---|---|
| $q$ | electric charge | C |
| $r$ | radius | m |
| $T_{e,I}$ | electron/ion temperature | eV |
| $L_B$ | characteristic length (plasma) | m |
| $n_{e,I}$ | number density (electrons/ions) | quantity |
| $v_D$ | drift velocity | $\mathrm{m{\cdot}s^{-1}}$ |
| $g$ | Earth's standard acceleration | $\mathrm{m{\cdot}s^{-2}}$ |
| $\mathbf{P}_s$ | pressure tensor | $\mathrm{N{\cdot}m^{-2}}$ |
| $\mathbf{q}_s$ | heat flux | $\mathrm{W{\cdot}m^{-2}}$ |
| $R_m$ | magnetic Reynolds number | dimensionless |
| $T_g$ | gyroperiod | $\mu$s |
| $d$ | drift step | m |
| $T_{PN}$ | code period | |
| $\Delta$T | TOF offset | $\mu$s |
| $\Delta \mathrm{B}_z$ | spin-axis offset | nT |

| | | |
|---|---|---|
| $\Lambda$ | plasma parameter | quantity |
| $\nu$ | frequency | $s^{-1}$ |
| $\omega_{pe}$ | plasma frequency | $\mathrm{rad{\cdot}s^{-1}}$ |
| $\omega_c$ | cyclotron frequency | $\mathrm{rad{\cdot}s^{-1}}$ |
| $\tau_n$ | electron-neutral collision time | s |
| $\lambda_D$ | Debye length | m |
| $\beta$ | plasma beta | dimensionless |
| $\Delta$ | code chip length | |
| $\sigma$ | standard deviation (TOF) | $\mu$s |

*I would like to express my deepest gratitude to my adviser Prof. Martin Heyn at Graz University of Technology and my advisor Dr. Rumi Nakamura at the Space Science Institute of the Austrian Science Academy. Their guidance and support were invaluable in the process of this thesis.*

*Special thanks to my colleagues at the Space Science Institute for their assistance at my first steps with IDL and the poster presentation. I also want to thank Edita Georgescu and Lukas Giner for providing the reading tools for the data used in this thesis.*

*Furthermore, I want to thank my parents Hubert and Anna for their continuous support. It would not have been possible without their help. I also want to thank my grandfather Lorenz for always believing in me, no matter what.*

*My special thank goes to my sister Carmen for her expertise in the correction process of the thesis.*

*Additionally, i want to thank my friends for their support during my studies.*

*At last I want to thank my wife Miriam for encouraging me, supporting me and sometimes enduring me.*

*"per aspera ad astra"*
*(Seneca)*

# Chapter 1

# General descriptions

## 1.1 The geomagnetic field

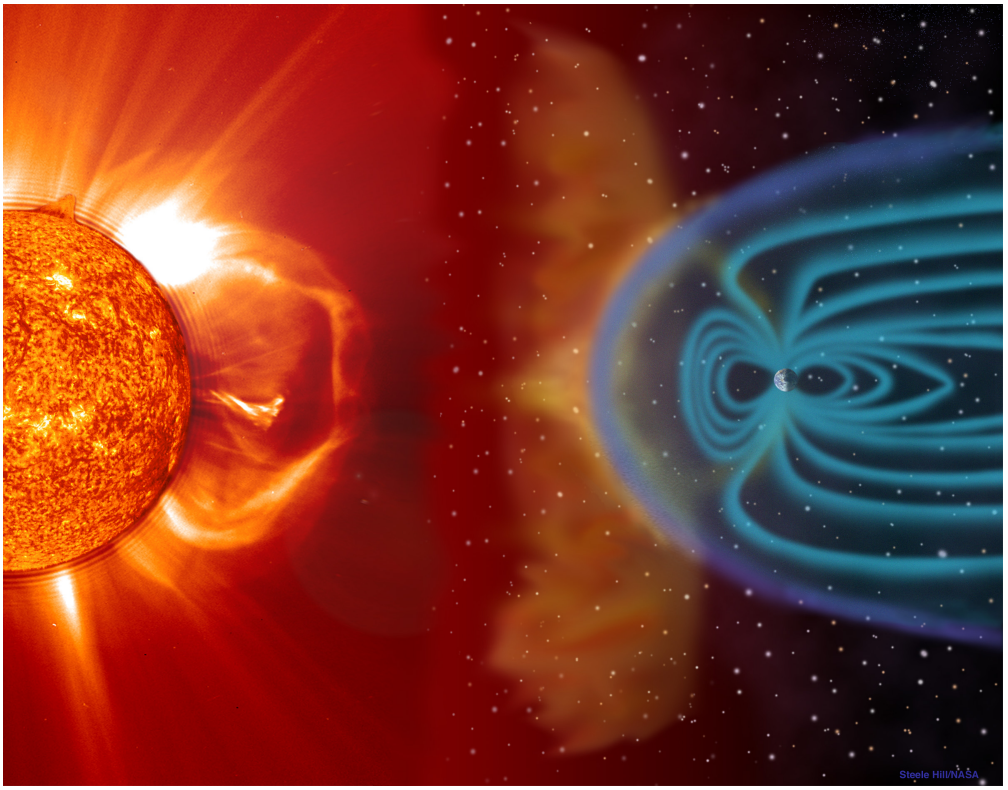


**Figure 1.1:** Artwork of earth's magnetic field interacting with the solar wind[1]

The earth's magnetic field can be described by a dipole field. It encompasses earth and extends into space. On the direction facing the solar wind the field extends to 10 - 12 earth radii and on the opposite side approximately 1000 earth radii. The field is a

result of the dynamo mechanism. Due to earth's rotation, molten metals in the outer core hold different rotational speeds. Furthermore, these molten metals are electrical conducts. As a result of the electrical currents a corresponding magnetic field is formed. The kinetic energy of the currents is transferred into magnetic field energy. Figure 1.1 displays an artwork of interaction of the magnetic field with the solar wind [17, p. 88-89].

**Solar wind** The solar wind consists of electrons, protons and to some extend of helium. This mixture forms a plasma, that is emanated from the sun surface with a speed of 400 km/s. Because of its high conductance the plasma can bind the weak magnetic field lines of the sun (see below Reconnection: frozen in condition). Therefore, the sun's magnetic field is transmitted throughout the whole solar system. For that reason the magnetic field is called interplanetary magnetic field. As a result of the sun's rotation the magnetic field lines have the shape of a spiral with the sun at the center of the spiral. Figure 1.2 depicts the spiral form of the interplanetary magnetic field lines. The dashed line in the Figure represents earth's orbit. The impinging magnetic field lines interact with earth's magnetic field resulting in the deformation of the dipole field [2, p. 8-9], [3, p. 5ff].

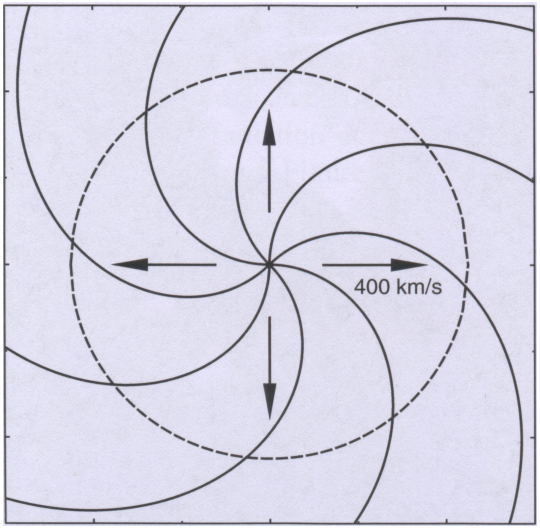


**Figure 1.2:** Spiral shape of the solar wind as a result of the sun's rotation [2, p. 8]

**Earth's magnetic field** The interaction of the solar wind with earth's magnetic field is depicted in Figure 1.3. The plasma transported in the solar wind impinges on earth's magnetic field and is slowed down abruptly. To achieve that sudden reduction in velocity of the solar wind particles energy has to be spent by the magnetic field. This leads to the deformation of the side of the magnetic field facing the solar wind. The region of that interaction is called the bow shock. Depending on the intensity of the solar wind the bow shock is located 14 - 16 earth radii from earth. The particles slowed down at

the bow shock accumulate in a layer called the magnetosheath. It is a layer, ranging between the bow shock and the magnetosphere, filled with plasma of the solar wind. The density, the magnetic field strength and the temperature of the plasma is substantially higher than the solar wind plasma. The boundary layer between the magnetosheath and the magnetosphere is called the magnetopause. In Figure 1.3 the outer dashed line marks the location of the magnetopause. The interplanetary magnetic field lines, holding the plasma are deflected along the magnetopause by the magnetosphere. The magnetosphere forms a cavity in the solar wind, that the interplanetary magnetic field lines cannot penetrate. As mentioned above, the magnetic field facing the solar wind is deformed resulting in the clinching of the field. The dimension of the field is around 10 - 12 earth radii. On the opposite side the magnetic field is elongated. The solar wind stretches the field resulting in the formation of the magnetotail. The dimensions of the magnetotail reach out up to 1000 earth radii, even reaching the moon. The plasma in the magnetotail is cumulated in an area of 10 earth radii. It is called the plasma sheet. In the region called the tail lobe the plasma sheet dimension thins out that much, that field lines of opposite directions approach each other. In Figure 1.3 these magnetic field lines are separated by the neutral sheet. At the point when the neutral sheet becomes thin enough the field lines can interact. The resulting process, where these lines are reconnected and magnetic field energy is converted to kinetic energy of the plasma particles is called reconnection [2, p. 9-10], [2, p. 5ff], [17, p. 88-89].

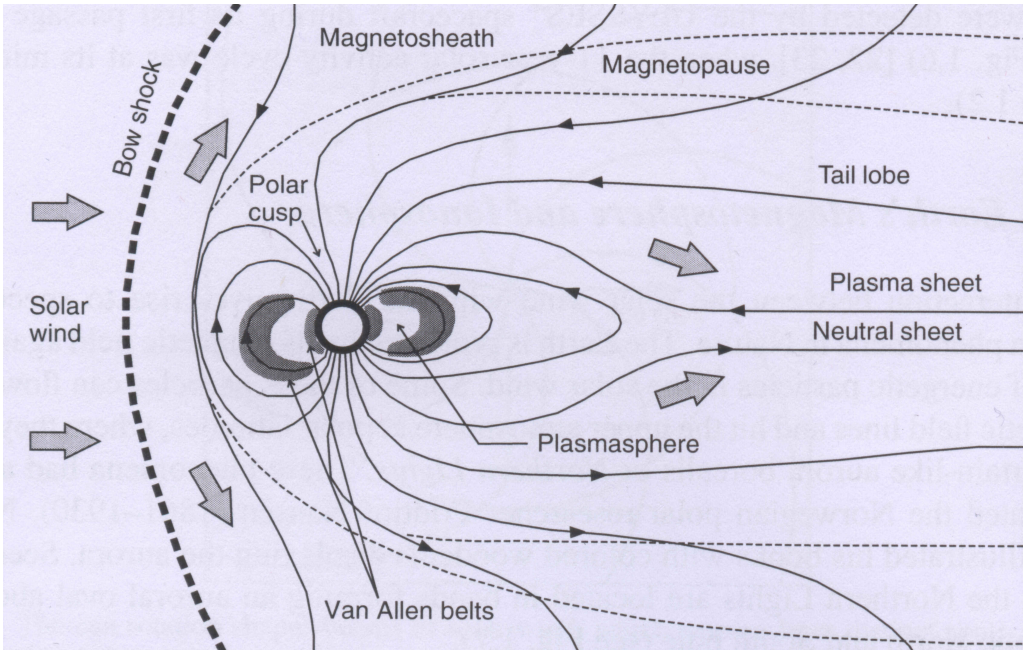


**Figure 1.3:** The interaction of earth's magnetic dipole field with the solar wind [2, p. 10].

**Magnetosphere and magnetic currents** The magnetosphere contains different kinds of regions filled with plasma. They differ from each other by their density, temperature and constitution. The main constituents are electrons and protons, originating in the solar wind and the ionosphere. The ionosphere can either be counted towards earth's atmosphere or towards the charged regions of the magnetosphere. If one considers that the atmosphere only consists of neutral particles the ionosphere is a separate layer. Otherwise, the ionosphere is part of the thermosphere. The ionosphere ranges from an altitude of 80 km to 500 km above earth's surface. The charged particles of the ionosphere are a result of the UV radiation emitted by the sun which ionizes the particles. Because of a low particle density recombination hardly ever happens resulting in the ionized layer. The ionosphere consists of electrons, protons, $He^+$ ions and $O^+$ ions. On average, the electron density is about $10^5$ cm$^{-3}$ and the electron temperature is about $10^3$ K. The corresponding magnetic field strength of the ionosphere is about $10^4$ nT. At higher altitudes the ionosphere passes over into the plasmasphere. The plasmasphere shown in Figure 1.3 has the form of a torus. It is enclosed by the radiation belts (Van Allen belts). The plasma in the plasmasphere originates in the ionosphere. The electron density is about $5 \cdot 10^2$ cm$^{-3}$ and an electron temperature of about $5 \cdot 10^3$ K. The plasmasphere is adjacent to the radiation belts and is separated by the plasmapause. Particles in the radiation belts are trapped and are moving back and forth along the magnetic field lines (magnetic mirror). At a given altitude particles of the plasma sheet can move along magnetic field lines and end up at the polar region. There they interact with neutral layers of the atmosphere resulting in an ionisation process followed by photon emission. The photon emission is called the aurora borealis (northern hemisphere) or the aurora australis (southern hemisphere). Magnetic field lines connecting the poles with the tail lobe are concentrated at the polar cap. The polar cap is located a the center of the aurora oval. The oval is a ring structure around the polar cap, where the interaction leading to the aurora lights takes place. Particles in the plasma move along the magnetic field lines. As long as the charges are equal their movement has no effect on the magnetic field. But if negative and positive charges move in different directions along the field lines an electric current is created. This electric current on the other hand forms a magnetic field that interacts with the magnetosphere, therefore changing its structure. As depicted in Figure 1.4 there are different currents within the magnetosphere. These currents determine the dynamics within the magnetosphere by transporting charge, mass, momentum and energy. Furthermore, as mentioned before they have a great influence on the shape of the magnetosphere. The compression at the side facing the solar wind is accompanied by the magnetopause current. The tail lobe on the opposite side is enclosed by the tail current. In the center of the plasma sheet lies the neutral sheet. The neutral sheet contains the neural sheet current. Another current is located within the radiation belt, which is called the ring current. The ring current is the result of the drift motion of the charged particles, which leads them around earth. The drift motion is different for electrons and protons resulting in different flow directions. The currents called field-aligned currents depicted in Figure 1.3 connect smaller currents

in the ionospheric region with the magnetosphere ensuring an exchange between them [3, p. 5ff].

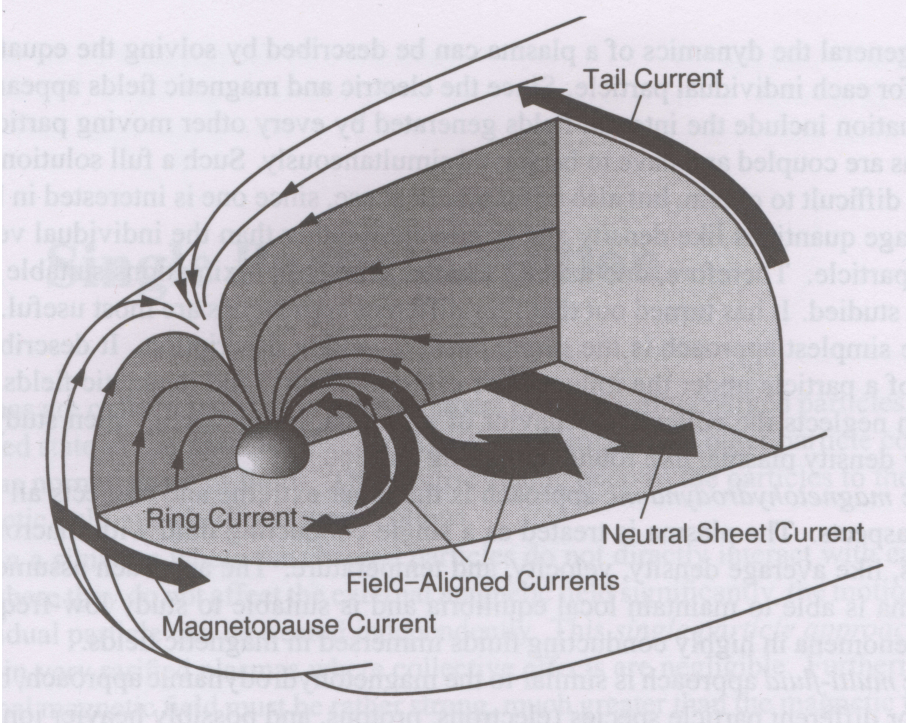


**Figure 1.4:** Magnetic currents in earth's magnetic field.[3, p. 9]

## 1.2 Theoretical Approach

This section quotes the theoretical background necessary for this thesis. The section is based on two books: Plasma physics by Alexander Piel and Basic Space Plasma Physics by Baumjohann and Treumann. From the book Plasma physics chapters one, two, three, five and nine were used. From the book Basic Space Plasma Physics chapters one, two, four, five, six and seven were used for this section.

### 1.2.1 Basic Plasma definitions

**What is Plasma?** The plasma state is the fourth state of matter. The state consists of a gaseous mixture of negatively charged particles, the electrons, and positively charged particles, the ions. The number of electrons and ions is approximately the same. Different types of plasma can be distinguished by the order of its ionization. In a fully ionized plasma there are no neutral atoms left. The plasma consists either of electrons or ions. This type of plasma can be observed in the sun. On the other hand partly

ionized plasma still contains some neutral atoms. Figure 1.5 below depicts the different kinds of plasma that can be observed in nature or created artificially in a laboratory.

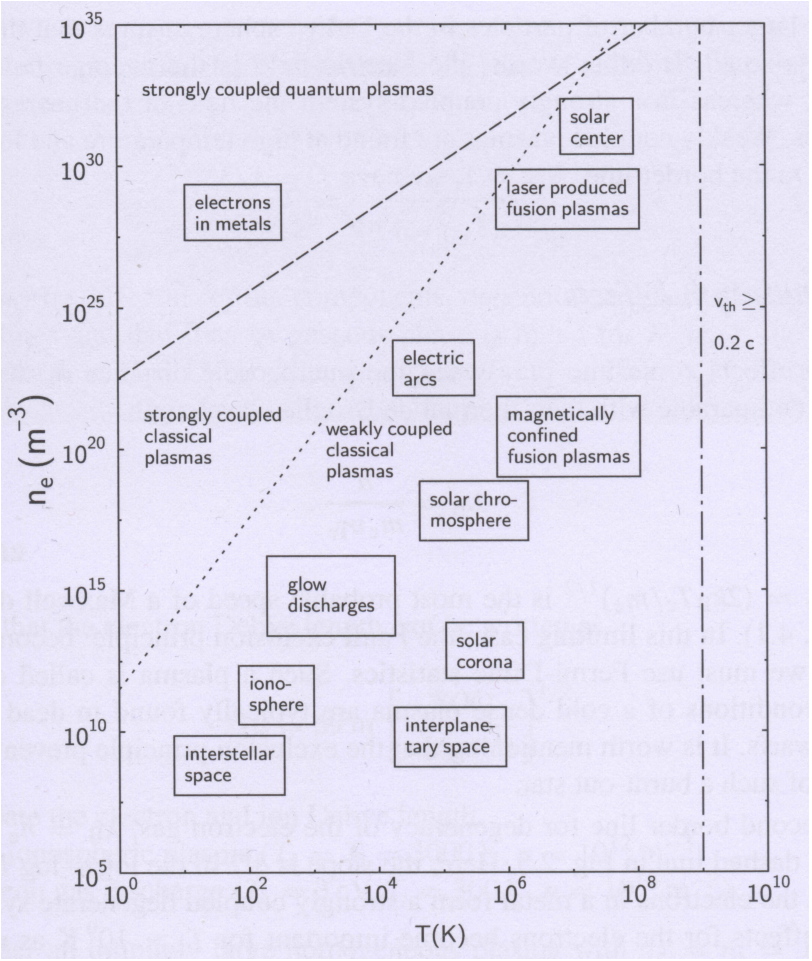


**Figure 1.5:** Different types of plasma and their interdependency of number density and temperature [2, p. 40].

The particles in the plasma interact with each other by transferring part of their kinetic energy to other particles, which leads depending on the energy to their ionisation. This kind of ionisation occurs at high temperatures, where the ionisation energy ranges between 3 eV to 25 eV. Another possible way of ionisation is photoionisation. In that case the ionisation energy is provided by the energy of the photons. This process needs a source of radiation in the UV spectral range. Both ionisation processes possess a reciprocal process. These two processes are depicted below with their respective recombination processes. Each of these processes occur continuously when the plasma is in thermodynamic equilibrium.

Collisonal ionisation: $e + P \rightarrow P^+ + 2e$

Three body recombination: $P^+ + 2e \rightarrow P + e$

Photoionisation: $h\nu + P \rightarrow P^+ + e$

Two body recombination: $P^+ + e \rightarrow P$

The following properties have to be satisfied that a specific volume with charged particles can be called a plasma.

**Quasineutrality and Debye shielding** As described in the paragraph above, a plasma is comprised of charged particles. For any of the following considerations the number of electrons $n_e$ and ions $n_i$ per volume element is equal, hence $n_e = n_i$. The dimension of the volume has to satisfy two conditions. Firstly, it must be large enough to contain a sufficient amount of particles. Secondly, it dimension must be small compared to the characteristic length L of the plasma. This characteristic length L is the length within the macroscopic quantities, like temperature and density, change. On a macroscopic scale the plasma is neutral, which is the result of the neutrality of each single volume element. This yields the definition of quasineutrality. For scales bigger than the dimension of the volume element the plasma is neutral. Therefore, the potential of each single charged particle in the volume element must be neutralised. This leads to the term of Debye shielding. Under normal circumstances each particle has a Coulomb potential. The Coulomb potential decreases with $\frac{1}{r}$. Although the potential decreases over distance, its effect won't vanish for distances smaller than the dimension of the volume element to govern charge neutrality. However, the interaction with other charges in the plasma leads to an adjustment of the Coulomb potential that is described by the Debye potential. The interaction with other particles is called the Debye shielding. Figure 1.6 depicts the difference between the Coulomb potential and the Debye potential. The Coulomb potential and Debye potential are described by the two equations 1.1 and 1.2 below the Figure. Coulomb potential:

$$\Phi_C = \frac{q}{4\pi\epsilon_0 r} \tag{1.1}$$

Debye potential:

$$\Phi_D = \frac{q}{4\pi\epsilon_0 r} \cdot \exp(-\frac{r}{\lambda_D}) \tag{1.2}$$

If one considers equation 1.2 one can see, that the newly formed potential is the Coulomb potential multiplied by an exponential factor. This exponential factor contains a specific length, called the Debye length $\lambda_D$. If this length is smaller than the distance r, then the effect of the potential vanishes rapidly(see Figure 1.6). The Debye length is the radius of the volume element. The corresponding volume element is called a Debye sphere. Within the sphere charge separations take place. However, these processes are balanced by their resulting electric fields. These charge separations are caused by the thermal energy of the particles. Therefore the Debye length is dependent on the temperature. Figure 1.7 depicts the interaction of positively and negatively charged particles with a single positive charge at two different temperatures. In the left part of the Figure the case for low temperature is shown. The kinetic energy of the particles is low. Electrons and ions can get close to the charge in the center. On their trajectories they get deflected

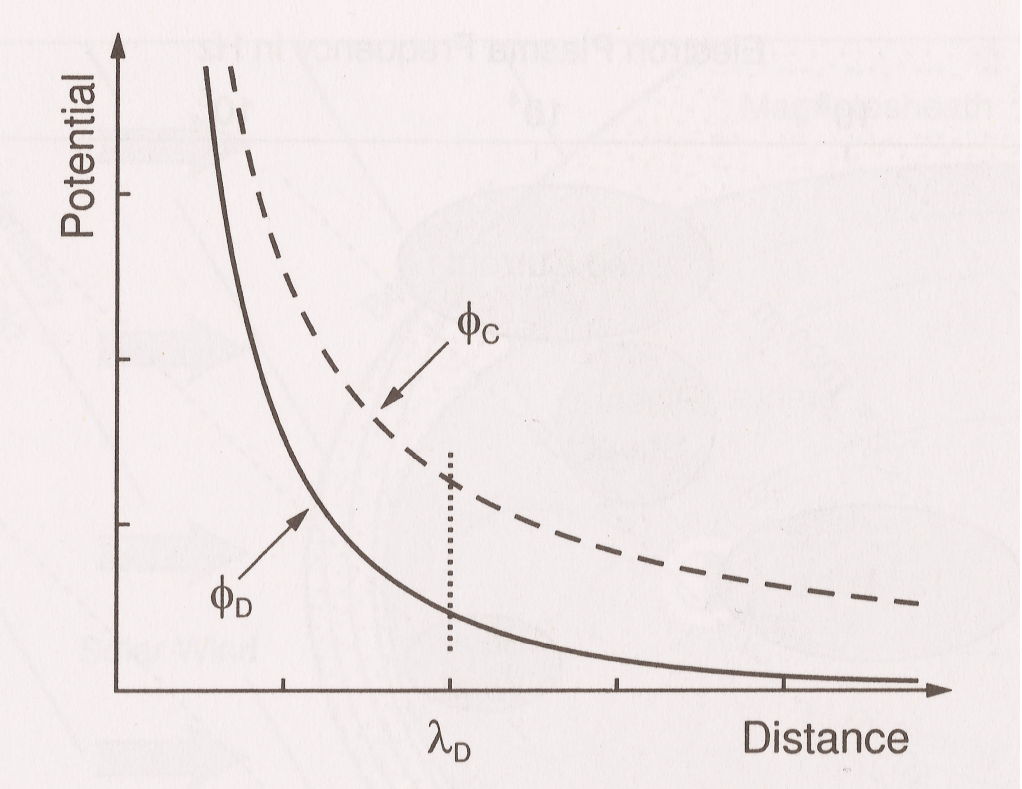


**Figure 1.6:** Coulomb potential and Debye potential [3, p. 3].

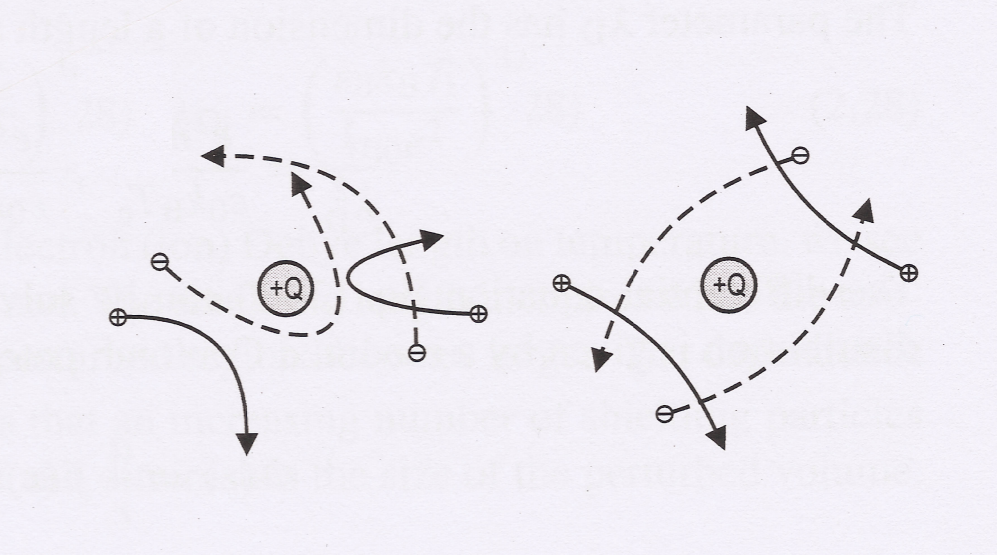


**Figure 1.7:** Trajectories of charged particles around a central charge at different temperatures [2, p. 52].

or reflected by the central charge. The shielding effect is significant. The right part of Figure 1.7 depicts the case of higher temperature, thus the kinetic energy of the particles is higher. Depending on the charges of the particles their trajectories are bend towards or away from the central charge. Both kind of trajectories are stiffer in comparison to the first case of Figure 1.7. Because of higher temperatures the magnitude of the shielding effect is less developed. The dependence of the Debye length of the temperature can be comprehended by examining the equation 1.3 , the definition of $\lambda_D$.

$$\lambda_D = (\frac{\epsilon_0 k_B T_e}{n_e e^2})^{1/2} \tag{1.3}$$

Here $\epsilon_0$ is the free space permittivity, $k_B$ is the Boltzmann constant, $T_e$ the electron temperature, $n_e$ electron density and $e$ elementary electron charge. The Debye length can also be defined for ions. In that case the temperature, number density and charge have to be replaced by the corresponding quantity for the ions. The equation 1.3 only describes the case for electrons. If one has to consider both electrons and ions the following equation determines the overall Debye length. For simplicity only the Debye length is displayed as a squared quantity.

$$\frac{1}{(\lambda_D)^2} = \frac{1}{(\lambda_{De})^2} + \frac{1}{(\lambda_{Di})^2} \tag{1.4}$$

To distinguish a plasma from any ionised gas, like a flame, the considered volume of charged particles has to satisfy the first plasma criterion. As mentioned at the beginning of the paragraph, for a system like a plasma there is a characteristic length L. This length must be much larger than the Debye length $\lambda_D$.

$$\lambda_D << L \tag{1.5}$$

So all the macroscopic variations of temperature or density take place in a great number of volume elements.

**Plasma parameter** For the definition of the Debye sphere there were two conditions that had to be satisfied. The first of those conditions was the second criterion for a plasma. Within the Debye sphere there have to be sufficient charged particles. This yields another quantity for the description of plasma, the plasma parameter $\Lambda$.

$$\Lambda = n_e \cdot \lambda_D^3 \tag{1.6}$$

Here the plasma parameter is expressed for the case of electrons. It should be mentioned that the value of $\Lambda$ is different for ions. The parameter states whether the plasma is weakly or strongly coupled. An ideal plasma is weakly coupled. Therefore, the following statement describes the weakly coupled states:

$$\Lambda >> 1 \tag{1.7}$$

In case of a weakly coupled plasma the electric field within the Debye sphere is the averaged field over many particles. In the case of a strongly coupled plasma the electric field of the nearest neighbour has the most influence. The border between weakly and strongly coupled plasma is at $\Lambda = 1$.

**Plasma frequency** If the plasma is exposed to a brief electric field electrons and ions experience a force. Because of their lower mass the electrons respond to the field with relative motion to the ions. As a result a charge separation emerges and the charge neutrality is violated. The response is a retracting force on the electrons because of an electric field originating in the charge separation. Due to inertia this process continues. The electrons oscillate around an equilibrium position. The frequency of this oscillation is called the electron plasma frequency $\omega_{pe}$.

$$\omega_{pe} = (\frac{n_e e^2}{m_e \epsilon_0})^{1/2} \tag{1.8}$$

In equation 1.8 $m_e$ is the mass of the electron, e is the elementary electron charge, $n_e$ the electron density and $\epsilon_0$ is the free space permittivity. The plasma frequency yields the third criterion for a plasma. In the case of a plasma that is not totally ionised, there are still some neutral particles within the plasma. This leads to the quantity $\tau_n$, the duration between electron neutral collisions. For a plasma the following conditions must be satisfied(third criterion):

$$\omega_{pe} \cdot \tau_n >> 1 \tag{1.9}$$

### 1.2.2 Plasma models

#### 1.2.2.1 Single particle model

In the single particle model the motion of a single particle within the plasma is observed. The particle does not interact with other particles, nor does it have a significant effect on an external magnetic field. This consideration is only acceptable, if the external magnetic field is of great magnitude and any collective effects of the plasma can be disregarded. Before considering the motion of the single particle one has to make a distinction between an unmagnetized and a magnetized plasma. The motion of the particles in the unmagnetized plasma is only governed by electric fields and collisions between the particles. In the case of a magnetized plasma an external magnetic field and an electric field interact with the particles and shape their trajectories. So most of the effects that are described in the following paragraphs refer to a magnetized plasma. The basis for the description of the trajectory of a single particle is Newton's equation of motion. According to this equation the particle experiences a force. The force acting on a moving charged particle is call the Lorentz force. It describes the interaction of a particle with an electric and magnetic field. Formula 1.10 depicts Newton's equation of

motion. Here m is the mass of the charged particle , $\dot{\mathbf{v}}$ is the acceleration resulting from the acting force, q is the charge of the particle, **E** is the electric field, **v** is the velocity of the particle and **B** is the magnetic field.

$$m\dot{\mathbf{v}} = q(\mathbf{E} + \mathbf{v} \times \mathbf{B}) \tag{1.10}$$

During the next step the electric field E is disregarded. The magnetic field B is directed along the z-axis. Therefore, the B field has no components acting along the x or y direction. In addition, the magnetic field does not change its magnitude along the z-axis(homogeneous). A particle that is injected into that set-up will start to spin around the magnetic field lines in a circular motion, as long as the acceleration component $\dot{v_z}$ is zero. The other components in the x and the y direction of the acceleration are displayed in formula 1.11 and 1.12.

$$\dot{v_x} = v_y \frac{q}{m} B_z \tag{1.11}$$

$$\dot{v_y} = -v_x \frac{q}{m} B_z \tag{1.12}$$

By taking the second derivative of either one of those two equations, one would get the equation of the harmonic oscillator. Considering the x direction this would lead to:

$$\ddot{v_x} = -(\frac{q}{m} B_z)^2 v_x \tag{1.13}$$

The squared part on the right hand side of equation 1.13 yields the cyclotron frequency.

$$\omega_c = \frac{|q|}{m} B_z \tag{1.14}$$

This quantity makes it possible to calculate the radius of the charged particle on its way around the magnetic field lines. This radius is called Larmor radius.

$$r_L = \frac{v_\perp}{\omega_c} \tag{1.15}$$

Here $v_\perp$ is the component of the velocity perpendicular to the Larmor radius. The solution of equation 1.13 is:

$$x - x_{center} = r_L \sin \omega_c t. \tag{1.16}$$

The variable $x_{center}$ is the position of the center of the circular trajectory. In Figure 1.8 the motion of negatively and positively charged particles is displayed in the upper part of the Figure. Electrons move counter clockwise around the field lines, whereas ions move clockwise on their circular trajectory. In the lower part of the Figure the charged particle has a non zero $v_z$-component. Therefore, the trajectory of the particle has the form of a helix. Now one can also consider additional forces that are acting on the charged particle. The effect of additional forces is that the circular motion of the particle around the magnetic field lines experiences a drift motion. This drift motion depends on the

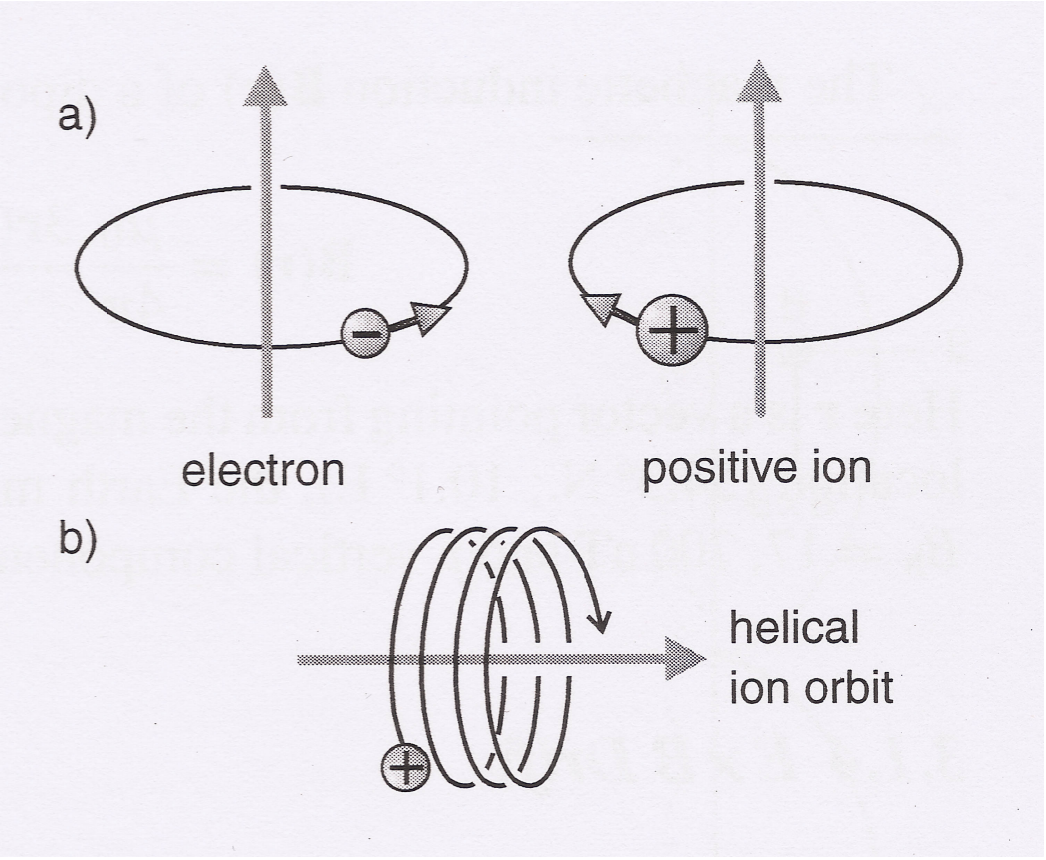


**Figure 1.8:** Different interactions of charged particles with a magnetic field. (a) Electron gyrate anticlockwise, positive ions gyrate clockwise. (b) Helical gyration of an ion along a magnetic field line [2, p. 47].

type of force. The electric field as stated in the definition of the Newton's equation of motion is a part of the Lorentz force. Hence, as an additional force the action of the electric field on the charged particle, which results in a force action, will be elaborated on the first paragraph. Before discussing drift motion in greater detail one should take a quick look at the idea of the guiding center. In this concept the particle motion and the drift motion are regarded separately. So the particle is gyrating around the magnetic field lines on a circular trajectory. If the velocity component of the particle along the field lines is zero, the motion of the particle can be considered to be in a plane. The drift describes the motion of the centre of the circular trajectory (guiding center) in a specific direction within this plane. The separation into the circular motion of the particle around the guiding center and the motion of the guiding center itself yields a simpler view.

**$\mathbf{E} \times \mathbf{B}$ - drift:** In the case of the $E \times B$ drift the electric field is considered to be non zero. It can be assumed that the **E** has a component parallel to and a component perpendicular to **B**. The component $E_{||}$ has an action parallel to **B**. Negatively and positively charged particles will be accelerated into opposite directions. This leads to

a charge separation, which results in another electric field. The field generated by the charge separation will be cancelling out the $E_{||}$ field component. The perpendicular field component $E_{\perp}$ will contribute to the motion of the particles. The next step is to determine the trajectory of the particle. As described in the paragraph above this is accomplished by validation of Newton's equations of motion. Because of the considerations done for the $E_{||}$ the z-component of equation 1.10 can be neglected.

$$\dot{v_x} = \frac{q}{m}(E_x + v_y B z) \tag{1.17}$$

$$\dot{v_y} = \frac{q}{m}(-v_x B_z) \tag{1.18}$$

Now one has to take the second derivative again and the result are two equations of motion. The first one for the x-component describes the motion of a harmonic oscillator. The second one for the y-component includes a term that leads to a velocity in the negative y-direction. The factor $\omega_c$ is the cyclotron frequency.

$$\ddot{v_x} = -\omega_c^2 v_x \tag{1.19}$$

$$\ddot{v_y} = -\omega_c^2 (v_y + \frac{E_x}{B_z}) \tag{1.20}$$

The solutions of equations 1.19 and 1.20 are as followed:

$$v_x = \frac{E_x}{B_z} \sin \omega_c t \tag{1.21}$$

$$v_y = \frac{E_x}{B_z} (\cos \omega_c t - 1) \tag{1.22}$$

The motion displayed by these two solutions describes the superposition of two separate motions. The first motion is a circular motion equal to the case, where only the magnetic field is considered. The second part of the motion is a drift motion perpendicular to the **E** and **B** fields. Written in the vector notation this drift velocity is

$$v_E = \frac{\mathbf{E} \times \mathbf{B}}{B^2}. \tag{1.23}$$

The drift motion is independent of the charge of the particle. Unlike in the case of the gyration motion in the magnetic field the ions and electrons move in the same drift direction.

**Gradient drift:** In the first part of this section the magnetic field was considered to be of a homogeneous form. This lead to the circular motion of the particle around the magnetic field lines. In most cases the magnetic field is not homogeneous, therefore one has to consider the case of an inhomogeneous magnetic field. The result of this inhomogeneity is the action of the magnetic gradient on the particle. Without the

gradient the force acting on the particle is described by the equation

$$m\dot{\mathbf{v}} = q(\mathbf{v} \times \mathbf{B}) \tag{1.24}$$

The magnetic field regarded in this consideration is at the center of the circular motion of the particle, at the guiding center. In the case of an inhomogeneous magnetic field the field changes in magnitude depending on the distance to the guiding center. As a result, the magnetic field magnitude is different at the location of the particle. Furthermore, the magnetic field vector can be expanded in a Taylor series as long as the dimension of the change of the magnetic field gradient is much larger than the distance of the particle to the guiding center.

$$\mathbf{B} = \mathbf{B_{GC}} + (\mathbf{r} \cdot \nabla)\mathbf{B_{GC}} \tag{1.25}$$

In equation 1.25 $\mathbf{B_{GC}}$ is the magnetic field at the guiding center and $\mathbf{r}$ is the distance of the particle to the guiding center. In the next step the magnetic field is put into equation 1.24.

$$m\dot{\mathbf{v}} = q(\mathbf{v} \times \mathbf{B_{GC}}) + q(\mathbf{v} \times (\mathbf{r} \cdot \nabla)\mathbf{B_{GC}}) \tag{1.26}$$

As done in the previous paragraphs the motion can be separated into gyration and drift. This can be achieved by considering the velocity $\mathbf{v}$ as the sum of a gyration dependant part $\mathbf{v_G}$ and a drift dependant part $\mathbf{v_D}$. Here the drift dependant part is a result of the magnetic gradient. Additionally the condition $\mathbf{v}_G >> \mathbf{v}_D$ has to be considered. Taking this condition into account and, on the one hand, neglecting terms that describe terms of the motion in a homogeneous field and, on the other hand, terms that are very small compared to the others will result in the following equation:

$$m\dot{\mathbf{v}}_D = q(\mathbf{v_D} \times \mathbf{B_{GC}}) + q(\mathbf{v_G} \times (\mathbf{r} \cdot \nabla)\mathbf{B_{GC}}) \tag{1.27}$$

Because the motion of the particle is observed for time periods much larger than one single gyration, it is possible to average over one gyration. On its trajectory through the spatial varying magnetic field the particle is accelerated in the high field and decelerated in the low field. On average, the change in drift velocity is zero. Therefore, the left side of equation 1.27 regarding the temporal alteration of the drift velocity disappears. To get a form similar to equation 1.23, one takes the cross product with $\frac{\mathbf{B}_{GC}}{B_{GC}^2}$ of equation 1.27.

$$\mathbf{v}_D = \frac{1}{B_{GC}^2}\langle(\mathbf{v}_G \times (\mathbf{r} \cdot \nabla)\mathbf{B}_{GC}) \times \mathbf{B}_{GC}\rangle \tag{1.28}$$

Now one can choose the direction of the magnetic field vector, either in the x- or the y-direction. By choosing the x-direction this results in:

$$\mathbf{v}_D = -\frac{1}{B_{GC}^2}\langle \mathbf{v}_G x \frac{d}{dx}(\mathbf{B_{GC}})\rangle \tag{1.29}$$

By using the solutions for x (1.2.2.1) and taking the average over a gyration, one would get the drift velocity. By choosing the magnetic field vector to change along the x-direction the drift velocity is directed in the y-direction and vice versa.

$$\mathbf{v}_D = \pm \frac{v_\perp r_G}{2\mathbf{B_{GC}}} \frac{d}{dx}(\mathbf{B_{GC}})\mathbf{e}_y \tag{1.30}$$

Here the factor $\frac{1}{2}$ is a result of the averaging. The sign depends on the charge of the particle. In Figure 1.9 the motion of negative and positive charges is displayed. The general form of the drift velocity is:

$$\mathbf{v}_D = \frac{mv_\perp^2}{2qB^3}(\mathbf{B} \times \nabla \mathbf{B}) \tag{1.31}$$

[3, p.18-20],[2, p. 51-52]

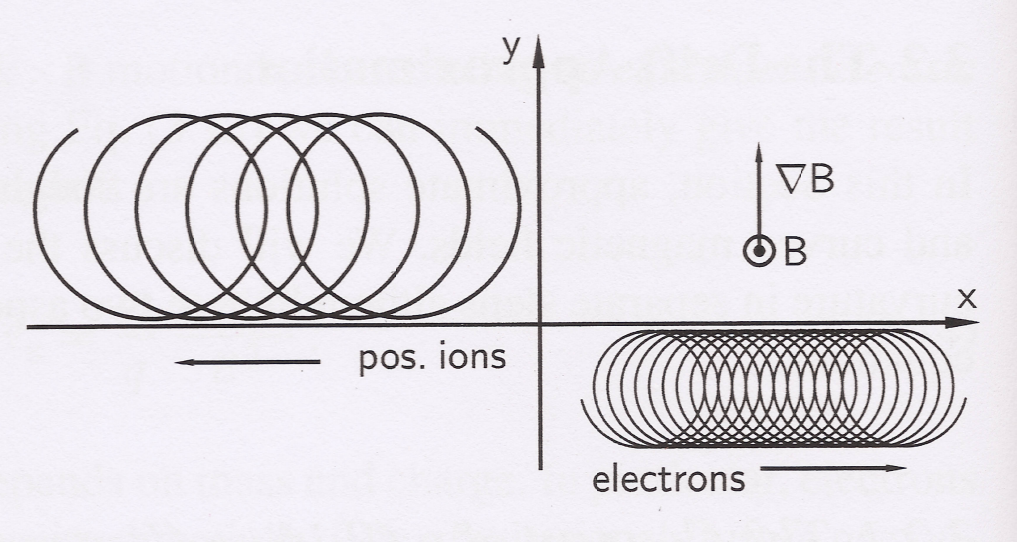


**Figure 1.9:** Gradient drift of positive and negative charges [2, p. 52].

**Polarisation drift:** The fields described in the paragraphs above were time-independent. The polarisation drift results because of a time dependent field. In this case the electric field **E** is time-dependent. The **E** - and **B** - field are perpendicular to each other. The electric field is directed along the x-axis and the magnetic field is directed along the z-axis. This leads to the equation of motion, which is equal to the Lorentz force equation, except for the time dependent electric field $\mathbf{E}(t)$.

$$\dot{\mathbf{v}} = \frac{q}{m}(\mathbf{E}(t) + \mathbf{v} \times \mathbf{B}) \tag{1.32}$$

As for these considerations the electric field changes with a constant rate. In the next step one forms the cross product with $\frac{\mathbf{B}}{B^2}$. This leads to:

$$\frac{m}{qB^2}\frac{d}{dt}(\mathbf{v}\times\mathbf{B}) = \frac{\mathbf{E}\times\mathbf{B}}{B^2} + \frac{(\mathbf{v}\times\mathbf{B})\times\mathbf{B}}{B^2} \tag{1.33}$$

For the last term on the right side of the equation above one has to apply an algebraic relation for the cross product (see Appendix), which leads to:

$$\mathbf{v} - \frac{\mathbf{B}(\mathbf{B}\cdot\mathbf{v})}{B^2} = \frac{\mathbf{E}\times\mathbf{B}}{B^2} - \frac{m}{qB^2}\frac{d}{dt}(\mathbf{v}\times\mathbf{B}) \tag{1.34}$$

The left side of the equation can be associated with the perpendicular drift velocity $\mathbf{v_D}$. Because of averaging over one gyration any changes that are in a time scale smaller than the gyration itself can be ignored. The first term on the right equals the velocity of the $\mathbf{E}\times\mathbf{B}$-drift. The cross product of the last term on the right can be written as an electric field. These considerations lead to:

$$\mathbf{v}_D = \mathbf{v}_E + \frac{1}{\omega_c B}\frac{d}{dt}(\mathbf{E}_\perp) \tag{1.35}$$

The last term on the right side is called the polarization drift. The difference between the $\mathbf{E}\times\mathbf{B}$-drift and the polarization drift is that the latter is dependent on the mass of the particle. The bigger the mass of the particle the higher the drift velocity. Furthermore, the charges are separated along the changing electric field. This yields in a current, which polarizes a plasma[3, p.16-17],[2, p. 60-61].

**Gravitational drift:** As mentioned at the beginning of this section, any force that acts on a particle can lead to a drift motion. This is even true for gravity. To take gravity into account equation 1.24 is complemented with the gravitational force. The result is the equation of motion incorporating gravity.

$$m\dot{\mathbf{v}} = q(\mathbf{v}\times\mathbf{B}) + m\mathbf{g} \tag{1.36}$$

Here $\mathbf{g}$ is the gravitational acceleration. A simple way to derive the drift velocity is to use the equivalent electric force to the gravitational force.

$$q\mathbf{E} = m\mathbf{g} \tag{1.37}$$

In the next step this equation is evaluated to obtain the electric field and the resulting equation is inserted into equation 1.23. The result is the equation for the gravitational drift:

$$\mathbf{v}_{gravity} = \frac{m}{q}\frac{\mathbf{g}\times\mathbf{B}}{B^2} \tag{1.38}$$

The gravitational drift depends on the mass and the charge. Therefore, negative and positive charges move in opposite directions. Within earth's magnetosphere the gravitational drift results in the formation of an equatorial net electric current[2, p. 49-50].

#### 1.2.2.2 Kinetic Model

In the single particle model the interaction with other particles was neglected. Therefore, a model has to be found that considers interactions with other particles. The kinetic model is not confined to the perspective of one single particle. It describes the motion of a great number of particles and their interaction with each other. Before introducing the interactions the motion of the particles has to be set into a workable framework. This is done by the characterisation of the location and velocity of every single particle at any given time. This characterisation leads to the definition of the phase space. The phase space is a six dimensional space. The coordinates of a particle are specified by a set of spatial coordinates $\mathbf{x}(t)$ and a set of velocity coordinates $\mathbf{v}(t)$, which are all time-dependent. These two quantities are independent of each other. So for every time t there is a point in the phase space for a single particle. The series of consecutive times t leads to the definition of the phase trajectory of a particle. A way to describe a particle in the phase space is by its exact number density:

$$F_i(\mathbf{x}, \mathbf{v}, t) = \delta(\mathbf{x} - \mathbf{x}_i(t))\delta(\mathbf{v} - \mathbf{v}_i(t)). \tag{1.39}$$

Hereby the density is non zero at the location of the i-th particle. For all following times t this corresponds to the trajectory of the particle in the phase space. A plasma consists of a large number of particles. So one has to sum over all particles in the plasma to get the total exact phase space density.

$$F(\mathbf{x}, \mathbf{v}, t) = \sum_i \delta(\mathbf{x} - \mathbf{x}_i(t))\delta(\mathbf{v} - \mathbf{v}_i(t)). \tag{1.40}$$

In phase space the plasma has a specific volume depending on the number of particles contributing to it. The number of the particles in the plasma is set as a constant value. So, even if the shape of the phase space volume changes the volume stays the same. The change in shape can be attributed to microscopic forces(fields). The trajectory of a particle in governed by electric and magnetic fields as well as collisions with other particles. In the next step we focus on the interaction of these particles with the fields generated by the sum of all particles. At a given point in time all particles are at a specific location. The particles form an electric and magnetic field. These fields are dependent on the position of the particles. Because of this electric and magnetic field a force acts on every single particle leading to a change in motion. Therefore the position changes and so do the fields. This force relation is displayed in the equation below.

$$\dot{\mathbf{v}}_i = \frac{q}{m}(\mathbf{E}_m(\mathbf{x}_i(t), t) + \mathbf{v}_i(t) \times \mathbf{B}_i(\mathbf{x}_i(t), t)) \tag{1.41}$$

It is the equation of motion for the i-te particle. The electric and magnetic fields in equation 1.41 are the ones that are created by the sum of all particles within the plasma. These microscopic fields have to satisfy the microscopic Maxwell equations:

$$\nabla \times \mathbf{B}_m(\mathbf{x}, t) = \mu_0 \mathbf{j}_m(\mathbf{x}, t) + \epsilon_0 \mu_0 \frac{d}{dt} \mathbf{E}_m(\mathbf{x}, t) \tag{1.42}$$

$$\nabla \times \mathbf{E}_m(\mathbf{x}, t) = -\frac{d}{dt} \mathbf{B}_m(\mathbf{x}, t) \tag{1.43}$$

$$\nabla \cdot \mathbf{E}_m(\mathbf{x}, t) = \frac{1}{\epsilon_0} \rho_m(\mathbf{x}, t) \tag{1.44}$$

$$\nabla \cdot \mathbf{B}_m(\mathbf{x}, t) = 0 \tag{1.45}$$

The microscopic electric field $\mathbf{E}_m$ is a result of the microscopic electric space charge $\rho_m$ whereas the microscopic magnetic field $\mathbf{B}_m$ is a result of the microscopic current density $\mathbf{j}_m$.

$$\rho_m(\mathbf{x}, t) = \sum_s q_s \int F_s(\mathbf{x}, \mathbf{v}, t) d^3v \tag{1.46}$$

$$\mathbf{j}_m(\mathbf{x}, t) = \sum_s q_s \int F_s(\mathbf{x}, \mathbf{v}, t) \mathbf{v} d^3v \tag{1.47}$$

The sum in equations 1.46 and 1.47 are taken over all charged particles within the plasma. The integration has to be done over the whole phase space. It is now possible to calculate the interaction of the particles with the electric and magnetic field due to equation 1.41(equation of motion) and the microscopic Maxwell equations 1.42,1.43,1.44,1.45. In the next step one considers the time evolution of the exact phase space density. The condition for a constant particle number leads to the fact that the total time derivative along all particle trajectories must be zero.

$$\frac{d}{dt} F(\mathbf{x}, \mathbf{v}, t) = 0 \tag{1.48}$$

By implementing the total time derivative one receives the Klimontovich-Dupree equation.

$$\frac{\partial F}{\partial t} + \mathbf{v} \cdot \nabla_{\mathbf{x}} F + \frac{q}{m}(\mathbf{E}_m + \mathbf{v} \times \mathbf{B}_m) \cdot \nabla_{\mathbf{v}} F = 0 \tag{1.49}$$

The third term on the left of the Klimontovich-Dupree equation consists of the equation of motion 1.41 for a particle that interacts with the collective microscopic fields. With equation 1.49 the state of the plasma can be described at all times within the phase space. Although this description yields an exact calculation of the plasma, its complexity grows with the number of particles. Therefore, it is not possible to calculate all interactions of the particles with each other and the microscopic fields. A way around that problem is the definition of ensemble averages. An ensemble is a larger number of particles, which are correlated by their interaction to each other. To get a quantity for this ensemble,

that can be used for further considerations, one averages over the whole ensemble. As an example the exact phase space density $F(\mathbf{x}, \mathbf{v}, t)$ becomes the ensemble averaged phase space density $\langle F(\mathbf{x}, \mathbf{v}, t)\rangle = f(\mathbf{x}, \mathbf{v}, t)$. The relationship between the exact phase space density and the ensemble averaged phase space density is depicted in the following equation:

$$F(\mathbf{x}, \mathbf{v}, t) = f(\mathbf{x}, \mathbf{v}, t) + \delta F(\mathbf{x}, \mathbf{v}, t). \tag{1.50}$$

The factor $\delta F(\mathbf{x}, \mathbf{v}, t)$ is a fluctuation that describes the deviation of the ensemble averaged phase density from the exact phase density. For this fluctuation the relation $\langle \delta F\rangle = 0$ must be satisfied. As for the exact phase density the microscopic fields can be described in the same manner. The two equations 1.51 and 1.52 below indicate the case of the microscopic fields.

$$\mathbf{E}_m(\mathbf{x}, \mathbf{v}, t) = \mathbf{E}(\mathbf{x}, \mathbf{v}, t) + \delta\mathbf{E}(\mathbf{x}, \mathbf{v}, t) \tag{1.51}$$

$$\mathbf{B}_m(\mathbf{x}, \mathbf{v}, t) = \mathbf{B}(\mathbf{x}, \mathbf{v}, t) + \delta\mathbf{B}(\mathbf{x}, \mathbf{v}, t) \tag{1.52}$$

The first term on the right of both equations describes the averaged **E**- and **B**-field over the ensemble. These considerations yield the kinetic equation for the ensemble averaged phase space density:

$$\frac{\partial f}{\partial t} + \mathbf{v}\cdot\nabla_{\mathbf{x}} f + \frac{q}{m}(\mathbf{E} + \mathbf{v}\times\mathbf{B})\cdot\nabla_{\mathbf{v}} f = -\frac{q}{m}\langle(\delta\mathbf{E} + \mathbf{v}\times\delta\mathbf{B})\cdot\nabla_{\mathbf{v}}\delta F\rangle \tag{1.53}$$

The kinetic equation has the advantage that the ensemble averaged phase density $f(\mathbf{x}, \mathbf{v}, t)$ and the fields(see eq. 1.51,1.52) do not depend on every single particle trajectory any longer. They depend on the coordinates of the phase space. The averaged phase density states the probability to find particles in a given phase space volume, defined by the coordinates. Through the averaging process the exact description of a single particle is no longer possible. Again, the kinetic equation is not an optimal description. The problem of this equation lies in the term on the right hand side. This term describes the correlation of the particles with the fields. To simplify the equation the correlations of the particles with the fields have to be neglected. This leaves a term on the right side of the kinetic equation that solely considers the collisions of the particles. Because of this simplification one obtains the generalized Boltzmann equation:

$$\frac{\partial f}{\partial t} + \mathbf{v}\cdot\nabla_{\mathbf{x}} f + \frac{q}{m}(\mathbf{E} + \mathbf{v}\times\mathbf{B})\cdot\nabla_{\mathbf{v}} f = (\frac{\partial f}{t})_c. \tag{1.54}$$

The collision term can be approximated. In the following paragraph two approximations are cited.

- Krook collision term: In this approximation one considers a partially ionized

plasma. Collisions only take place between charged particles and neutral particles. So the collision term can be written as:

$$(\frac{\partial f}{t})_c = \nu_n(f_n - f) \tag{1.55}$$

Here $\nu_n$ is the frequency of the collisions between a charged particle and a neutral particle, and $f_n$ is the distribution function of the neutral particles.

- Fokker-Planck equation: The plasma is considered to be fully ionized. There are no collisions. The collision term is replaced by an correlation term. This term describes the interaction of the particles to each other by their contributions to the field variations.

$$(\frac{\partial f}{t})_c = \nabla_{\mathbf{v}} \cdot (\mathbf{D} \cdot \nabla_{\mathbf{v}} f) \tag{1.56}$$

**D** is called the diffusion coefficient and depends on the particle velocities.

A special case of the generalized Boltzmann equation is the Vlasov equation. Hereby the plasma is regarded to be collisionless(e.g. space plasma). Therefore, the term on the right side vanishes.

$$\frac{\partial f}{\partial t} + \mathbf{v} \cdot \nabla_{\mathbf{x}} f + \frac{q}{m}(\mathbf{E} + \mathbf{v} \times \mathbf{B}) \cdot \nabla_{\mathbf{v}} f = 0 \tag{1.57}$$

Even though there are no collisions the particles interact with each other. However this interaction should not change the phase space density of the plasma. Therefore, the shape of the plasma in the phase space can change but the volume in the phase space is constant. This is the statement of the Liouville's theorem. For the Vlasov equation this is only then true when there are no collisions and no microscopic fields.

**Macroscopic Variables** Finally one has to get to the point where macroscopic quantities can be extracted. Before this can be done the averaged phase density $f(\mathbf{x}, \mathbf{v}, t)$, which is a probability distribution function has to be defined. But first, there are some simplifications that have to be taken into consideration. This distribution function is dependent on space, velocity and time. But many quantities of the plasma can be described by only knowing its velocity distribution function. Therefore, the space and time coordinates within the phase space are considered to be fixed. Around the thermal equilibrium of the plasma no changes in time or space occur, because there is no energy exchange between the charged particles of the plasma. Hence, the distribution function $f(\mathbf{x}, \mathbf{v}, t)$ can be regarded as a velocity distribution function $f(\mathbf{v})$. There are a lot of velocity distributions that can be used to describe any physical state of the plasma. The simplest form is the Maxwellian velocity distribution. Here the plasma is regarded as collisionless and isotropic.

$$f(\mathbf{v}) = n\Big(\frac{m}{2\pi k_B T}\Big)^{\frac{3}{2}} \exp\Big(-\frac{mv^2}{2k_B T}\Big) \tag{1.58}$$

To find the physical quantities of such a probability distribution on has to calculate its velocity moments. The problem is, that the macroscopic quantities only depend on space and time and not on the single velocities of the particles. Therefore one has to integrate the distribution over all velocities. The velocity moments are calculated the following way:

$$M_i(\mathbf{x}, t) = \int f(\mathbf{x}, \mathbf{v}, t)\mathbf{v}^i d^3v \tag{1.59}$$

Here M is the i-th moment of the probability distribution. The quantity $\mathbf{v}^i$ is a tensor of rank i. Not all moments that can be calculated are physically interesting. Some of that are important are the number density n, the bulk flow velocity $v_b$, the pressure tensor p and the kinetic temperature. In the following equations the probability distribution, which is dependent on space, velocity and time has been replaced by a velocity distribution.

- number density n:
$$n = \int f(\mathbf{v}) d^3v \tag{1.60}$$
- bulk flow velocity $v_b$: This quantity describes an average flow component of all particles or a specific species of the particles of the plasma.
$$\mathbf{v}_b = \frac{1}{n}\int \mathbf{v} f(\mathbf{v}) d^3v \tag{1.61}$$
- pressure tensor: All fluctuations from the mean velocity of all particles within the ensemble are focussed in this quantity.
$$P = m\int (\mathbf{v} - \mathbf{v}_b)(\mathbf{v} - \mathbf{v}_b) f(\mathbf{v}) d^3v \tag{1.62}$$
- kinetic temperature: The pressure tensor can be split into trace elements and traceless elements. The trace elements form the isotropic/anisotropic pressure depending which kind of plasma it is. The isotropic pressure is $p = nk_B T$. With that equation the kinetic temperature can be calculated. It is not a temperature in the normal sense. Its a measure of the distribution of the particle density in velocity space.
$$T = \frac{m}{3k_B n}\int (\mathbf{v} - \mathbf{v}_b)(\mathbf{v} - \mathbf{v}_b) f(\mathbf{v}) d^3v \tag{1.63}$$
By calculating the integral one derives the definition of the thermal energy for the isotropic case as being $E_{th} = k_B T$.

With the quantities described above the macroscopic definition of the plasma in the realm of the kinetic model is accomplished.

#### 1.2.2.3 Magnetohydrodynamics

In the previous subsection the plasma was described by the usage of the particles distribution function. Therefore, in the case of the collisionless plasma described by the Vlasov equation great precision was accomplished. But it is not always necessary to aim for precision. The calculation of the evolution of the exact distribution function leads to a great effort. Another approach is the theory of magnetohydrodynamics(MHD). The evolution of the plasma state is described by the evolution of the macroscopic moments. This is similar to fluid theory and therefore MHD uses the framework of that theory.

**Multi fluid theory:** The center of deliberations in MHD is the evolution of the macroscopic moments. Those moments used in the following considerations are the same as used in the previous subsection: number density $n_s(\mathbf{x}, t)$, bulk flow velocity $\mathbf{v}_{b,s}(\mathbf{x}, t)$, the pressure tensor $\mathbf{P}_s(\mathbf{x}, t)$ and the kinetic temperature $T_s(\mathbf{x}, t)$. The index s stands for a species within the fluid. In the multi fluid theory more than one kind of charged particles are considered. Therefore, s can stand for ions or electrons, which are separate species. To determine the evolution of the plasma state one needs a set of equations. This equations are obtained by forming different order moments of the Vlasov equation. The first equation that one gets of the zero order moment of the Vlasov equation is the continuity equation.

$$\frac{\partial n_s}{\partial t} + \nabla \cdot (n_s \mathbf{v}_s) = 0 \tag{1.64}$$

This equation states that no particle is created or annihilated as long as there is no interaction between the particles. This leads to the conservation of number density, mass and charge density. The equation itself couples the plasma density to the fluid velocity. But the velocity of the plasma cannot be determined. Therefore, one has to find another equation. By forming the first order moment of the Vlasov equation one gets the equation of motion.

$$\frac{\partial (n_s \mathbf{v}_s)}{\partial t} + \nabla \cdot (n_s \mathbf{v}_s \mathbf{v}_s) + \frac{1}{m_s} \nabla \cdot \mathbf{P}_s - \frac{q_s}{m_s} n_s (\mathbf{E} + \mathbf{v}_s \times \mathbf{B}_s) = 0 \tag{1.65}$$

It is the equation for the velocity of the plasma and it is called the momentum density conservation equation of the species s fluid of the plasma. The purpose of the equation is the connection of the fluid velocity to the density and the electromagnetic force, which acts on the fluid element. With the coupling of the fluid velocity to the electromagnetic force the fluid is also coupled to the electromagnetic equations. Additionally, the electromagnetic force leads to the coupling of all charged plasma fluid components. Now the solution for one species results in the need for the solution of the other species, as all species are linked to the electromagnetic field. Only by knowing all species dependent solutions one gets the solution for the momentum density conservation equation. Therefore, another moment of the Vlasov equation has to be determined. The energy

equation is the result of the second order moment of the Vlasov equation. It is also called the energy density conservation equation.

$$\frac{3}{2}n_s k_B(\frac{\partial T_s}{\partial t} + \mathbf{v}_s \cdot \nabla T_s) + p_s \nabla \cdot \mathbf{v}_s = -\nabla \cdot \mathbf{q}_s - (\mathbf{P'}_s \cdot \nabla) \cdot \mathbf{v}_s \tag{1.66}$$

The quantities in this equation are: $T_s$ the temperature, $p_s$ the scalar pressure, $\mathbf{q}_s$ the heat flux vector and $\mathbf{P'}_s$ the stress tensor part of the pressure tensor. The heat flux vector is a moment of third order and one has to derive another equation to find a solution for it. The stress tensor describes the momentum transfer in a perpendicular direction, when motion is directed at another direction. At this point, in order to get the final solution, one has to get an equation to get a solution for the heat flux vector. But this would probably not be the last equation that needs another equation to solve the previous one. Therefore, to stop this Russian doll of equations one must define an equation of state. This equation is chosen for the pressure in such a way that the energy equation vanishes. The form of this equation for the pressure depends on whether the plasma is isotropic or anisotropic.

**One-Fluid theory:** In the case of the One-Fluid theory one must consider the plasma to consist of only two different species, electrons and ions. Whereby the ions are of the same sort (e.g. protons). By using some equations of the multi fluid case the main equations for the one-fluid case can be derived. Before that, some conditions must be met. Firstly, the considered plasma has to fulfil quasineutrality, hence $n_e = n_i = n$. The number of electrons is equal to the number of ions. Therefore, the space charge $\rho$ should be zero, as one can devise of:

$$\rho = e(n_i - n_e) \tag{1.67}$$

Hereby e is the elementary charge. Additionally, the plasma should be free of a current, hence $\mathbf{j} = 0$.

$$\mathbf{j} = e(n_i \mathbf{v}_i - n_e \mathbf{v}_e) \tag{1.68}$$

As long as the particle flux densities are equal, which is satisfied when $n_i \mathbf{v}_i = n_e \mathbf{v}_e$, the plasma is current free. By using the continuity equation 1.64 and the equation of motion 1.65 of the multi fluid theory, the quantities: number density n, fluid mass m and fluid velocity $\mathbf{v}$ can be written as a combination of the corresponding electron and ion quantity. The indices in the following equation point to the species of the particle.

$$n = \frac{m_e n_e + m_i n_i}{m_e + m_i} \tag{1.69}$$

$$m = m_e + m_i \tag{1.70}$$

$$\mathbf{v} = \frac{m_i n_i \mathbf{v}_i + m_e n_e \mathbf{v}_e}{m_e n_e + m_i n_i} \tag{1.71}$$

The first equation to be considered for the one-fluid theory is the continuity equation. This equation was derived of the equation 1.64 and the definitions of n, m and **v**(equations 1.69, 1.70 and 1.71).

$$\frac{\partial n}{\partial t} + \nabla \cdot (n\mathbf{v}) = 0 \tag{1.72}$$

If the continuity equation is satisfied, the mass in the system is conserved. The next equation for the description of the fluid is the equation of motion(momentum density conservation equation). Again, the multi fluid case is the starting point for the considerations. In addition, the collision term is considered to account for the momentum transfer between the electrons and ions in the plasma. It also couples the electric fields to the resistive currents. Furthermore, the collision term R has a different sign for electrons than for ions.
Electrons(momentum equation):

$$\frac{\partial (n_e \mathbf{v}_e)}{\partial t} + \nabla \cdot (n_e \mathbf{v}_e \mathbf{v}_e) = -\frac{1}{m_e} \nabla \cdot \mathbf{P}_e - \frac{n_e e}{m_e} (\mathbf{E} + \mathbf{v}_e \times \mathbf{B}) + \frac{\mathbf{R}}{m_e} \tag{1.73}$$

Ions(momentum equation):

$$\frac{\partial (n_i \mathbf{v}_i)}{\partial t} + \nabla \cdot (n_i \mathbf{v}_i \mathbf{v}_i) = -\frac{1}{m_i} \nabla \cdot \mathbf{P}_i + \frac{n_i e}{m_i} (\mathbf{E} + \mathbf{v}_i \times \mathbf{B}) - \frac{\mathbf{R}}{m_i} \tag{1.74}$$

Adding those two momentum equations and by using the definitions for n, m, **v**, $\rho$, **j** and defining a total pressure $P = P_e + P_i$ and furthermore considering some approximations on the way one gets the equation of motion (momentum conservation equation for one-fluid):

$$\frac{\partial (nm\mathbf{v})}{\partial t} + \nabla \cdot (nm\mathbf{v}\mathbf{v}) = -\nabla \cdot \mathbf{P} + \rho \mathbf{E} + \mathbf{j} \times \mathbf{B} \tag{1.75}$$

A second material equation that results of the momentum conservation equation is the generalized Ohm's law. With its help the time evolution of the current flow **j** can be determined.
Generalized Ohm's law:

$$\mathbf{E} + \mathbf{v} \times \mathbf{B} = n\mathbf{j} + \frac{1}{ne} \mathbf{j} \times \mathbf{B} - \frac{1}{ne} \nabla \cdot \mathbf{P}_e + \frac{m_e}{ne^2} \frac{\partial \mathbf{j}}{\partial t} \tag{1.76}$$

The difference of the generalized Ohm's law to a simple form is its complexity. In this form it posses additional terms to the resistive term $n\mathbf{j}$. Those terms are the anisotropic electron pressure $\frac{1}{ne} \nabla \cdot \mathbf{P}_e$, a time dependent term of the current, which originates in the inertia of the electron motion, and the Hall term $\mathbf{j} \times \mathbf{B}$. The Hall term contributes to the resistance in a direction perpendicular to the current flow and the magnetic field. Like in the case of the multi fluid an energy conservation equation can be found.

Energy conservation equation:

$$\frac{\partial}{\partial t}[nm(\frac{1}{2}v^2 + w) + \frac{B^2}{2\mu_0}] = -\nabla \cdot \mathbf{q} \tag{1.77}$$

Here $w$ is the free internal energy density and $\mathbf{q}$ is the heat flux density vector. If the term $\nabla \cdot \mathbf{q}$ of the previous equation is equal to zero the total energy density is constant through time.

**Magnetic tension and Plasma Beta:** Two quantities that are found only in magnetohydrodynamics are the magnetic tension and plasma beta. The magnetic tension arises of the term $\mathbf{j} \times \mathbf{B}$ in the generalized Ohm's law. If one considers slow motions only, the displacement current in the plasma can be disregarded. By using the Ampere's law the cross product of the current flow and the magnetic field can be rewritten to:

$$\mathbf{j} \times \mathbf{B} = -\nabla(\frac{B^2}{2\mu_0}) + \frac{1}{\mu_0}\nabla \cdot (\mathbf{BB}). \tag{1.78}$$

The first term of this equation is called the magnetic pressure. It adds up to the thermal pressure in the plasma. The second term is the magnetic stress tensor, which contributes to the tension and torsion in the fluid. Another useful quantity to describe processes within the plasma is called plasma beta. It defines the ratio of the thermal and the magnetic pressure at the equilibrium of an isotropic/quasineutral plasma. A plasma can be differentiated of being a low-beta plasma, with $\beta << 1$, and a high-beta plasma with a beta around zero and above.

$$\beta = \frac{2\mu_0 p}{B^2} \tag{1.79}$$

**Equation of State:** To get a set of closed equations one has to find a condition and/or equation that truncates one quantity in such a way that no further equations are necessary. In the case of the pressure tensor on can consider the plasma as an ideal gas. Therefore, the ideal gas equation $p = nk_BT$ is valid. Now the equations possess a temperature dependence that has to be solved. This is described in the energy or heat conduction equation. In the isotropic case one only needs the energy conduction equation, which contains the heat flux. By truncating the heat flux the energy conduction equation only depends on the temperature. As a solution the system can be regarded as being in an isothermal or an adiabatic condition. This leads to a set of closed equations.

### 1.2.3 Reconnection

Reconnection is a process, in which magnetic field energy is converted into kinetic energy. It occurs on the solar surface, in earth's magnetic field and even in fusion reactors.

Some conditions have to be satisfied so that reconnection can occur. First, one would need a mathematical way to describe the time dependent development of the magnetic field. This is being achieved be using the generalised Ohm's law in combination with the Faraday's law and the Ampere's law. The generalised Ohm's law can only then be used, when the plasma is collision-less and the conductivity is near to infinity [3, p. 73ff].
Generalised Ohm's law:

$$\mathbf{j} = \sigma_0(\mathbf{E} + \mathbf{v} \times \mathbf{B}) \tag{1.80}$$

Faraday's law:

$$\nabla \times \mathbf{E} = -\frac{d\mathbf{B}}{dt} \tag{1.81}$$

The Ampere's law has to be modified. If one takes into consideration, that the characteristic length of the system $L_B$, in which the magnetic field changes is large, then the term of the electric field can be left aside[18, p. 46]:
Ampere's law(MHD):

$$\nabla \times \mathbf{B} = \mu_0 \mathbf{j} \tag{1.82}$$

This leads to the general induction equation:

$$\frac{d\mathbf{B}}{dt} = \nabla \times (\mathbf{v} \times \mathbf{B}) + \frac{1}{\sigma_0 \mu_0} \nabla^2 \mathbf{B} \tag{1.83}$$

The first term on the right side is called the convection term and describes the motion of the field lines over time. The second term on the right is the diffusive term and describes the diffusion of the magnetic field lines within the plasma. If the conductivity is very large or near infinity the second term vanishes. Therefore, the diffusion process can be neglected. The resulting equation yields the frozen in condition. Because there is no diffusion the magnetic field lines are bound to the plasma in terms of MHD to the fluid elements. The field lines are aligned with the plasma. Furthermore, during their motion the magnetic field lines can be distorted. This consideration also leads to the definition of a flux tube. If one looks at a closed surface at a time $t_0$ the magnetic flux through that surface is constant. Now the frozen in condition is satisfied. If the surface is moving and even changing its area one will observe that the magnetic flux through that surface at a time $t_1$ will be the same as in $t_0$. The volume encompassed by that magnetic flux is called a flux tube. In the case of the velocity of the plasma being zero and the resistivity is unequal to zero the first term of equation 1.83 can be dropped. Therefore, the general induction equation describes the diffusion of the magnetic field lines through the plasma. In that case the field lines will arrange in such a way that they reduce inhomogeneities in the plasma. Depending on the characteristic length the magnetic diffusion time can vary. If one considers space plasma like the solar wind, the general induction equation includes both terms. But after the diffusion time has elapsed the magnetic field lines

will get out of sync with the plasma and diffuse[3, p. 73ff]. Another important quantity that is useful for the description of reconnection is the magnetic Reynolds number. It describes the ratio between the convection term and the diffusive term.

$$R_m = \mu_0 \sigma_0 L_B v \tag{1.84}$$

Here $R_m$ is the magnetic Reynolds number, $\mu_0$ is the permeability of space, $\sigma_0$ is the conductivity of the plasma, $L_B$ is the characteristic length of the system and $v$ is the velocity of the plasma. With that ratio one can estimate if the frozen in condition is satisfied or if it is broken. In case $R_m$ is much larger than unity the frozen in condition is valid. But if $R_m$ is similar or equal to unity the frozen in condition breaks down. In the next step one has to consider two flux tubes. Those two areas can be very different from each other. The magnetic field lines can be orientated differently and even the magnetic field strength can vary. If the flux tubes get close together, a thin layer is being formed between them. This layer is called a current sheet. The magnetic field lines of the flux tubes, which are adjacent to the layer(flux tubes edges) are oriented parallel to the layer anti parallel to each other. Within the tube itself they can be oriented differently. In the first part of Figure 1.10 on the left the plasma and correspondingly the magnetic field lines move toward the current sheet. In some small area of the thin layer the Reynolds number can change to the point at which the frozen in condition would break down. The magnetic flux of the two flux tubes interact. At a specific point, depicted in the middle part of Figure 1.10 the so called X point is formed. At that point the magnetic field is zero. In a three-dimensional consideration the X point is representing a line called X type neutral line. The inward flow of plasma and magnetic field lines is governed by an electric field that is perpendicular to the magnetic field and the direction of the plasma. In the region around the X point diffusion between the two areas takes place. The red arrows in Figure 1.10 depict the plasma flow. After the field lines have entered the area around the X point the frozen in condition is invalid. The magnetic field lines and the plasma particles are no longer in sync. Therefore, plasma can flow from on side of the layer to the other connecting both tubes. In the diffusion region the magnetic field lines are reconnected. After leaving that region the frozen in condition is valid again. Plasma of the diffusion region is accelerated by the field lines perpendicular to the X point. In that way, magnetic field energy has been converted to kinetic energy of the plasma particles [18, p. 247].

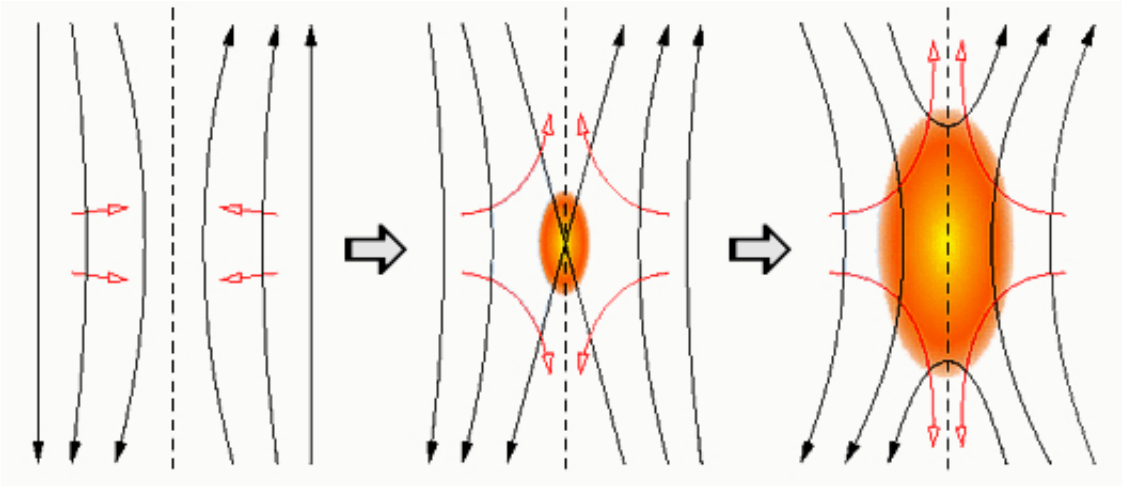

**Figure 1.10:** Process of reconnection at different stages[4].

### 1.2.4 Coordinate systems

The basis to describe any moving object in space or on earth is to give a common frame of reference. This is done by defining a point in space as the origin of a coordinate system. The objects' movements can now be described by the relative position to the origin defined by a metric. For space physics it is very important to have a coordinate system to describe the trajectories of stellar bodies, or defining locations of physical phenomena like current sheet boundaries or to simply define the direction of a measured field quantity (e.g. magnetic field vector). There are a lot of different coordinate systems in use. The reason for this diversity is that different problems can be described better or easier with a specific coordinate system. In the following paragraph two of the most common coordinate systems are addressed, the heliocentric and the geocentric coordinate system. The heliocentric coordinate system, as the name implies, is centred around the center of the sun. The configuration of the axes of the coordinate system leads to the classification into different subsets of the heliocentric coordinates. Two of those subsets are displayed below. The definition of the x- and the z-axis is given, whereas the y-axis is perpendicular to them[19, p. 712-713].

- Heliocentric Earth ecliptic(HEE): x-axis: Line between the sun's center and earth's center. z-axis: Perpendicular line to the ecliptic with the sun's center as origin.
- Heliocentric Earth equatorial(HEEQ): x-axis: Line between the sun's center and the intersection of the solar equator with the solar central meridian observed from earth. z-axis: Positive rotational axis of the sun (solar north pole).

The geocentric coordinate system is centred around the earth's center. As with the heliocentric coordinates there are subsets of this coordinate system. As for the heliocentric coordinates the y-axis is perpendicular to the x- and the z-axis[19, p. 712-713].

- Geocentric solar ecliptic(GSE): x-axis: Line between the earth's center and the sun's center. z-axis: Perpendicular line to the ecliptic with the earth's center as origin.
- Geocentric solar magnetospheric(GSM): x-axis: Line between the earth's center and the sun's center. z-axis: The dipole axis is projected on the yz-plane of the GSE coordinates.

In this thesis the commonly used coordinates are the GSE. Below are two Figures depicting the GSE and the HEE coordinate system.

## 1.3 Cluster Mission

### 1.3.1 History

The Cluster mission was one of the first cornerstone projects of the ESA. It was proposed in 1982 and after a timespan of 14 years the mission development ended in 1996 with the launch of the Cluster I mission. The vessel to transport the satellites into orbit was the Ariane 5 rocket. On June 4th, 1996, the Ariane 5 rocket had to be detonated remotely a little more than half a minute after its launch. Therefore, all of the four satellites were destroyed. Because of its importance for research a fifth satellite was built out of spare parts. At first, the satellite was supposed to be launched into orbit as a single vessel, but the scientific motivation behind the cluster mission needed more than one satellite to be successful. Through cut backs at administration, namely multiple ground stations, and because a fully developed concept had already existed three additional satellites were built. To reduce additional cost reduction the launch vehicle for the Cluster II mission was the Russian Soyuz-U/Frigat rocket. The four satellites were transported on two different launches. On July 16th, 2000, the first pair was launched and nearly a month later on August 9th, 2000, the second pair followed. From a highly elliptical orbit around the earth the four satellites began with their scientific measurements on February 1st, 2001. The duration of the mission was planned for three years, ending in 2003. Because of its success the Cluster II mission has been extended. In 2014 it will be replaced by the MMS (Magnetospheric Multiscale) mission. By means of a public contest ESA searched for names for the satellites. The winning proposal named the satellites as follows: Rumba, Salsa, Tango and Samba [20–22].

### 1.3.2 Goals

The Cluster mission investigates earth's magnetosphere by in-situ measurement. The four spacecraft orbiting earth in a tetrahedral formation conduct measurements to derive

a three dimensional image of the magnetosphere and the processes within it. Furthermore, different quantities of the plasma can be derived. Because of the high precision measurements spatial and temporal variations can be observed. The main emphasis lies on the investigation of the interactions between the solar wind and the magnetosphere, especially the interaction on the solar wind particles with the atmosphere through the polar cusps and the process of reconnection at the magnetotail during a substorm. A substorm is the result of the interaction of the solar wind with the magnetosphere. This interaction leads to a disturbance of earth's magnetic field, which results in the formation of an aurora. To observe these interactions mentioned above the spacecraft have to visit the key regions of the magnetosphere. These regions are as follows [21]:

- solar wind and bow show
- magnetopause
- polar cusps
- magnetotail
- auroral zones

### 1.3.3 Spacecraft and Instruments

As mentioned above, the Cluster mission consists of four identical spacecraft. The spacecraft orbit earth on a elliptic polar orbit with a perigee of 19000 km and an apogee of 119000 km. The duration of an orbit is roughly 57 hours. On their collective orbit the spacecraft are positioned in a tetrahedral configuration. Each spacecraft itself has a diameter of 2.9 m, a height of 1.3 m and weighs 1200 kg. They are equipped with solar panels which generate 224 W to sustain the instruments. In addition to their orbital motion each spacecraft rotates around its own axis with about 15 rotations per minute. The Instruments on-board the Cluster satellites are used to measure charged particles as well as electrical and magnetic fields along their orbit. Furthermore some additional quantities can be derived of the measurements [23]. In order to complete their task the Cluster satellites are equipped with 11 instruments. The following list displays those instruments and briefly describes their usage.

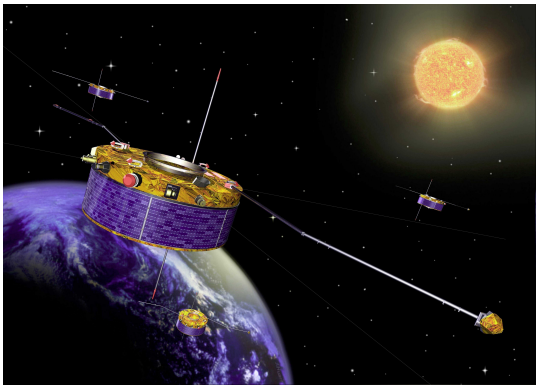

**Figure 1.11:** Artwork of the four Cluster satellites in formation [5].

1. FGM (Fluxgate Magnetometer)[10]:

   The FGM measures the magnetic field vectors in the vicinity of the spacecraft. The instrument contains two triaxial fluxgate magnetometers and a data processing unit. The two fluxgate magnetometers are spatially separated to ensure that the magnetic background of the spacecraft is at a minimum. One of the magnetometers is placed on a 5.2 m radial boom of the spacecraft (within the spin plane). The other magnetometer is located inside the spacecraft on a corresponding position to the outer one.

2. EDI (Electron Drift Instrument)[24]:

   The Electron Drift Instrument can be operated in two modes: In the electron drift mode and the ambient electrons count mode. The Instrument consists of two electron guns and two electron detectors. Via the electron drift experiment the magnetic field can be measured indirectly. In ambient electron count mode the electrons in the vicinity of the spacecraft can be counted in such a way to ensure a high time resolution.

3. ASPOC (Active Spacecraft Potential Control experiment)[25]:

   Through an ion beam the electrical potential of the spacecraft is being reduced. Therefore the quality of the gathered measurements can be enhanced.

4. STAFF (Spatio-Temporal Analysis of Field Fluctuation experiment)[26]:

   The instrument consists of two parts: a magnetic sensor that can measure in all three spatial directions and a two parted wave analyser. The instrument measures the variation of the magnetic field in respect to the location and the time. In addition, the second part of the instrument is part of the WEC (Wave experiment Consortium), which is comprised of four other instruments on the Cluster spacecraft.

5. EFW (Electric Field and Wave experiment)[27]:

   The main purpose of the EFW is the measurement of the electric field in the vicinity of the spacecraft. The instrument consists of four probes, which are mounted on 44 meter long wire booms in respect to the spacecraft within its spin plane. Therefore, the difference in potential of the single probes to each other and the spacecraft can be measured, leading to the measurement of the full electric field in the spin plane. The EFW is also part of the WEC.

6. DWP (Digital Wave Processing experiment)[28]:

   The DWP is a non-scientific instrument onboard the satellites. Its main function is the central coordination of the WEC experiment. The instrument controls the function of the related instruments via macros and thereby synchronises their effort. In addition, the DWP also stores data concerning its procedures to provide means for error analysis of the system itself.

7. WHISPER (Waves of High frequency and Sounder for Probing of Electron density by Relaxation experiment)[29]:

   The instrument is part of the WEC and cooperates directly with the EFW and the DWP. The components of the WHISPER are a receiver, a transmitter and a spectrum analyser. The instrument has two functions. Firstly, the measurement of the total electron density of the plasma and secondly, measuring naturally occurring plasma emissions in the frequency range of 2-80 kHz.

8. WBD (Wide Band Data Instrument)[30]:

   The main purpose of the WBD is the measurement of plasma waves in the magnetosphere of earth. To complete that task the instrument possesses two pairs of spin-plane electric dipole antennas and magnetic search coils(along the spin axis). With either one of those four possible measuring devices the instrument can gather its data. The WBD is also part of the WEC.

9. PEACE (Plasma Electron and Current Experiment)[31]:

   The PEACE instrument measures the velocity distribution of the plasma in all three spacial coordinates around the spacecraft. For this purpose it is equipped with two electron energy analyser, one for higher energies HEEA(High Energy Electron Analyser) and one for lower energies LEEA(Low Energy Electron Analyser). They are mounted on the satellites in opposite directions directed along the spin axis. Each analyser can detect plasma particles in an angle of $\pi$. Combined they have a detection angle of $2\pi$. Because of the spinning motion of the spacecraft they can collect electron counts from a full $4\pi$ solid angle. The data is collected and processed in the DPU of the instrument. The instrument samples data in the energy range of 0.6 eV to 26 keV.

10. CIS (Cluster Ion Spectrometry experiment)[32]:

    The CIS is an instrument to gather ion distributions in three dimensions with a time resolution of 4 seconds, that is one spin of the spacecraft. The two measuring devices that are used for acquiring the date are a time of flight ion composition and distribution function analyser and a hot ion analyser.

11. RAPID (Research with Adaptive Particle Imaging Detectors)[33]:

    In comparison to the PEACE instrument the RAPID instrument samples data in an energy range above 30 keV. For the detection of the charged particles within the plasma RAPID uses two different instruments: the Imaging Ion Mass Spectrometer (IIMS) and the Imaging Electron Spectrometer (IES).

#### 1.3.3.1 EDI (electron drift instrument)

**Instrument:** As mentioned in the previous section the Electron Drift Instrument can be run in two operation modes:

- active mode
- passive mode

In active mode an electron beam is emitted from the gun and detected at the detector. This mode is called windshield wiper mode (WW) or electric field mode (EF). WW is often used to describe the basic operation of the instrument, while EF is associated with the scientific measurements. In those measurements the drift velocity of the electrons is calculated. With the knowledge of the drift velocity and the magnetic field, which can be measured by the FGM, the electric field can be derived. In another approach the data gathered in WW mode can be used to calculate the magnetic field(see below 1.3.3.1). The time resolution of the instrument in WW mode is 1/8 s in Nominal mode (NM) and 1/64 s in Burst mode (BM)[24, p. 5].

In passive mode ambient electrons in the vicinity of the satellite are being detected. No electrons are emitted by the electron guns. Therefore this mode is called ambient electron mode (AE). Here electrons can be detected in three different pitch angles. The pitch angle is the angle between the velocity vector and the magnetic field line. The electrons are detected in 0°, 180° and 90°. Normally the 0° and 180° pitch angles are detected at once, while the angle of 90° is done separately. In other cases data is measured by alternating between 0°/180° and 90°. The time resolution in ambient electron mode is 1/16 s in Nominal mode (NM) and 1/128 s in Burst mode (BM) [24, p. 7].

The data used for this thesis of the EDI was solely gathered in WW mode. The following paragraph illustrates the basic makeup of the EDI. Figure 1.12 displays a picture of the electron gun/detector of the electron drift instrument. Figure 1.13 illustrates the schematic of the GDU(gun/detector unit). The electron gun is situated at the upper part of the unit. It has a cylindrical shape. As depicted in Figure 1.13 the electrons are generated at the cathode and accelerated onto the anode. Through octopole deflectors the electron beam is deflected to its designated direction. The electron beam is shown in Figure 1.13 represented by a red line leaving the gun.

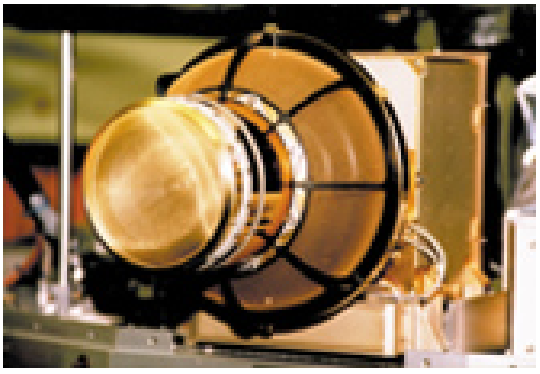

**Figure 1.12:** Picture of the GDU (gun/detector unit) of the EDI [6].

This narrow electron beam of the GDU can be directed in a solid angle of a little over $2\pi$ steradian. The detector of the GDU is situated below the gun. It surrounds it like a collar. The outer part of the detector is the entrance grid. An electron beam that passes that grid is first deflected by upper or lower deflectors, then guided by injectors to an analyser. Depending on the energy of the electrons the analyser directs the electrons to an annular micro channel plate, where they are detected. The detector can detect an electron beam in a solid angle of a little over $2\pi$ steradian.

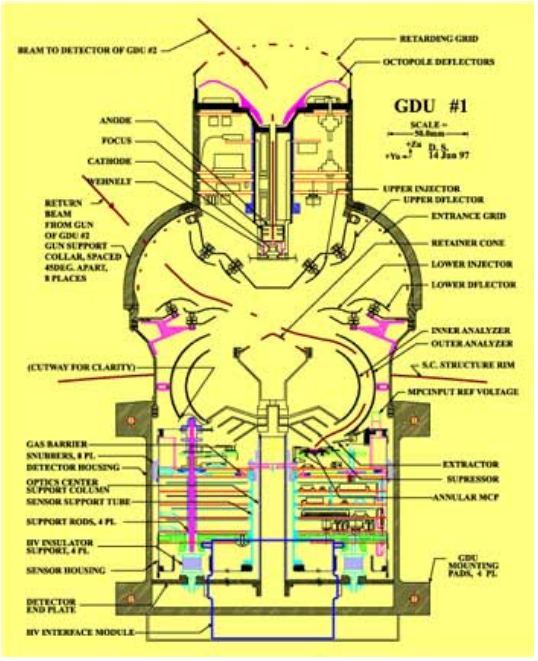


**Figure 1.13:** Detailed representation of the GDU(gun/detector unit) of the EDI [7].

On the satellite there are two GDU. They are positioned on opposite sides of the satellite. The guns are directed in anti parallel directions to each others. The electron beam of one gun is detected by its opposite detector. To ensure that those electrons of the emitted beam are registered at the other detector the electron beam is coded in a specific way(see below 1.3.3.1).

**Principle idea:** The idea behind the electron drift instrument is that electrons directed perpendicular to the magnetic field experience the Lorentz force. As a result of that interaction the electrons perform a circular motion. Hence the electrons return back to their source. In the case of the Cluster satellites two electron guns direct an electron beam perpendicular to the magnetic field. As long as there is no drift velocity $v_D$ the electrons move on an circular trajectory. If the electrons are exposed to an electric field $\mathbf{E}_\perp$ and/or a magnetic field gradient $\nabla\mathbf{B}_\perp$ they will exhibit a drift, hence a velocity $v_D$. Therefore the circular trajectory is distorted. The distortion shapes the trajectory shape as depicted in Figure 1.14. As illustrated in Figure 1.14 the shape of the trajectory depends on the direction the electron beam is injected perpendicular to the magnetic field. If the electron beam has a velocity component that is parallel to the drift velocity, then the electrons move on a shorter trajectory. If the velocity component is anti parallel to the drift velocity, then the electrons have a longer trajectory. There are two ways to determine the drift velocity $v_D$.

**Two methods to calculate the drift velocity:** The two methods to determine the drift velocity are the triangulation method and the time of flight (ToF) method.

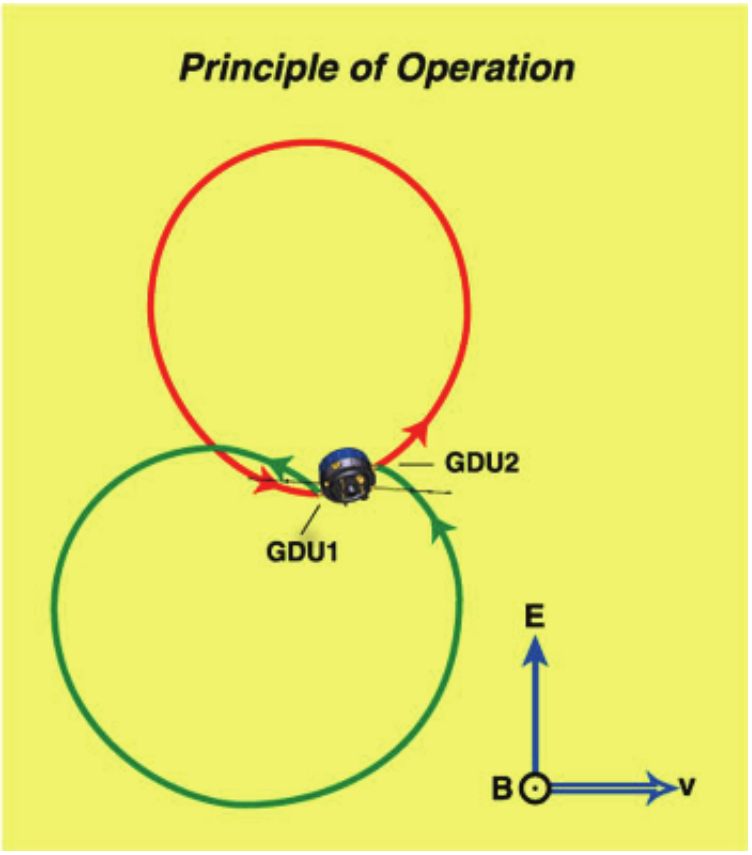


**Figure 1.14:** Electron orbits of the Electron Drift Instrument within a magnetic field [8].

Each of the two methods have regions of low and high accuracy. Fortunately, the two methods complement each other.

**Triangulation method:** The drift step d is the resulting displacement caused by the drift velocity $v_D$. This length is related to the drift velocity by the gyroperiod $T_g$. It is the time the emitted electron needs for one or more gyrations until it is detected. The relationship between those quantities is:

$$d = v_D \cdot T_g \tag{1.85}$$

The form of that equation assumes that there is just one gyration. If one knows the number of gyration the equation is multiplied on the right side by that quantity.
For simplification one assumes that there are only single gyrations. Electrons emitted from a source are detected at a detector. If there is no electric field $\mathbf{E}_\perp$ and no magnetic field gradient $\nabla\mathbf{B}_\perp$ then the source and the detector are at the same location. If that is not the case the source and the detector are placed in a distance d, the drift step, to one another. The location of both source and detector has to be a known factor. In

this configuration the lack of knowing the distance states an insurmountable problem. To avert it the electron guns can be placed in such a way that they are directed to an imaginary electron source location or away from it. Although the location of the imaginary source is unknown, it is possible through triangulation to find the position of the source. In Figure 1.15 the schematic makeup of the GDU systems on the Cluster satellites is depicted. The two GDU's are situated at the opposite sides of the satellite in a distance b. This distance is called the baseline. The precision of measuring d depends on b. Figure 1.16 illustrates an equivalent configuration of Figure 1.15. The difference is that the detector is placed in the middle of the two electron guns and the two sources in Figure 1.15 are combined into one. Therefore the length of the baseline b has to be doubled [9, p. 240ff]. Now the triangulation can be done easily. The two angles at which the electron beams are emitted and the length of the baseline are known quantities. This leads to the determination of the source S. Because the position of the detector is a known quantity too, d can be determined. By knowing d and $T_g$ the drift velocity $v_D$ can be calculated according to equation 1.85. Like every method the triangulation method has its limits. In the region of large drift steps the direction of the drift step is very accurate, but the value of d itself cannot be determined accurately enough. For very small drift steps the picture is reversed. The direction cannot be determined, but the value of d can be determined very accurately.
The two GDU on the Cluster satellites have a baseline b of 3 m. This leads to a virtual baseline of 6 m following the considerations in Figure 1.16.

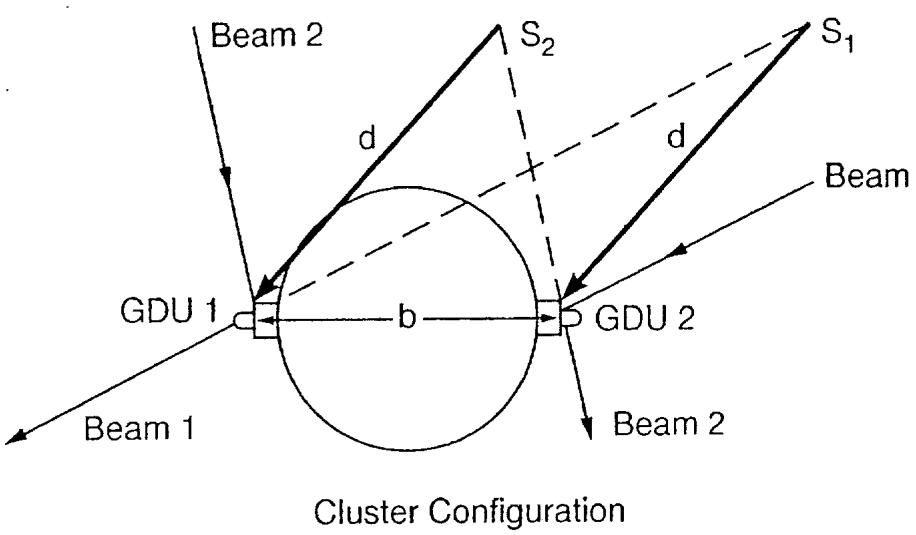


**Figure 1.15:** Configuration of the GDU onboard the Cluster satellites [9, p. 244].

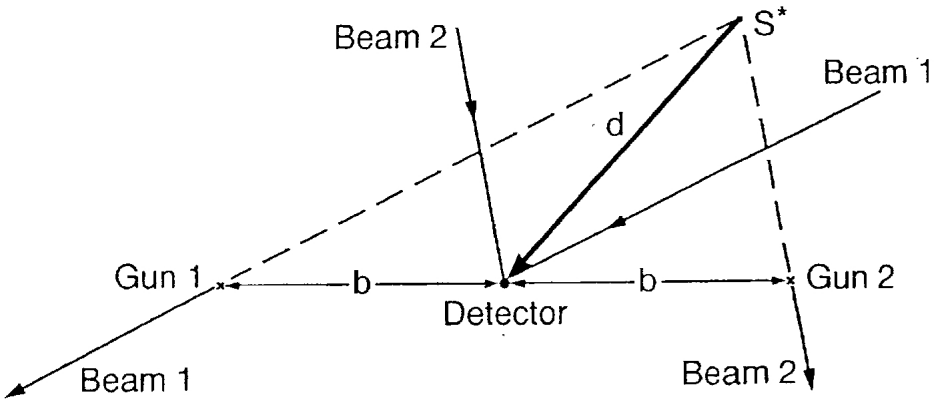


**Figure 1.16:** A simplified configuration of Figure 1.15 [9, p. 244].

**Time of flight method** In contrast to the triangulation method the time of flight method only uses the gyration times of each GDU to calculate the drift step. As mentioned above, depending on the direction the electrons are injected along $B_\perp$ their gyration trajectory is shortened or elongated. The resulting time difference is proportional to the drift step.

$$\Delta T = T_1 - T_2 = 2 \cdot T_g \cdot \frac{v_D}{v} \approx \frac{d}{v} \tag{1.86}$$

Here $T_1$ and $T_2$ are the gyration times for the elongated and the shortened trajectory. To calculate the drift velocity $v_D$ the gyroperiod has to be determined. v is the electron velocity. This velocity is given by the energy of the beam.

$$T_g = \frac{T_1 + T_2}{2} \tag{1.87}$$

Equation 1.87 defines the gyroperiod as the mean value between the two gyration times. Therefore, by knowing the gyration times it is possible to determine the drift velocity $v_D$ by simply using equation 1.86 and 1.87. To calculate the drift step d equation 1.85 can be used.

Another information that can be drawn from equation 1.86 is that the time difference can be measured even better, when d has larger values. Therefore, only the signal-to-noise effects limit the measurement of $\Delta T$, hence the measurement of d. As mentioned before, the two methods complement each other. For an increasing drift step d the triangulation method loses its accuracy. On the other hand, the time of flight method increases its accuracy and vice versa.

Not only is it possible to determine the drift velocity by using the time of flight method, but it can also be a reliable tool to calculate the magnitude of the magnetic field. The gyroperiod $T_g$ is inverse proportional to the magnetic field magnitude.

$$T_g = \frac{2\pi m_e}{eB} \tag{1.88}$$

Equation 1.88 characterises this relationship. Here e is the elementary charge of the electron and $m_e$ is the electron mass. The motion of the electrons has to be considered at relativistic speed.

$$m_e = m_{e,0} + \frac{T_k}{c^2} \tag{1.89}$$

The variable $T_k$ is the kinetic energy of the electrons. The electron gun of the electron drift instrument can operate in two energy modes: $1keV$ and $0.5keV$ [9, p. 246]. This feature of the time of flight method is very accurate. The magnetic field magnitude of around 30 nT can be estimated with a variance of only 0.1% [9, p.246]. Therefore, the method is predestined for in-flight calibrations. This is one of the reasons this method will be used at the upcoming mission MMS. The designated orbit of the MMS satellites is within the magnetosphere. Under that circumstance calibration of the FGM instrument in the solar wind region is out of the question.

**Time of flight measurement:** To measure the time of flight(ToF) of the electrons the EDI uses a specific correlator. This correlator consists of three components: a pseudo noise code(PN-code) generator, 'i' correlator counters and a delay-lock loop(DLL). For this correlator the measurements are divided into two magnetic field magnitude ranges. Depending on the range, 'i' is set accordingly. These two values depend on the number of stages(flip flops) used to generate the PN-code. For magnetic field magnitudes lower than 100 nT 'i' takes the value of 15. If the magnitude is higher than 100 nT 'i' is 127. As mentioned in the paragraph Instrument (see 1.3.3.1) the electron beam is coded in such a way that it can be distinguished from the ambient electrons. This is the reason for the usage of the PN-code. The code is generated by a shift register, where some of the outputs are logically linked to the input of the first stage. By making all the possible variations of the states, being '1' and '0', of each stage one gathers a sequence of ones and zeros. The variation, where every single stage is set to '0', is disregarded. This resulting sequence is a maximum-length PN sequence. The period of the sequence is determined by the following formula:

$$M \cdot \Delta = (2^{nos} - 1) \cdot \Delta \tag{1.90}$$

nos $\cdots$ number of stages in the shift register(low field = 4, high field = 7).
$\Delta \cdots$ code shift length.

The product $M \cdot \Delta$ is called code period $T_{PN}$. The code shift length is the inverse of the frequency of the clock in the shift register $f_c$. The clock frequency can be chosen in a broad range. By choosing a value for $f_c$ the code period $T_{PN}$ is set too. The initial setting sometimes leads to the case that $T_{PN}$ is much smaller than ToF. Therefore, the ToF cannot be measured accurately. This can be averted by using the magnetic field magnitude of the FGM to set a proper value for $T_{PN}$. To cover the whole range of ToF measurements the PN sequence is copied 'i' times, according to the range of the

magnetic field magnitude. Each copy is delayed by $\Delta$ to the following one and linked with a counter, resulting in a correlator counter. This forms the second part of the EDI correlator. Each of these correlator counters can be identified as a channel. A pulse is only counted at any channel at the time the code at the channel is set to one. If the channel is set to zero the pulse is disregarded. On average, all channels get hit by ambient electrons according to their PN sequence, but that does not indicate a pulse. In general, the PN sequences do not differ that much from each other. But with the delay of each sequence to the next one by a factor of $\Delta$, their individual phases differ. If one channel counts more than the average counts, then the received pulses have the same phase as this channel. This phase depends on the ToF. Therefore, ToF can be calculated. The last part of the EDI correlator is the DLL. It can be run in two modes: the tracking mode and the drift mode. In the tracking mode the system compares the counts to a specific threshold, the tracking sensitivity. If the threshold is surpassed the phase of all the i codes are reduced by a certain amount of $\Delta$, which is called the code shift step DT. This reduction in $\Delta$ leads to an increase in accuracy. The two quantities $\Delta$ and DT are related by the factors n and m. The formula below shows the definition of $\Delta$:

$$\Delta = \frac{n \cdot m}{2^{23}}[s] \tag{1.91}$$

DT is only dependent on n. As depicted in the formula above $\Delta$ is depending on both factors n and m. Therefore, the accuracy of the measurements can be increased by reducing m, without changing DT in the process. The second mode of the DLL is the drift mode. To ensure the best possible accuracy the counts should be centred in a specific channel, where the error can be minimized. This can be accomplished by shifting the phase of the 'i' codes. If the error is reduced far enough the tracking mode can be activated. The shift of the phase is done by comparing which of the channels has the most counts and by shifting the phase to its direction. At the end, the majority of the counts is set at the specific channel, which is the channel in the middle of the channel array. As for the tracking mode, the drift mode possesses a sensitivity threshold too, the drift sensitivity. This sensitivity describes the number of counts that are necessary to initiate the shift. Table 1.1 below shows initial values for DT, $\Delta$ and tracking-mode sensitivity SE for two regions in the magnetosphere, the tail lobe and the plasma sheet [15].

**Resolution of the electron drift instrument:** As stated in equation 1.88 the time of flight measurement is inversely proportional to the magnetic field magnitude. In the paragraph above it is shown that the time measurement is dependent on the shift step size DT. As a result of the dynamic variation of DT the resolution of the magnetic field measurement changes accordingly to it. Therefore, multiple ranges with different resolutions are used for magnetic field magnitudes below 700 nT in the EDI. Table 1.2 taken from the paper of E.Georgescu et al. [16, p. 3] depicts the different ranges for the

**Table 1.1:** Initial values of DT, Δ and tracking-mode sensitivity SE for two magnetosphere regions [15, p. 51].
B ··· magnetic field magnitude
E ··· electric field magnitude
DT ··· shift step size
$T_g$ ··· gyration period(equation:1.87)
Δ ··· code shift length
SE ··· tracking-mode sensitivity

| | Tail Lobe | Plasma Sheet |
|---|---|---|
| B[nT] | 30 | 20 |
| E[mV/m] | 0.5 | 1.0 |
| $T_g$[ms] | 1.2 | 1.8 |
| $\Delta T$[$\mu$s] | 2 | 9 |
| DT[$\mu$s] | 0.95 | 0.95 |
| Δ[$\mu$s] | 30.5 | 30.5 |
| SE | 17 | 9 |

EDI corresponding to the DT value and its resolution for the magnetic field magnitude measurement.

**Table 1.2:** Resolution of EDI [16, p. 3].
B ··· magnetic field magnitude
DT ··· shift step size

| B[nT] | DT[$\mu$s] | Digital Resolution of B[nT] |
|---|---|---|
| 0 - 15 | 1.907 | 0.012 |
| 16 - 31 | 0.953 | 0.007 - 0.026 |
| 32 - 63 | 0.476 | 0.014 - 0.053 |
| 64 - 127 | 0.238 | 0.027 - 0.11 |
| 128 - 163 | 0.476 | 0.22 - 0.35 |
| 164 - 325 | 0.238 | 0.18 - 0.70 |
| 326 - 657 | 0.119 | 0.35 - 1.4 |

#### 1.3.3.2 FGM (flux-gate magnetometer)

The flux-gate magnetometer is an instrument to measure the ambient magnetic field. It measures the magnetic field magnitude and its direction at a high precision. On each of the Cluster satellites there are two separate FGMs. The primary instrument is placed on a 5 meter long boom, while the secondary instrument is placed within the satellite. As a result of this arrangement the magnetic background can be minimised. The basic measurement principle behind the flux-gate magnetometer is a saturated transformer. If the transformer is in saturation and brought in to the vicinity of a magnetic field, then even harmonics will occur in the transformer. These harmonics are proportional

to the ambient magnetic field. For the measurement of the field the second harmonic is used, because of the simple reason it is its biggest. The instrument is made up of three identical transformers which are orthogonally positioned. Each transformer represents a component of the magnetic field. The saturation of the transformers is detected by pick-up coils. Those register the signal, hence the saturation, and pass it to an electronics unit. The electronics unit calculates the appropriate current that has to be fed to the feedback coils to even out the harmonics in the transformers. The feed in current is proportional to the ambient magnetic field. The range of the magnetic field measurement of each component of the FGM is subdivided into seven separate ranges. The reason for doing that is to gain a better resolution. Every range has its own sensitivity and therefore its own resolution. The ranges of the FGM with their corresponding resolution are depicted in table 1.3(Table used of the calibration report of the FGM instrument [10]). The last range was initially only used for ground calibration.

**Table 1.3:** Ranges and resolutions of the FGM instrument [10, p. 4].

| Range number | Range[nT] | Resolution[nT] |
|---|---|---|
| 2 | -64 to +63.97 | $7.8 \times 10^{-3}$ |
| 3 | -256 to +255.87 | $3.1 \times 10^{-3}$ |
| 4 | -1024 to +1023.5 | 0.125 |
| 5 | -4096 to +4094 | 0.5 |
| 6 | -16385 to +16376 | 2 |
| 7 | -65536 to +65536 | 8 |

The range changes are mostly done automatically, but there is a manual option too. The automatic range change is implemented by the digital processing unit (DPU), which is part of the electronics system of the FGM. To elevate to the next range the DPU uses the value measured by one of the three components of the FGM and checks if its above 90% of the current ranges absolute value. If this condition is satisfied the range for all components is increased. For a reduction of the range the DPU checks the measured values of all components of the FGM. Now if all components are smaller than 12.5% of the ranges absolute value the range number is decreased. If the instrument is set to a range the measurement can start. Hereby the instruments samples data, for example, with the primary sensor with a rate of 201.793 $\frac{vectors}{s}$. The acquired data is transmitted to the ground station. Because of the limited bandwidth the signal needs to be filtered before being sent to the uplink. This is done by the CPU of the instrument by applying a Gaussian digital filter on the signal. This filter matches the bandwidth of the acquired signal with the possible rate to be transmitted to the ground station. The most commonly used modes are $22.417\frac{vectors}{s}$ and $67.25\frac{vectors}{s}$.

**In-flight calibration of the FGM:** Before the data measured by the FGM can be used for its scientific purpose it has to be calibrated. Calibration is needed because there are a lot of error sources that have to be regarded. The FGM instrument is made

up of three sensors that are measuring each component of the magnetic field. These three sensors form the coordinate axes of the instrument. The coordinate system of the sensors has to be transformed to the spacecraft coordinate system. Furthermore, another transformation has to be done to transform the spacecraft coordinate system to a more general coordinate system like the GSE. In Figure 1.17 two of the three sensor axes are displayed in relation to a fixed cartesian coordinate system. One can see that these systems are misaligned and therefore the unknown angles have to be determined.

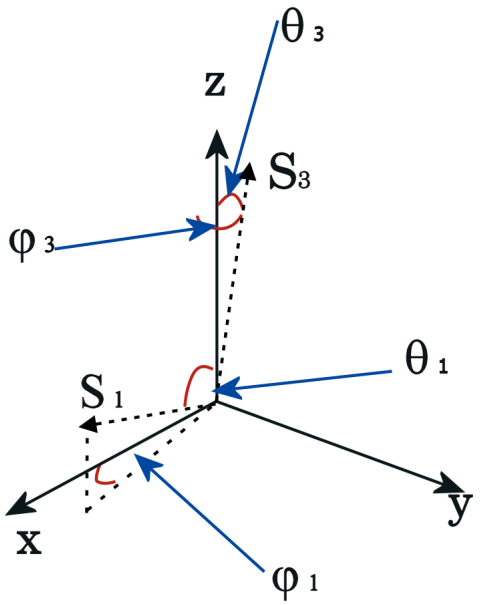


**Figure 1.17:** Coordinates axes of the sensors in relation to cartesian coordinate system. [10, p. 6].

The occurring errors in the calibration can be arranged into three categories. First, errors which are a result of the misalignment and non orthogonality of the coordinate system of the sensors in respect to a general coordinate system, here GSE. These errors are expressed by six angles between the two coordinate systems.This is exactly the case in Figure 1.17. The next kind of errors are those induced by the sensors themselves. If the sensors' sensitivity is falsely calibrated the measured values of the sensors are scaled by a multiplicative factor in respect to the actual value. Another error of that kind is an offset error. Hereby the zero level of the sensors are not calibrated. Therefore, an additive error is incorporated in the measured value. Furthermore, the electronics of the FGM can induce errors in the measurement as well. The last source of errors is the satellite itself. If parts on the satellite are magnetised this can have an effect on the measurement(e.g. offsets). As one can see there are a lot of different errors influencing the measurement and some which have yet to be found. For the coordinate

transformation of the sensor coordinate system into the GSE coordinates the following equation regards some of these errors.

$$\mathbf{V} = \mathbf{c}^{(instr)}\mathbf{c}^{(SR-FSR)}\mathbf{c}^{(spin)}\mathbf{c}^{(att)}\mathbf{B}_{GSE} + \mathbf{c}_0 \tag{1.92}$$

In equation 1.92 the variable V denotes the uncalibrated, raw signal measured by the FGM. Each of the matrices $\mathbf{c}$ in equation 1.92 represent a correction method for an error source. The matrices $\mathbf{c}^{(instr)}$ and $\mathbf{c}^{(SR-FSR)}$ can be combined to a matrix $\mathbf{c}^{(sensor)}$. This newly formed matrix corrects the sensitivity of the sensor and performs the correction of the alignment of the sensors to match an orthogonal coordinate system, the spacecraft coordinate system. The matrix $\mathbf{c}^{(spin)}$ takes care of the influence of the spin on the measurement. It corrects for the spin phase angle during the measuring process. Furthermore, the spacecraft coordinate system has to be transformed into the GSE system. This is done by the matrix $\mathbf{c}^{(att)}$. The offsets of the sensors of the instrument are corrected by the matrix $\mathbf{c}_0$. Equation 1.92 can be brought into a form that outlines the requested quantity $\mathbf{B}_{GSE}$:

$$\mathbf{B}_{GSE} = \mathbf{c}^{(att)^{-1}}\mathbf{c}^{(spin)^{-1}}\mathbf{c}^{(sensor)^{-1}}(\mathbf{V} - \mathbf{c}_0) \tag{1.93}$$

How can one check if the calibration done by the equation above leads to a viable result? First, one has to take the calibrated data for a specific time interval(e.g. single orbit) and generate the spectrum of that data. If some of those effects described above have not been corrected the spectrum will show some additional frequencies at the spin frequency and at its harmonics. These additional frequencies are called spin-tone. An example for a spectrum including additional frequencies is displayed in Figure 1.18. This Figure has been taken from the calibration report for the FGM. It depicts the spectrum of the magnetic field magnitude in the yz-plane(spin-plane), hence $|\mathbf{B}_{yz}|$. The left part of the Figure shows that the calibration was not successful. There are additional frequencies at 0.25 Hz and 0.5 Hz. The Cluster spacecraft carries out one rotation every 4 s(=0.25 Hz). This corresponds to one of the observed frequencies, whereas the other frequency is a harmonic of 0.25 Hz. By accomplishing another correction the harmonic can be reduced greatly. The spin-tone, however it is reduced is partially still observable. This shows that the process of calibration in the spin-plane has yet to be developed further. A technique to do this correction is called singular value decomposition. In the considerations above only the spine-plane was regarded. The reason for that is that the spin-axis does not contribute any additional frequencies to the spectrum, hence there is no spin-tone of the spin-axis. The error regarding the spin-axis is the spin-axis offset. This error can be calculated by different methods. One of these methods is the Hedgcock technique. For this technique the satellites' orbit must be partially crossing into the interplanetary space(out of the magnetosphere). Because this is not always possible, especially with an outlook at the upcoming MMS mission one has to use an alternative technique. A method to accomplish this is by using the electron drift instrument onboard Cluster.

The main purpose of this thesis is to evaluate the cross calibration of FGM and EDI. Sources:[11, p. 3ff, 17],[34, p. 1209ff],[35, p. 6ff],[10, p. 4ff].

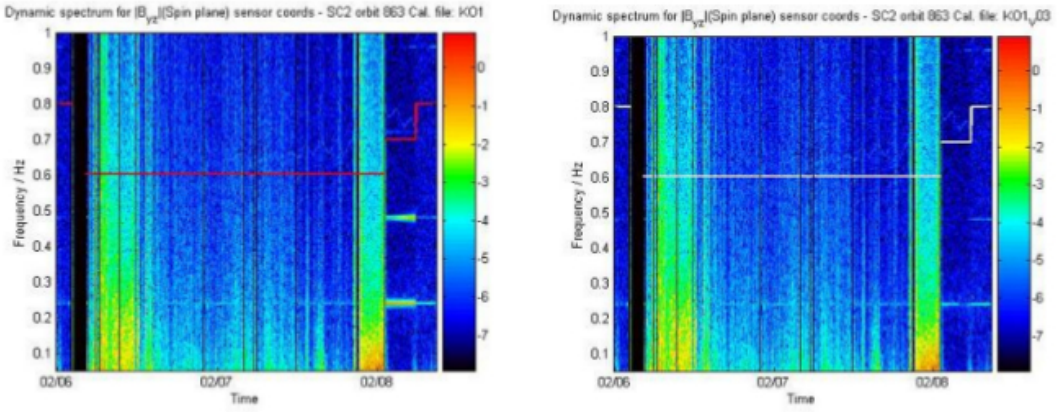


**Figure 1.18:** Spectrum of magnetic field magnitude $|\mathbf{B}_{yz}|$ in the yz-plane.(Left) After calibration still spine-tone visible at spin frequency (0.25 Hz) and first harmonic (0.5 Hz). (Right) Additional calibration yields reduction of spine-tone for both frequencies [11, p. 17].

### 1.3.4 Outlook(MMS)

The Magnetospheric Multiscale Mission, short MMS, is NASA's follow up mission to the Cluster mission. Like Cluster the mission uses four satellites to explore earth's magnetic field. The spacecraft will orbit earth on a near equatorial orbit, where the process of reconnection (see Reconnection) can be studied in great detail. With its improved sensors MMS measurements have a better spatial and temporal resolution. Therefore, the thin, fast moving electron diffusion region of the reconnection can be observed even better. An additional benefit of a better understanding of processes in the magnetosphere is an improved space weather forecast. Most modern technologies are sensitive to electromagnetic fields. Therefore, navigation systems like the GPS, telecommunications and even electrical power grids can be protected from harm.


**Figure 1.19:** Mission badge of the upcoming MMS mission depicting the four satellites in formation. [12].

## 1.4 CAA cluster active archive

At the beginning of the Cluster mission the data was only accessible to the Principal Investigators and Co-Investigators laboratories, who conducted the different experiments on Cluster. Since 2003 the Science Programme Committee of ESA brought the Cluster Active Archive (CAA) into being. It is an online platform that allows access to the Cluster satellite data. The team of the CAA is stationed at ESA's European Space research and Technology Center (ESTEC) in the Netherlands. Furthermore, experts on relevant topics at different institutes are supported in their participation for the maintenance of the system. Since September 2005 the system is accessible to anybody. After the registration at the website one can access the following types of data and tools:


**Figure 1.20:** Website interface of the Cluster Active Archive.

1. processed and validated high-resolution Cluster data
2. raw data
3. processing software
4. calibration data
5. documentations

Figure 1.20 shows the search mask of the website. Depending on the specific experiment one is interested in, the database can be searched according to a desired time period. Naturally, the data is only available within the time-frame in which the Cluster satellites are conducting measurements. During maintenance the data acquisition is not possible. The data is provided in the ASCII format. Furthermore, a lot of metadata information is available. The format of the files is called Cluster Exchange Format (CEF) [36].

# Chapter 2

# Practical work

## 2.1 EDI-FGM-crosscalibration

As stated in the introduction, the reason for the calibration of the FGM is to measure the magnetic field and its gradient more precisely. This leads to a better observation of the magnetosphere and the processes which take place within it. Many of these observations lead to the formulation of an magnetic field model called the Tsyganenko model(T 89 [37]). To some extent this model is a guideline in this thesis, when it comes to the evaluation of the measured magnetic field gradient measured by the Cluster satellites. The magnetic field measurements on the Cluster satellites are done by an FGM. It needs to be calibrated for different factors, as described in the section 1.3.3.2 (see inflight calibration). As mentioned, one of the quantities, the spin-axis offset, cannot easily be determined. Therefore, a second set of magnetic field measurements done by the EDI is used as a reference for calibrating the FGM. The EDI magnetic field values are absolute values. Therefore, no directional information of the magnetic field vector is gathered. At this stage, one has to make two assumptions to continue with the calibration. The primary assumption is that the spin-plane values of the FGM are properly calibrated. Therefore, one can use the components of the FGM to derive the spin-axis component of the EDI values. This is done by using the following equation, in which the spin-axis component is considered to be the z-axis.

$$\mathbf{B_z}(EDI) = \sqrt{(\mathbf{B}(\mathbf{EDI}))^2 - (\mathbf{B_x}(FGM))^2 - (\mathbf{B_y}(FGM))^2} \tag{2.1}$$

The second assumption is that EDI has no significant offset that is comparable to the spin-axis offset of the FGM. So that the difference between them is mainly due to the offset of the FGM spin-axis. But how can one be sure that the EDI values are good enough for such a calibration. As an example for their quality one can take a look at the magnetic field gradients measured by the EDI and the FGM compared to the above mentioned Tsyganenko model. In Figure 2.1 the magnetic field gradients, determined

by the multi-point measurements done by two Cluster satellites, are plotted against the quantity $\cos b$. This quantity will be described in the following paragraph.
First of all, $\cos b$ describes the direction of the magnetic field. If $\cos b$ is set to a single value a specific field direction is chosen. Furthermore, it allows to filter data sets for magnetic field directions of a specified angular range. Moreover, it displays the influence of the spin-axis offset on the spin-axis component of the magnetic field. If $\cos b$ has a low value the influence of the offset is small. The higher the value of $\cos b$ gets the larger is the extent of its influence. In the Figure below the magnetic field gradient of the EDI and the FGM is compared to the Tsyganenko model. If one considers the values of the EDI one can see that there is no reasonable deviation from the model at higher $\cos b$ values. On the other hand, if one compares the FGM values to the model considerable deviations for $\cos b$ values greater than zero occur. Therefore, the EDI values can be considered to have no comparable offset in the spin-axis. Before starting with the calibration the origin of the FGM and EDI data is described and some pre-calibration steps are explained.

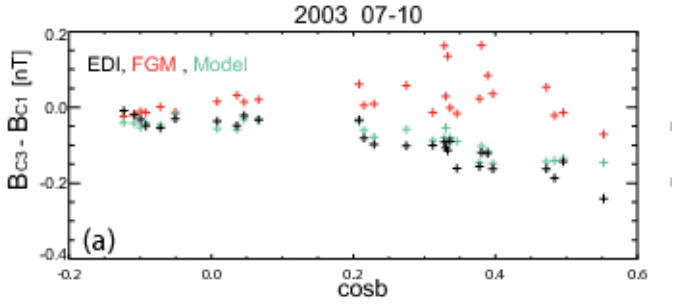


**Figure 2.1:** Magnetic field gradient of FGM, EDI and the Tsyganenko model plotted against $\cos b$(spin-axis influence)[13].

### 2.1.1 Used data sets

The data form the FGM is provided by programs written by Edita Georgescu (Max Planch Institute for Solar System Research) and a team at the Technical University of Braunschweig. The matching of the EDI and FGM datasets is done by programs written by Lukas Giner (Space Science Institute Graz). Furthermore, the programs of Lukas Giner prepare the data for further analytical use. The data of the FGM is provided by two programs. Each program returns the data of the FGM in a different calibration. The two calibrations are called: daily calibration and caa calibration. Each calibration is provided by a calibration file. The daily calibration is conducted by a team at Technical University of Braunschweig (Cluster Co-I team), whereas the caa calibration is done by the CAA team. Primarily, the daily calibration is used in this thesis. The daily calibration is done as its name suggests on a daily basis. The program "fgm_fsr_hr.bash" returns a file in the ASCII format with the ending ".mag". Upon executing the program, a specific date and one of the four Cluster satellites has to be chosen. The created

file contains the x-, y-, and z-component of the magnetic field measured by the FGM and the corresponding time at that specified day. The corresponding data of the EDI was downloaded from the Cluster active archive website. As mentioned in the section regarding the CAA, the data is provided in the CEF format. Another format that is being used for scientific purposes is the CDF (Common Data Format). In general, all data relevant to the EDI experiment in this thesis is utilised in the CDF format. To get to the data the following steps have to be made. First of all, one has to search for the specific time period. As already mentioned, the EDI experiment is not obtained continuously. Furthermore, one has to point out that the FGM in respect to the EDI delivers more datasets. This is understandable if one considers that successful detection of gyrated electrons is limited in some regions. In the next step the dataset with the needed gyration times has to be chosen. After both data sets have been acquired their timestamps have to be matched. This is done by the program "match_edi_fgm.pro". This is done for every single data point. Only if the time stamp of the EDI and the FGM are within a certain margin the data is matched. The program returns an array describing the position of the matched data points. With this array both data sets can be used for cross calibration. In this thesis data from four months of the year 2003 from the Cluster 1 satellite is used for analysis. The months are as follows: July, August, September and October.

### 2.1.2 FGM offset

In section 1.3.3.2 the FGM is described in detail. In that paragraph in-flight calibration of the FGM the process of transforming the measured data into a workable coordinate system and the correction according to some known deviations was lined out. It was pointed out that the measured data can be calibrated to a certain degree. For example, the deviations of the spin-plane can be corrected properly. The spin-axis however, possesses an offset that can not be corrected with the same method. Hereby one has to apply another strategy. This strategy is the cross-calibration of the FGM with the EDI. Before doing so one has to know how the offset of the spin-axis effects the spin-axis component (z-component) of the magnetic field. Partly this is already shown in Figure 2.1, the bigger the factor $\cos b$ is the greater is the effect of the spin-axis offset. The factor $\cos b$ is defined below.

$$\cos b = \frac{\mathbf{B_z}}{\mathbf{B}} \tag{2.2}$$

In equation 2.2 $\mathbf{B_z}$ is the z-component and $\mathbf{B}$ the magnetic field measured by the FGM. The factor b is the angle between the two vector quantities. Figure 2.2 depicts the relationship between the two quantities.

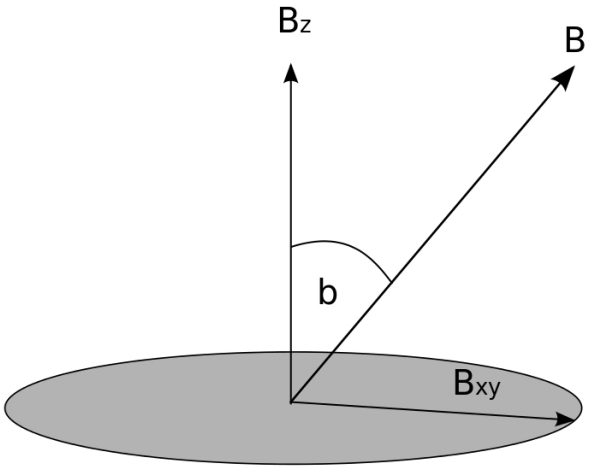


**Figure 2.2:** $\cos b$: Relationship of $\mathbf{B_z}$ and $\mathbf{B}$

The Figure shows that if the angle b is set to 90°, hence $\cos b$ is equal to zero, the magnetic field vector **B** lies within the xy-plane. In the plane **B** is not effected by the offset of the spin-axis. In Figure 2.1 at $\cos b = 0$ the magnetic field of the FGM is about the same as the Tsyganenko model. At $b = 0°$ the spin-axis offset has its largest contribution. Now one can compare the z-component of the magnetic field measured by the FGM to the corresponding EDI measurements. This is done for the month of August in 2003 (Cluster 1 satellite).

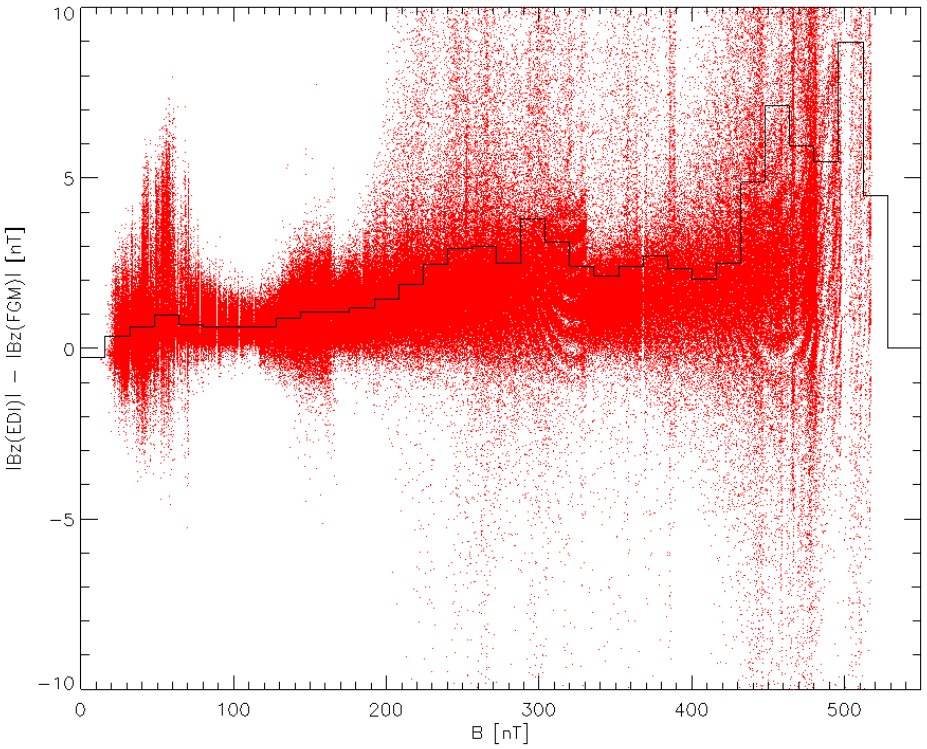


**Figure 2.3:** Difference of $|\mathbf{B_z}(EDI)|$ and $|\mathbf{B_z}(FGM)|$ with respect to the magnetic field magnitude.

In Figure 2.3 the difference of $|\mathbf{B_z}(EDI)|$ and $|\mathbf{B_z}(FGM)|$ in respect to the magnetic field magnitude is depicted. The black line shows the average deviation of the two values. The average is taken over a defined magnetic field range (bin) of 10 nT. This Figure uses all values without any constraint. Now one can use $\cos b$ as a condition to minimise the contribution of the spin-axis offset. Therefore, only certain directions of the magnetic field are considered. In Figure 2.4 only values which satisfy $\cos b > 0.7$ are used. This corresponds to an angle of $b > 45.57°$.

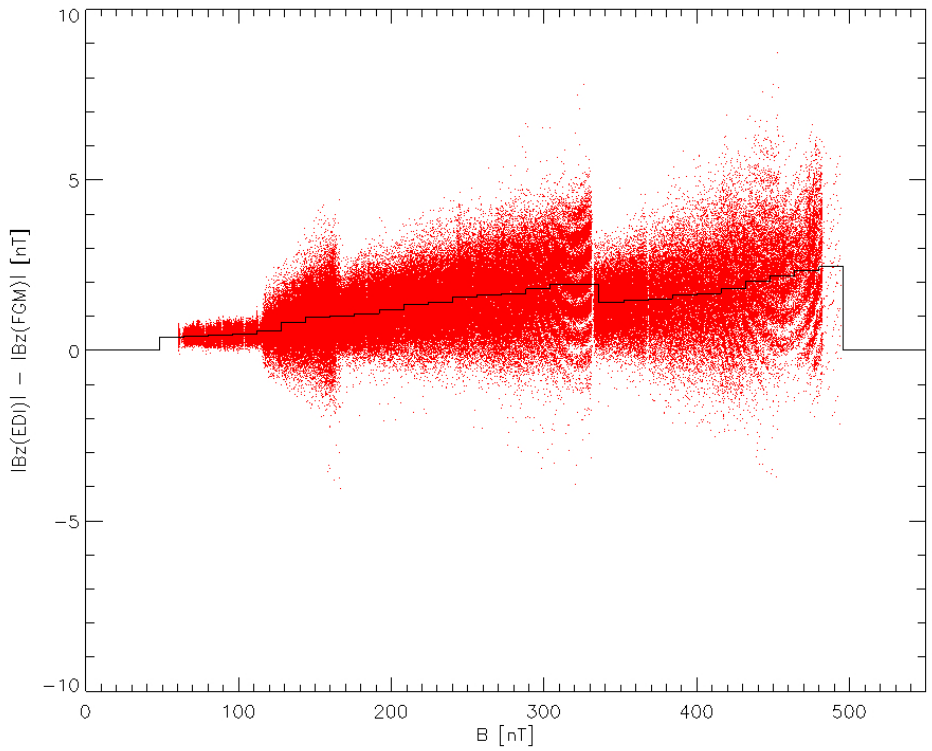


**Figure 2.4:** Difference of $|\mathbf{B_z}(EDI)|$ and $|\mathbf{B_z}(FGM)|$ in respect to the magnetic field magnitude for value which satisfy $\cos b > 0.7$.

Figure 2.4 shows that the average value is reduced compared to those in Figure 2.3. Because of the $\cos b$ condition, values with a large deviation from zero are neglected. One question arises from the form of the average value line. Why is it not a straight line? If the spin-axis offset is just an additive quantity the difference of $|\mathbf{B_z}(EDI)|$ and $|\mathbf{B_z}(FGM)|$ should be around a certain constant value, the offset itself. But in Figure 2.3 and 2.4 the black line contains two ranges which show the behaviour of a non-linear ascent. The first is around the magnetic field range of about 100 nT to 300 nT and the second one is about 340 nT up to the end. These two ranges make one wonder if there is another deviation that is not accounted for. This leads to the considerations for the time of flight offsets of the EDI.

### 2.1.3 EDI offset

At first it was considered that there is only one offset, the spin-axis offset of the FGM. But the Figures 2.3 and 2.4 from the previous section gave an indication for some additional offsets. The FGM is well calibrated in the spin-plane. Therefore, this deviation has to be another unknown quantity or it is part of the EDI values. The magnetic field values of the EDI are a result of the time of flight measurements described in the section

1.3.3.1. By using equation 1.88 the measured times are transformed into a magnetic field. The EDI possesses different modes where measurements are conducted. The different modes are distinguished by a quantity called CRF (code repetition frequency). It will be discussed in greater detail below.

**Code repetition frequency (CRF):** As mentioned in section 1.3.3.1 in the paragraph time of flight measurement the quantity $T_{PN}$ (code period) is proportional to the code chip length $\Delta$. The proportional factor is defined by the sensors' electronics. There are two possible values defining two settings of the sensor for the magnetic field measurement. One for the magnetic field below 100 nT and another for the magnetic field above 100 nT.
B $<$ 100 nT:

$$T_{PN} = 15 \cdot \Delta \tag{2.3}$$

B $>$ 100 nT:

$$T_{PN} = 127 \cdot \Delta \tag{2.4}$$

The code repetition frequency is defined as the inverse of the code period $T_{PN}$. As its name suggests the CRF is a frequency.

$$CRF = \frac{1}{T_{PN}} \tag{2.5}$$

If the quantity $\Delta$ is changed the accuracy is changed as well. Because the CRF is related to $T_{PN}$ it is related to $\Delta$ as well. Therefore, if the accuracy changes so does the CRF. The change results in a different CRF value, hence a different mode. Each mode possesses its own standard deviation. It is defined by the code chip length $\Delta$. The standard deviation of a specific mode is given by:

$$\sigma = \frac{\Delta}{5} \tag{2.6}$$

The modes given by the CRF should not be mistaken with the ranges of the EDI displayed in table 1.2. As described in the section 1.3.3.1 the resolution of the time of flight measurement is defined by the drift step size DT. The two quantities DT and $\Delta$ are indirectly related by equation 1.91. There are circumstances where DT,the time resolution, remains the same but the accuracy described by $\Delta$ changes. That would explain why there are sometimes more than one modes in the same resolution range. Another thing that is of interest concerning the CRF are oscillations between different modes. At the edges between two modes the electronics of the detector can switch between them. Because of the settings of the electronics this can lead to oscillations between the modes. The oscillations can be displayed by plotting the CRF as a function of time. Now one can get rid of the oscillations by applying the program "crf_const.pro"

. In Figure 2.5 the temporal evolution of the CRF within one day is plotted. One can see the oscillations between different CRF values (modes).

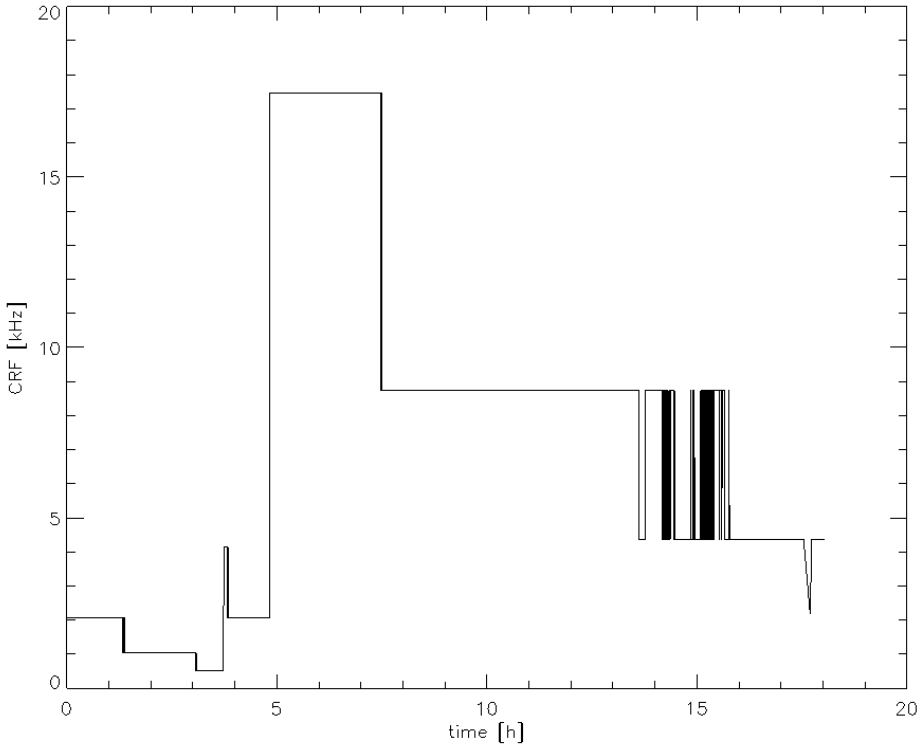


**Figure 2.5:** Temporal evolution of the CRF for one day (5th of August, 2003).

After the program "crf_const.pro" has been used the oscillation of the temporal evolution of the CRF values are properly reduced (see Figure 2.6).

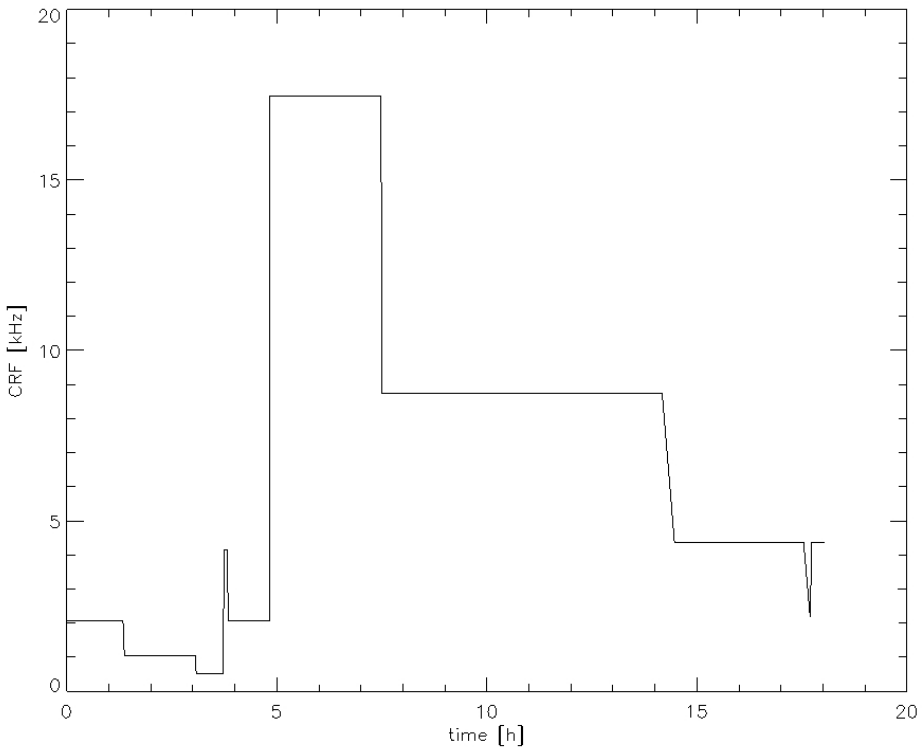


**Figure 2.6:** Temporal evolution of the CRF for one day (5th of August, 2003), after usage of the oscillation reduction.

In Figure 2.7 the modes given by the CRF are plotted in a histogram in respect to the magnetic field of the FGM.

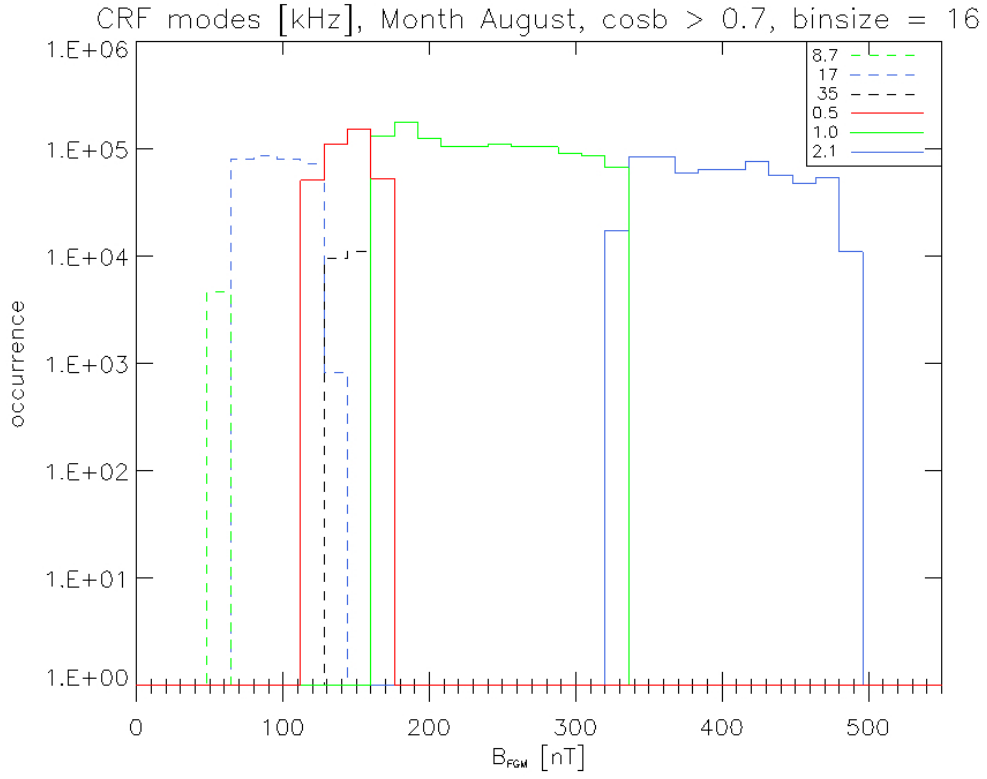


**Figure 2.7:** Different modes of the EDI (CRF modes) in respect to the magnetic field magnitude.

Lastly, one has to think about the offset of each single mode. Because the modes describe measurements with different accuracy their respective offset should differ too. Furthermore, the time of flight offsets seem to be related to the offset of the z-component of the magnetic field. This relationship has to be further examined.

### 2.1.4 Offset interactions

The interaction of the magnetic field offset to the time of flight offsets and vice versa can be described by a simple model. One uses equation 1.88 and modifies it to express the magnetic field. In addition, a constant factor $\Delta T$ is added to the time of flight variable $T_g$. This factor $\Delta T$ represents the offset of the time measurement, hence the offset of a mode. Equation 2.7 describes the change of the magnetic field of the EDI resulted by that factor $\Delta T$.

$$B_{EDI} = \frac{2\pi m_e}{e(T_g + \Delta T)} \tag{2.7}$$

In the next step the z-component of $\mathbf{B}_{EDI}$ is calculated according to equation 2.1. The relative change resulted by the factor $\Delta T$ can be expressed by the following equation:

$$\Delta \mathbf{B_z} = \mathbf{B_z}(T_g) - \mathbf{B_z}(T_g + \Delta T) \tag{2.8}$$

Analogously this can also be done for the magnetic field of the FGM. In that case, equation 1.88 is modified in the same way as above. The z-component of the FGM $B_z$ is extended with the additive quantity $\Delta B_z$.

$$T_{FGM} = \frac{2\pi m_e}{e(B_z + \Delta B_z)} \tag{2.9}$$

The relative change of the time of flight values resulted by the offset of the spin-axis can be described by:

$$\Delta T_{FGM} = T_{FGM}(B_z) - T_{FGM}(B_z + \Delta B_z) \tag{2.10}$$

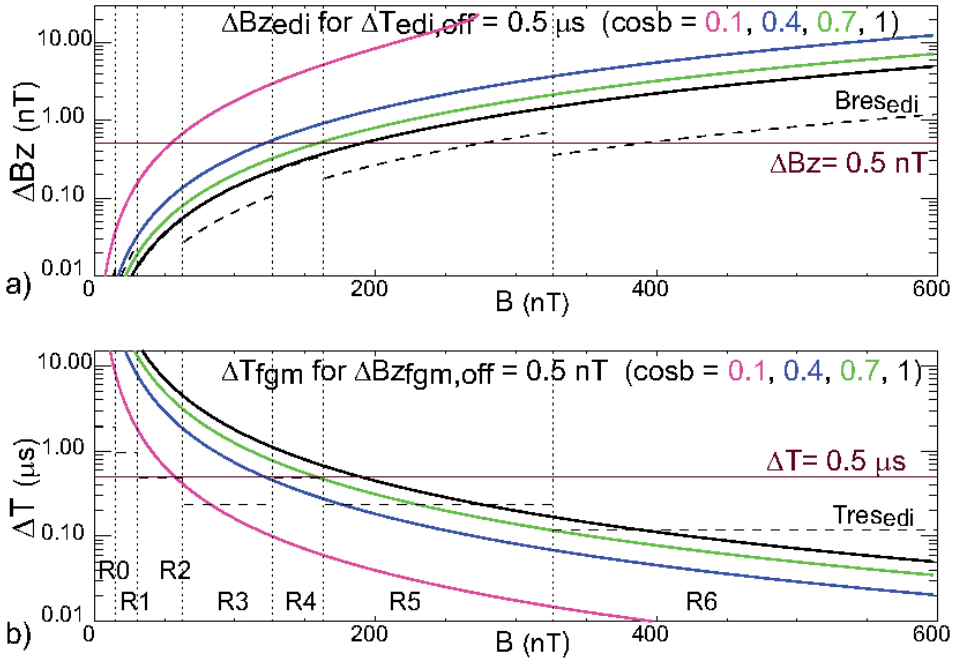


**Figure 2.8:** (a) Effect of the EDI time of flight offset $\Delta T = 0.5\ \mu s$ on the offset $\Delta B_z(EDI)$. The magnetic field offset $\Delta B_z$ is plotted as a function of the magnetic field magnitude. (b) Effect of the FGM offset $\Delta B_z(FGM) = 0.5$ nT on the time of flight offset $\Delta T$. $\Delta T$ is plotted as a function of the magnetic field magnitude.

Figure 2.8 displays the two cases stated by equation 2.8 and 2.10. In the upper part of Figure 2.8 the change of the offset $\Delta B_z$ as a function of the magnetic field is displayed. Hereby, an offset for the time of flight measurement is set to $\Delta T_{EDI} = 0.5\ \mu s$. Figure 2.8 (a) shows four different directions of the magnetic field defined by the $\cos b$ condition ($\cos b = 0.1, 0.4, 0.7, 1.0$). Directions with a smaller $\cos b$ value are les influenced by the

spin-axis offset and vice versa. The lower part of Figure 2.8 depicts the change of the time of flight offset as a function of the magnetic field. As described in the paragraph above an offset is added. In this case it is a constant spin-axis offset $\Delta B_z(FGM) = 0.5$ nT. In Figure 2.8 (b) there are also four directions of the magnetic field displayed. Along the magnetic field magnitude several ranges are marked, labelled as R0-R6. These ranges refer to the EDI ranges of different resolutions listed in table 1.2. Furthermore, the resolution is marked by a dashed line labelled $Bres_{edi}$ in the upper part and $Tres_{edi}$ in the lower part. In both parts of Figure 2.8 the direction of the magnetic field stated by $\cos b = 0.1$ (marked pink), describes the smallest interaction between the two different offsets. All other magnetic field directions deviate from it. Because of a larger growing influence of the respective offset in Figure 2.8 the smaller $\cos b$ becomes the more the offsets effect each other.
In the next step one considers the effect one offset has on the other one's magnetic field magnitude dependence. In Figure 2.8 (a) the spin-axis offset is plotted in respect to the magnetic field magnitude. As described above, the time of flight offset has an effect on this relation. For low magnetic field strengths, here represented by R0 to R2, nearly all magnetic field directions show an offset $\Delta B_z$ below 0.5 nT. The higher the magnetic field gets the larger the offset $\Delta B_z$. Therefore, the spin-axis offset $\Delta B_z$ should be calculated at a lower magnetic field in the ranges of about R0 to R2. Naturally, the $\cos b$ condition has to be considered because of its effect on the spin-axis offset. The same consideration also applies to Figure 2.8 (b). In this case the relationship of the time of flight offset to the magnetic field is effected by the spin-axis offset $\Delta B_z$. If one considers the low magnetic field magnitude from above, hence R0-R2, the time of flight offset is pretty large. In this case the time of flight offset should not be calculated in this region. For higher magnetic fields, like R5 and R6, the offset is getting smaller. In these ranges, especially in R6, the time of flight offset can be calculated very precisely.

### 2.1.5 Offset calculations

In general one is confronted with two different kinds of offsets. On the one hand there is the spin-axis offset of the FGM and on the other hand one has to handle the time of flight offset of the EDI. As stated before the EDI possesses more than one offset. These modes have to be calculated separately. The deliberations of the previous section lead to the realisation that there are ranges in the magnetic field **B** at which the different offsets take larger and smaller values. For any further calculation this has to be considered. In the next step one has to separate the calculation by the magnetic field. There are three regions that have to be considered. The regions consist of ranges displayed in Figure 2.8.

- low-field region: R1 - R3 (B $\approx$ 16 nT - 127 nT)
- mid-field region: R4, R5 (B $\approx$ 128 nT - 325 nT)

- high-field region: R6 (B ≈ 326 nT - 657 nT)

**low-field region:** First the spin-axis offset has to be calculated. The different directions of the magnetic field displayed in Figure 2.8 (a) show that the spin-axis offset is small in the first few ranges. For the calculation of the spin-axis offset it is necessary to use only specific directions of the magnetic field. Because the data of the first two ranges R0 and R1 does not contain any data at those directions, only data of the ranges R2 and R3 is used for the calculation. The reason for using certain directions, hence a $\cos b$ condition, is to use only data that has a large contribution of the z-component of the magnetic field compared to its xy-components. This is ensured by the condition $\cos b < 0.7$. The spin-axis offset is larger for those directions compared to the others. Now to derive the spin-axis offset the difference of $|\mathbf{B_z}(EDI)|$ and $|\mathbf{B_z}(FGM)|$ is calculated. The resulting array contains the spin-axis offset for every single data point of the reduced data set. By taking the average the spin-axis offset $\Delta B_z$ is obtained. Additionally, the standard deviation of that quantity is calculated as well. By knowing the spin-axis offset in the low-field region it is possible to determine the modes of the CRF in the ranges R1 to R3. Hereby a different $\cos b$ condition has to be used, because one only needs data that is minimally effected by the spin-axis offset. This is true for $\cos b < 0.1$. Using this condition one can calculate the different modes by calculating the difference of $T_g$ (times of flight) and $T_{FGM}$ (converted magnetic field magnitude see equation 2.9). Furthermore, their respective standard deviations are calculated. The CRF modes contained in the ranges R1 to R3 are depicted in Figure 2.7 as mode 1, 2 and 3.

**mid-field region:** As one can see in Figure 2.8 (a) and (b) in the ranges R4 and R5 both offsets are of equal magnitude. Therefore, the spin-axis offset of the low-field region is used in the mid-field region as well, because the spin-axis offset should not change at least up to 256 nT. At the magnetic field magnitude of 256 nT the FGM changes its range. This range change results in the change of the spin-axis offset as well. So one can use the low-field region offset up to this point. The calculation of the spin-axis offset above 256 nT is done after determining the other offsets of the mid-field region. There are three modes contained in the mid-field region. Hereby one mode reaches over the range change at 256 nT. But this should not change its value. In the range R4 there are two modes that have to be calculated. Although the spin-axis offset is already calculated for this range the direction of the magnetic field is chosen to be near the spin-plane. Therefore, the spin-axis offset has little influence on the values of the modes. Again $\cos b < 0.1$ is chosen. The result are the values for mode 4 and 5. For the range R5 the mode 6 is calculated in the same way as before. Only the data of the mode under 256 nT is used for its calculation. By using the value of mode 6 it is possible to calculate the spin-axis offset for the data above 256 nT. Like for the first calculation of the spin-axis offset the magnetic field directions according to $\cos b > 0.7$ are used for

its determination. After calculating the difference of $|\mathbf{B_z}(EDI)|$ and $|\mathbf{B_z}(FGM)|$ the spin-axis offset $\Delta B_z$ for $B > 256$ nT is derived. Compared to the low-field region the spin-axis offset is not that important, because of the magnitude of the magnetic field. At magnetic field magnitudes beyond 256 nT the spin-axis offset is insignificant compared to the field itself.

**high-field region:** In the high-field region only one range R6 still remains. In this case the spin-axis offset derived in the mid-field region for magnetic fields above 256 nT is used to calculate the last mode, mode 7. As already mentioned, the spin-axis offset is not relevant in this region. Therefore, one can use every data there is. As for all other modes and spin-axis offsets before in addition to the value itself the standard deviation is calculated too.

**Calculated offsets:** In the table 2.1 below the values of each mode and spin-axis offset is presented. The calculations were executed for four months in 2003: July, August, September and October.

**Table 2.1:** Calculated values for the spin-axis offsets and the modes of the EDI. The calculation was applied on the datasets for the months of July, August, September and October in 2003.

| Offsets | July | August | September | October |
|---|---|---|---|---|
| $\Delta Bz_{FGM}(low)[nT]$ | 0.51 ± 0.15 | 0.46 ± 0.16 | 0.64 ± 0.17 | 0.57 ± 0.17 |
| $\Delta Bz_{FGM}(high)[nT]$ | 0.40±0.99 | 0.41±0.99 | 0.57±1.04 | 1.00±0.19 |
| $\Delta T_{EDI,R1}[\mu T]$ | 2.92±5.77 | 1.90±4.77 | 2.87±6.42 | 1.92±4.98 |
| $\Delta T_{EDI,R2}[\mu T]$ | 1.81±2.42 | 1.60±1.96 | 1.81±1.89 | 1.85±2.40 |
| $\Delta T_{EDI,R3}[\mu T]$ | 0.38±1.15 | 1.03±1.27 | 0.70±0.89 | 1.20±1.04 |
| $\Delta T_{EDI,R4a}[\mu T]$ | 0.21±0.25 | 0.15±0.20 | 0.19±0.16 | 0.05±0.23 |
| $\Delta T_{EDI,R4b}[\mu T]$ | 0.65±0.97 | 0.63±0.96 | 0.50±0.97 | 0.48±1.00 |
| $\Delta T_{EDI,R5}[\mu T]$ | 0.55±0.42 | 0.55±0.43 | 0.59±0.46 | 0.57±0.50 |
| $\Delta T_{EDI,R6}[\mu T]$ | 0.28±0.19 | 0.26±0.19 | 0.27±0.19 | 0.26±0.20 |

### 2.1.6 Calibration (month)

The values acquired by the calculations described in the last section, where used to calibrate the dataset of the four months mentioned above. Therefore, the z-component of the magnetic field measured by the FGM has to be corrected by these values. In the case of the FGM the dataset contains two separate offsets. The spin-axis offset for the magnetic field range below 256 nT and the spin-axis offset above that value. Hereby,

the dataset is divided into two blocks and for each block the spin-axis offset was added to the z-component appropriately. This is done by using the following equation:

$$B_z = B_z + \Delta B_z \tag{2.11}$$

One has to mention at this point that the z-component of the FGM could also measure negative values. The FGM can measure the magnetic field magnitude and the direction of the field as well. If one imagines a coordinate system with the three orthogonal axes, a magnetic field is directed along the z-axis. There are two possible directions along the axis, a positive direction and a negative direction. According to this consideration each component of the magnetic field vector could be positive or negative and hereby determine the direction of the field. The magnetic field data gathered by the time of flight measurements of the EDI are absolute values. Therefore, one cannot extrapolate the direction of the magnetic field. As a result the calculated spin-axis offset can either be positive or negative depending on the used magnetic field data of the FGM. The calibration for the different modes of the EDI is integrated into the calculation of the z-component of the magnetic field. The applied equation to accomplish that task is equation 2.1. The correction regarding the modes is executed in the definition of the magnetic field magnitude of the EDI. This is done by using equation 2.7. For the factor $\Delta T$ the value of the mode has to be inserted into the equation. As for the spin-axis offset not every data point in the dataset is inflicted with the same offset, hence is not part of the same mode. Therefore, the dataset has to be divided for all the different modes. Afterwards any mode can be calibrated with the calculated value for the mode. In the next step the difference of the calibrated components $\mathbf{B_z}(FGM)$ and $\mathbf{B_z}(EDI)$ is calculated. In the beginning of this chapter the raw data (difference of the previously mentioned quantities in uncalibrated form) was displayed in Figure 2.3. The average deviation of a bin (small magnetic field range) is displayed as a black line. It shows considerable deviations of a zero level. In the Figures 2.9 (July), 2.10 (August), 2.11 (September) and 2.12 (October) the calibrated data is plotted for the examined months. Here the difference of the z-components (FGM and EDI) are plotted in respect to the magnetic field magnitude of the FGM. The Figures are color coded. The data points plotted in the color red are the original data. The original dataset as well as the calibrated dataset only contain data of a certain direction given by $\cos b > 0.7$. The data points in the color cyan display the calibrated dataset. The black line shows the average deviation of the original dataset. The blue line depicts the average deviation of the calibrated dataset. The three dashed lines mark the zero level and a deviation of this level by $\pm$ 0.5 nT. It must be noted at this point that the values for the first three modes (time of flight offsets) are set to zero because in the low-field region their error is as large as their respective value. Therefore, setting the values of these modes to zero is justified. In addition, the Figures are complemented with a histogram depicting the occurrence of the different modes of the EDI. The modes are named according to their CRF.

Out of the four months August is calibrated the best (Figure 2.10). The deviation of the zero level is at its highest value about 0.2 nT. The calibrated data of July, Figure 2.9, shows a slightly increasing average deviation at higher magnetic fields. This deviation starts at about 400 nT and increases up to the end. The same trend can be observed in the calibration of the month of September (Figure 2.11). The largest deviation is observed in the month of October (Figure 2.12). At this point one has to think of an additional factor, because the data used should not be that different concerning its initial calibration. Therefore, to get a better understanding of this phenomenon further studies have to be conducted. This would ensure the future application of this calibration method. The program used to calculate the spin-axis offsets(FGM) and the offsets of the different modes (EDI) is called "calibrate_month.pro". This program is described in the appendix.

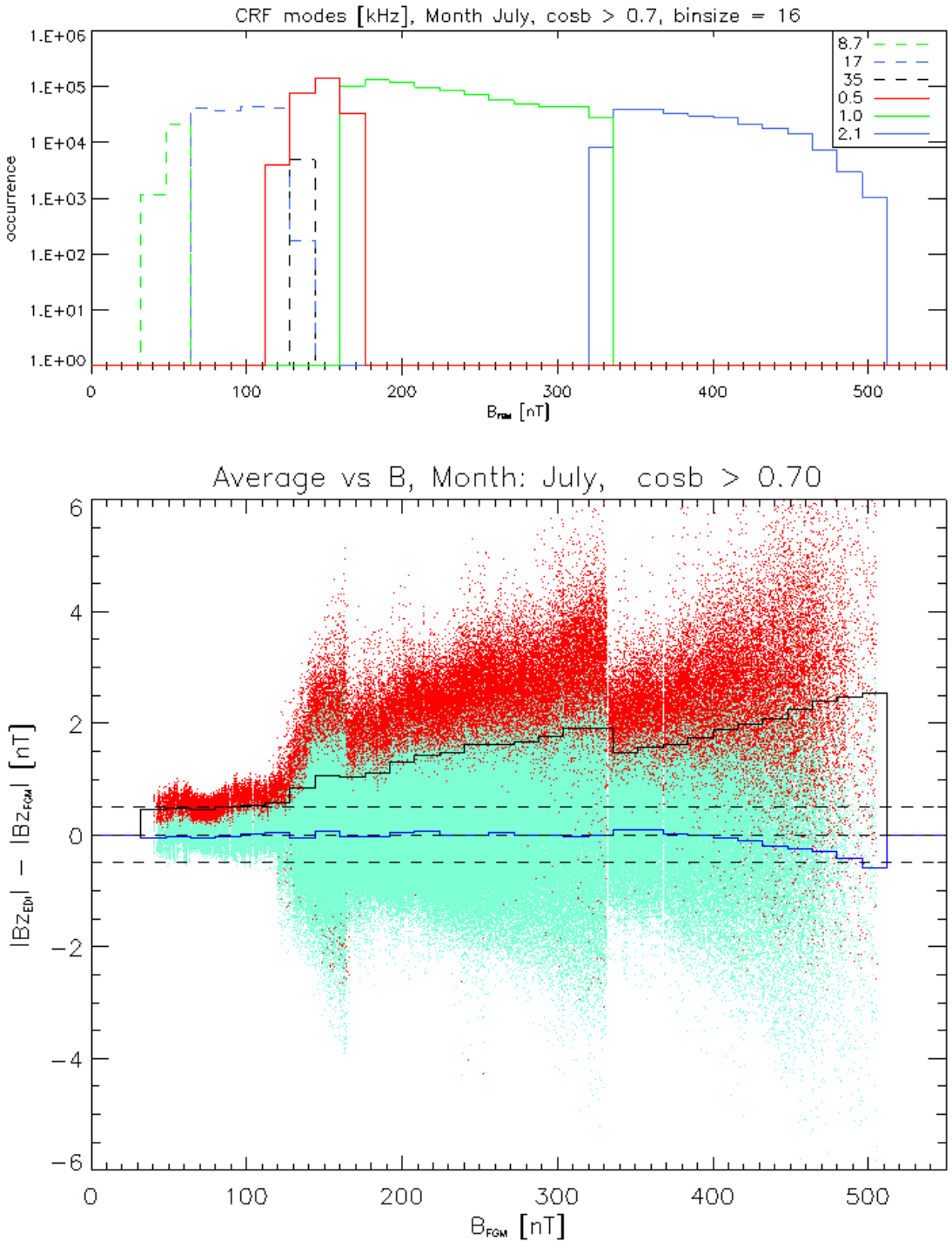


**Figure 2.9:** Calibration of the month of July in 2003.
(u) Occurrence of the different modes of the EDI (CRF modes) in respect to the magnetic field measured by the FGM.
CRF modes: mode 2 = 8.7 kHz, mode 3 = 17 kHz, mode 4 = 35 kHz, mode 5 = 0.5 kHz, mode 6 = 1.0 kHz, mode 7 = 2.1 kHz.
(l) Comparison of the original data (red) and the calibrated data(cyan). The black line (original data) and the blue line (calibrated data) show the averaged difference of the used bins.

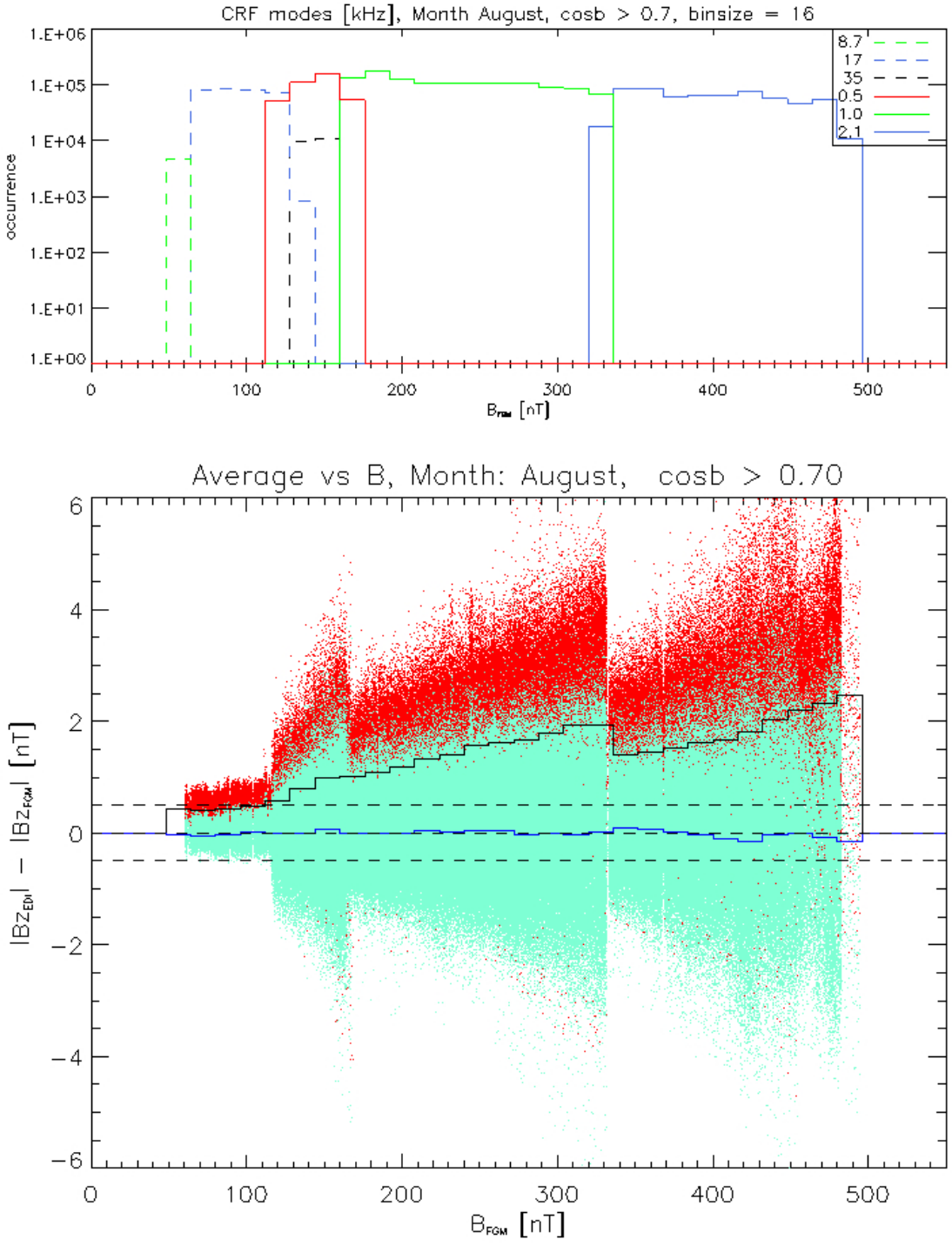


**Figure 2.10:** Calibration of the month of August in 2003.
(u) Occurrence of the different modes of the EDI in respect to the magnetic field measured by the FGM.
CRF modes: mode 2 = 8.7 kHz, mode 3 = 17 kHz, mode 4 = 35 kHz, mode 5 = 0.5 kHz, mode 6 = 1.0 kHz, mode 7 = 2.1 kHz.
(l) Comparison of the original data (red) and the calibrated data(cyan). The black line (original data) and the blue line (calibrated data) show the averaged difference of the used bins.

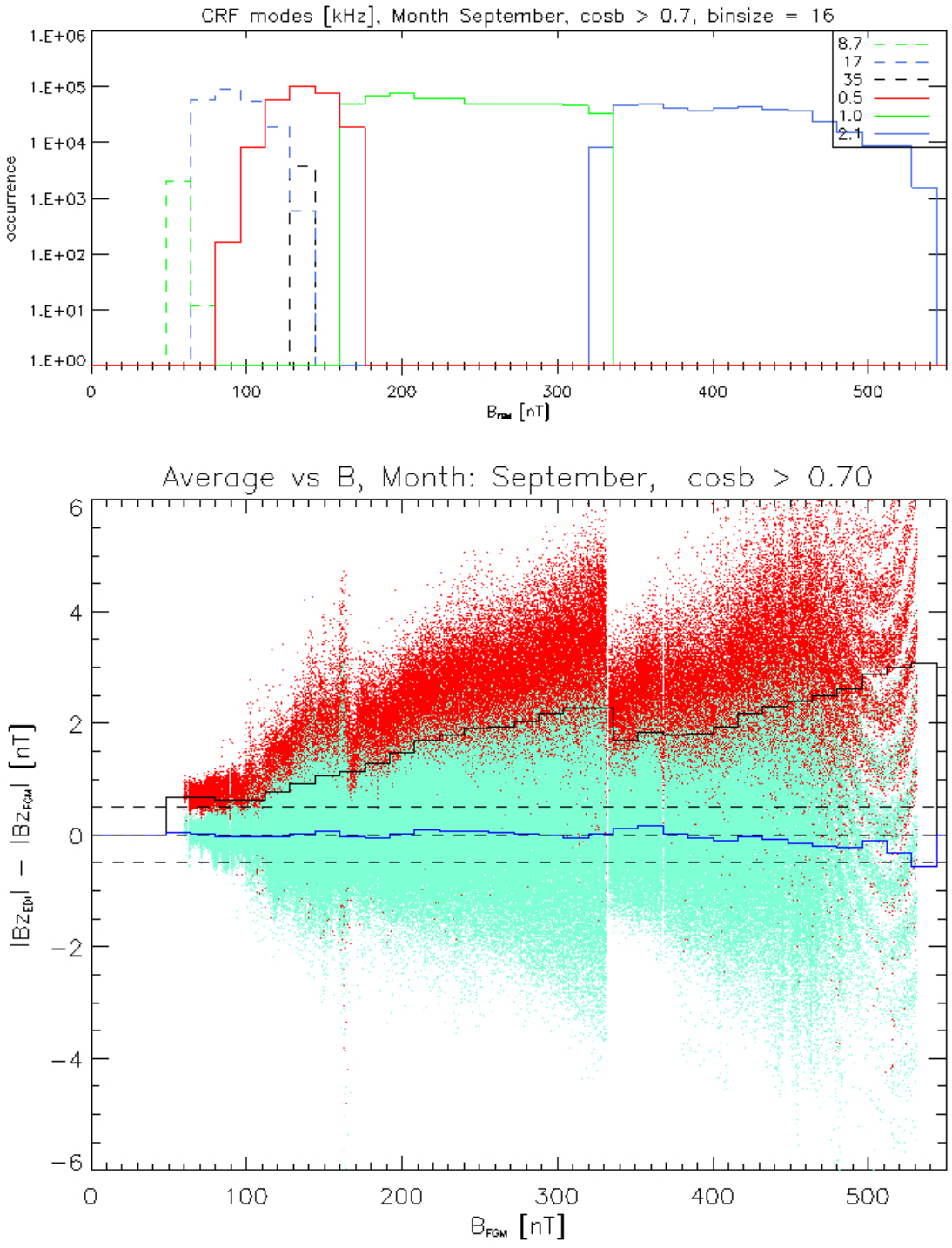


**Figure 2.11:** Calibration of the month of September in 2003.
(u) Occurrence of the different modes of the EDI in respect to the magnetic field measured by the FGM.
CRF modes: mode 2 = 8.7 kHz, mode 3 = 17 kHz, mode 4 = 35 kHz, mode 5 = 0.5 kHz, mode 6 = 1.0 kHz, mode 7 = 2.1 kHz.
(l) Comparison of the original data (red) and the calibrated data(cyan). The black line (original data) and the blue line (calibrated data) show the averaged difference of the used bins.

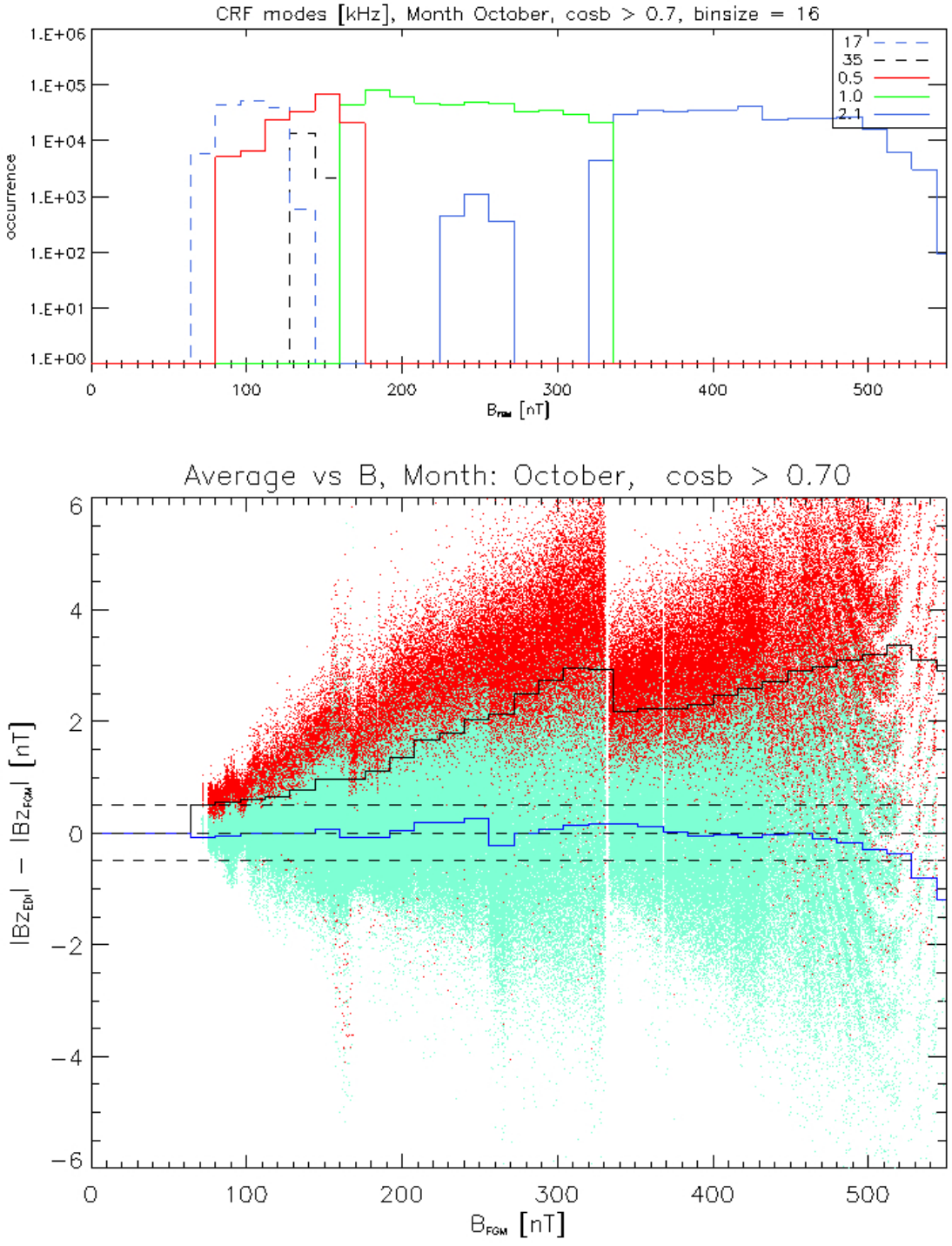


**Figure 2.12:** Calibration of the month of October in 2003.
(u) Occurrence of the different modes of the EDI in respect to the magnetic field measured by the FGM.
CRF modes: mode 3 = 17 kHz, mode 4 = 35 kHz, mode 5 = 0.5 kHz, mode 6 = 1.0 kHz, mode 7 = 2.1 kHz.
(l) Comparison of the original data (red) and the calibrated data(cyan). The black line (original data) and the blue line (calibrated data) show the averaged difference of the used bins.

### 2.1.7 Calibration (Orbit)

In addition to the calibration of a whole month the calculation of offsets can be applied to a series of orbits. This leads to the characterisation of the temporal evolution of the different offsets. Because of the exceptional quality of the August dataset orbits were only considered of this month. Naturally, the method can be applied to other orbit series too. As numerously mentioned throughout this thesis the EDI measurements can not be done continuously. Therefore, data of an orbit is only available during phases in which measurements are conducted. In general, a data along a full orbit does not exist. The duration of the orbits is provided by NASA website [14]. As an example Figure 2.13 depicts one orbit. Furthermore, the orbit is shown from all three directions in GSE (geocentric solar ecliptic) coordinates. In the case of this Figure the orbit illustrated is from the Cluster 2 satellite (August, 12th, 2003). Because the satellites move in formation the orbit also applies for the Cluster 1 satellite. In the header of Figure 2.13 the starting and the ending time of the specified orbit is stated. For every single orbit in the examined orbit series these times are taken from the corresponding Figures provided on the website. Hence the duration of the orbit is obtained.

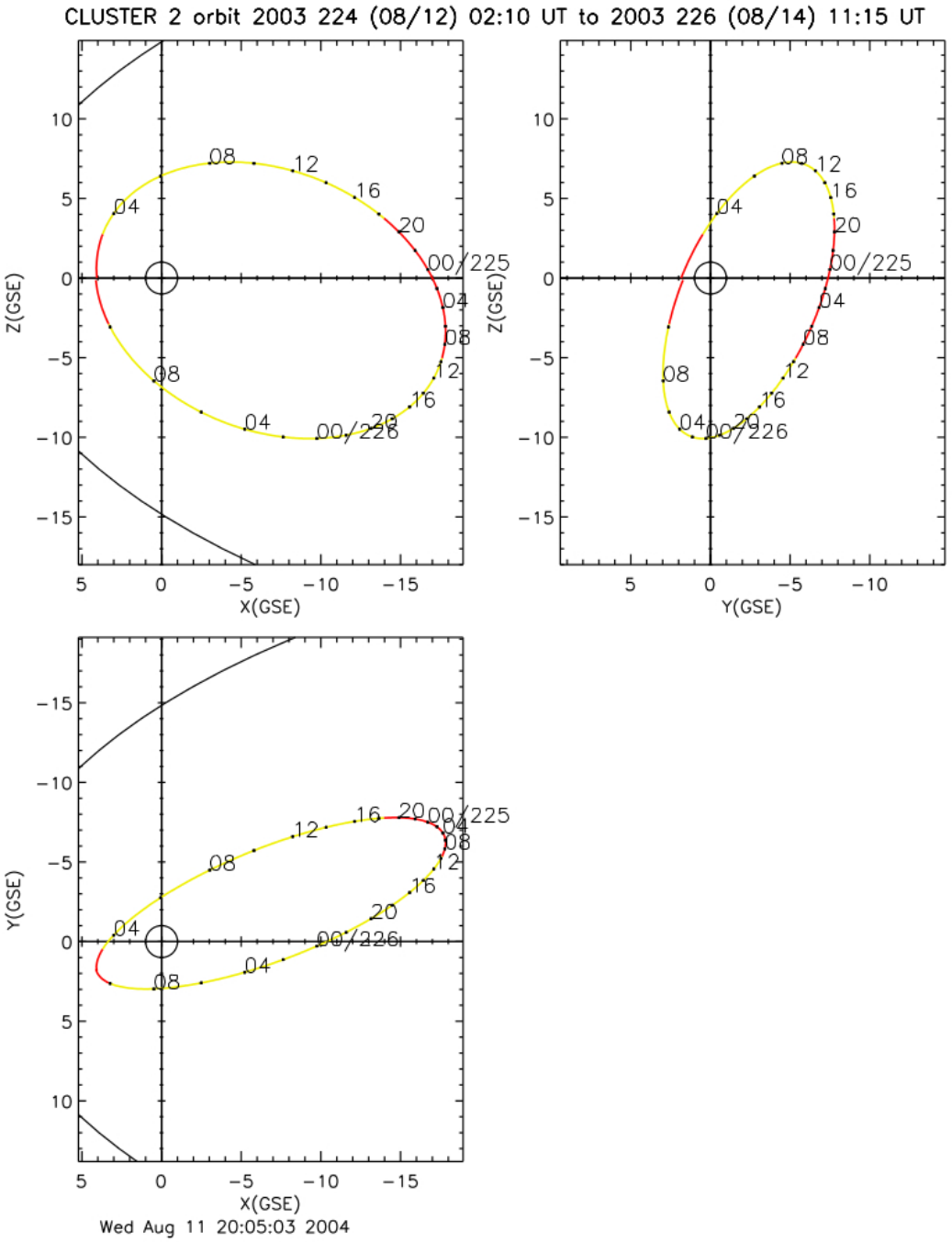


**Figure 2.13:** Orbit data for August, 12th, in 2003 for Cluster 2 [14].

In the next step the temporal evolution of the spin-axis offsets (FGM) and the different modes (EDI) are determined. In comparison to the datasets of a whole month not all modes are present at each orbit. Because the calculations are based on the considerations of different magnetic field regions and their interactions, some compromises have to be made. If there is no data for the low-field region to calculate the spin-axis offset, the spin-axis offset of the previous orbit is used for further calculations. Because of the

importance of the spin-axis offset this can be done, but the same thing does not apply to the values of the different modes. Modes in the mid- or high-field regions can be calculated as long as the spin-axis offset is known. As already stated for the monthly calibrations the dataset has to be corrected for the spin-axis offset to do any calculations for the different modes.
In the upper part Figure 2.14 the temporal evolution of the spin-axis offsets for magnetic field magnitudes below and above 256 nT is depicted. In this Figure the violet data points connected by a line represent the lower field spin-axis offset. The values of that spin-axis offset are plotted according to their orbit number. Not every orbit has a value for that offset. This is because of the previously mentioned absence of the data in those orbits. As for the evolution of this value the deviation is roughly in the range of the monthly calculated value. The blue data points represent the higher spin-axis offset plotted against their orbit number. Here one can see that there is sufficient data for every single orbit to calculate the offset. The values for the spin-axis offset in the higher field region vary strongly. Because of the previous considerations concerning the accuracy of the calculations in the high field done for the monthly calculations this variation was expected (see section 2.1.5). In the lower part of Figure 2.14 the occurrence of the data used for the calculation at each single orbit is depicted. Again the violet line represents the lower field spin-axis offset, whereas the blue line represents the higher field spin-axis offset.
The temporal evolution of the different modes (time of flight offsets) is also examined. For simplicity only three of the modes are used for the analysis. In the upper part of Figure 2.15 the modes of the following regions are depicted: R2, R5 and R6. The first mode, R2, is of the lower field region. In this field region the mode can be calculated, but because of the considerations made in the section 2.1.5, the value of the mode is strongly error-prone. This leads to a variation of the value over the whole orbit series. As for the spin-axis offset in the lower field region, the data for the mode of R2 is also limited. Therefore, it is not possible to calculate a value for that mode at every single orbit. The value of the mode can only be calculated if there is a corresponding value of the spin-axis offset. The two modes in the regions R5 and R6 are in the higher field region. Both values show a steady temporal evolution and have a small deviation. In the lower part of Figure 2.15 the occurrence of the data used for the calculation is depicted. One can see that the mode of the region R2 has much less data as the two other modes. Even though there are some variations in the occurrence this has no impact on the values of the modes R5 and R6. In section 2.1.5 it is shown that the modes calculated in the higher regions are of higher accuracy. This is obvious if one considers Figure 2.15.

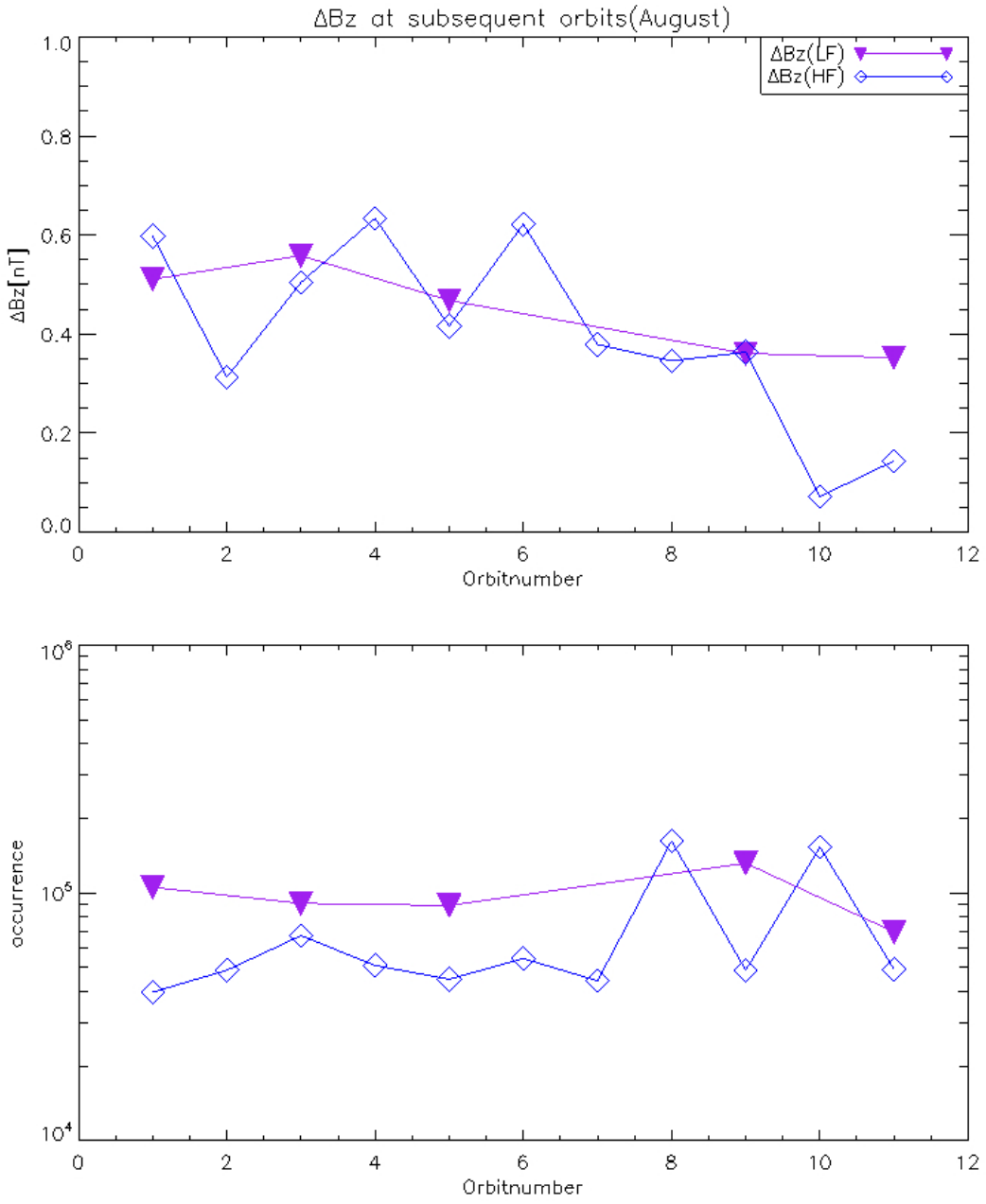


**Figure 2.14:** Temporal evolution of the spin-axis offsets (11 orbits).
(u) Values of the two spin-axis offsets (LF = low field, HF = high field) of an orbit series.
(l) Occurrence of the data used for the calculation of the two spin-axis offsets.

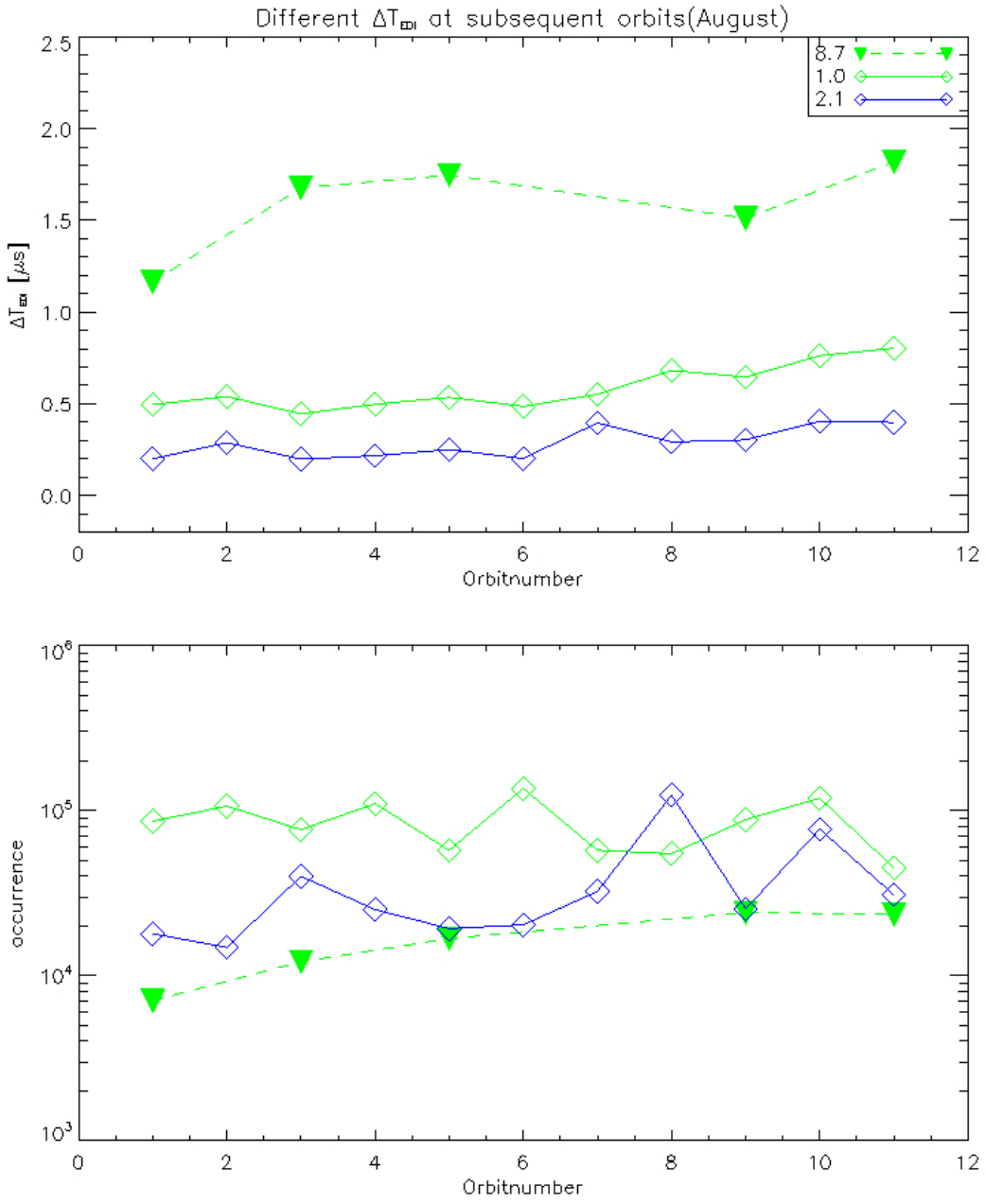


**Figure 2.15:** Temporal evolution of the different modes(EDI) (11 orbits). (u) Values of three EDI modes (CRF modes) of different regions (R2, R5, R6) of an orbit series (mode 2 = 8.7 kHz, mode 6 = 1.0 kHz, mode 7 = 2.1 kHz). (l) Occurrence of the data used for the calculation of the three modes.

## 2.2 Summary

To ensure the proper operation of any instrument onboard a satellite a continuous examination for error sources is vital. Some errors can be corrected at a preflight calibration, others have to be considered in space. For the Fluxgate-Magnetometer (FGM), one of the 11 instruments onboard the Cluster satellites, several procedures for inflight calibrations have been taken. The main emphasis of this master thesis is the calibration of the spin-axis offset of the FGM. It is acknowledged that the data used for the calibration is already pre-calibrated for several other error sources (see section 1.3.3.2, paragraph 1.3.3.2). In this thesis the calibration is done by using the data of another instrument onboard the Cluster satellite, the Electron Drift Instrument (EDI). The EDI can measure an absolute value of the ambient magnetic field (see section 1.3.3.1, paragraph 1.3.3.1). By comparing the two magnetic fields measured by the FGM and the EDI the spin-axis offset can be calculated. Normally, the spin-axis offset can by calculated by using Alfven waves in the solar wind. This is only applicable if the satellite is crossing into the interplanetary space along its orbit. Therefore, the method described in this thesis will be interesting for the upcoming MMS mission (see section 1.3.4).
The dataset of the FGM used in this master thesis is pre-calibrated. Those calibrations are done for every processed day. Therefore, the calibration scheme is called daily-calibrations. During the thesis an additional errors came up. The measurement of the magnetic field done by the EDI is based on a time measurement. Depending on the magnetic field strength there are several different sensitivities of the EDI. Each sensitivity of the time measurement has its own error. In general this leads to two different kind of errors. One is the spin-axis of the FGM and the other is the result of the time measurement of the EDI. In the section 2.1.2 and section 2.1.3 these errors are discussed in greater detail.
One other thing that has to be considered is the mutual interaction of the spin-axis offset and the time measurement offset (error). In section 2.1.4 the interaction of the offsets is examined. The accuracy with which the two offsets can be calculated differs by the examined magnetic field magnitude. For magnetic field magnitudes less than 100 nT the spin-axis offset can be calculated quite good. The time measurement offset on the other hand cannot be determined sufficiently at these magnetic field magnitudes. At higher magnitudes the situation is reversed. In the next step the calculations of both offsets are done. This part can be found in section 2.1.5. Here the spin-axis offset and the different time measurement offsets are determined. Because each of the two kinds of offsets can only be calculated precisely at different magnetic field magnitudes, the considered magnetic field range is divided into three separate regions: low-field region, mid-field region and high-field region. For every region one has to apply individual considerations to calculate the desired offsets. In the paragraph 2.1.5 of section 2.1.5 the values of the spin-axis offsets and the time measurement offsets are presented. Here, calculations for the following four months of 2003 are depicted: July, August, September and October. The calculated values for these four months were used to calibrate the original data.

In section 2.1.6 the calibration of the four months is discussed. For every month the original data is plotted with the calibrated data to depict the difference resulted by the calibration.
In section 2.1.7 the calibration method was used to examine the temporal evolution of the spin-axis offsets and the time measurement offsets. The calibration was applied on 11 consecutive orbits of the month of August (2003). Finally, it must be said that the applied method to calibrate the two different kinds of offsets result in a successful enhancement of the original data, despite that some parts in the monthly calibrations still show a deviation that could not be corrected by the application of this method. Therefore, further examinations and considerations for additional error sources must be made.

# Appendix A

# Appendix

Cross product algebraic relation:

- $\mathbf{A} \times (\mathbf{B} \times \mathbf{C}) = (\mathbf{A} \cdot \mathbf{C})\mathbf{B} - (\mathbf{A} \cdot \mathbf{B})\mathbf{C}$

Programs:

- calibration_main: This program is the main file for the calibration process. There are four variables that have to be specified at start. The first variable is called ormo. If ormo is set to '1' the monthly calibration is done. If ormo is set to '0' the orbit series calculation is performed. The second variable is only used in the program if the orbit series is chosen. The value of this variable defines a specific orbit to be calculated. This is an optional case. The third variable is set for the case of the monthly calibration. This value defines the month for the calibration. The year cannot be changed and is set to 2003. The months are defined as follows: July ('0'), August ('1'), September ('2') and October ('3'). The last variable defines, which calibration scheme is use: daily calibration or caa calibration. In this thesis the daily calibration scheme was used. After choosing the four variables the data is loaded accordingly and pre-prepared for the usage in the programs: 'calibration_month' and 'calibration_orbit'. Furthermore, the data passed along to those two programs is also saved to a file.

- calibration_month: In this program the calibration is done for the specified month chosen in 'calibration_main'. Twelve variables are passed to this program. They are as follows: (1) the x-component of the magnetic field measured by the FGM (array) , (2) which GDU is used (array), (3) TOF data (array), (4) the magnetic field measured by the FGM (array), (5) the x-component of the magnetic field calculated with the TOF data (array), (6) the y-component of the magnetic field measured by the FGM (array), (7) the z-component of the magnetic field measured by the FGM (array), (8) the magnetic field calculated with the TOF data (array),

(9) sigma values of the TOF measurement (array), (10) time of the FGM measurements (array), (11) orbit index (single), (12) month index (single). Using the data provided by the main program the calculation of the offsets and the following calibration can be done. In this program the calibration is done according to the described procedure in section 2.1.5.

- calibration_orbit: The same variables, which were stated for the program 'calibration_month' are used passed to this program. In contrast to 'calibration_month' the calculations for the different offsets are done for each orbit. The program is written to do a specified orbit series defined at the beginning of the 'calibration_main' program. The calculated values of each orbit are stored in a file. This data can be used to plot the evolution of the offset values by using the program 'display_mode'.

- crf_const: Three variables have to be passed to this program: (1) dataset of the sigma values (correspond to CRF values, array), (2) the time of the FGM measurements (array), (3) different sigma elements (correspond to CRF elements, array). The program corrects the passed data for the previously mentioned oscillations that can be observed in the plot CRF-values versus FGM time (see section 2.1.3). The program returns the dataset, wherein the parts of the oscillations have been removed. The return variable is a corrected array, which contains the indices of the dataset without the oscillation elements.

- display_mode: This program is used to plot the orbit series calculated by the program 'calculation_orbit'. In the current state of the program there is only one variable that has to be passed to it. A variable that defines the month which is used for the calculation. In this case only the month of August can be plotted. To display the calculated data the data is loaded from the file. Afterwards the data is plotted accordingly.

- mode_filtering: Four variables have to be passed to this program: (1) the magnetic field measured by the FGM (array), (2) indices of the different sigma values (CRF values) in the sigma array (pointer array), (3) different sigma elements in the sigma array (CRF elements) (small array), (4) indices of the elements, which fulfil the $\cos b$ condition (array). This program filters the dataset according to the different sigma values (CRF values) and return four variables: (5) indices of elements in the low field corresponding to a certain sigma value (CRF value, pointer array), (6) indices of elements in the high field corresponding to a certain sigma value (CRF value, pointer array), (7) marker for low field sigma value (CRF value, pointer array), (8) marker for high field sigma value (CRF value, pointer array). The marker remark if there is a certain sigma value (CRF value) or not. By using this program the dataset is broken down to the different sigma value (CRF value) datasets.

# Bibliography


[1] ESA/NASA SOHO/LASCO/EIT. Coronal mass ejections sometimes reach out in the direction of earth. Website, February 2003. Available online at http://spaceinimages.esa.int/var/esa/storage/images/esa_multimedia/images/2003/02/coronal_mass_ejections_sometimes_reach_out_in_the_direction_of_earth/9851895-3-eng-GB/Coronal_mass_ejections_sometimes_reach_out_in_the_direction_of_Earth.jpg — visited on May 14th 2013.

[2] Alexander Piel. *Plasma Physics: An Introduction to Laboratory, Space, and Fusion Plasmas*. Springer-Verlag Berlin Heidelberg, 2010.

[3] Wolfgang Baumjohann and Rudolf A. Treumann. *Basic Space Plasma Physics*. Imperial College Press, 516 Sherfield Building, Imperial College London, 1996.

[4] Arturo Ortiz Tapia. Magnetic reconnection. Website, 2005. Available online at http://www.aldebaran.cz/astrofyzika/plazma/reconnection/reko.gif — visited on February 22th 2013.

[5] European Space Agency. Cluster earth. Website, 2006. Available online at http://esamultimedia.esa.int/images/Science/Clusters_Earth2.jpg — visited on February 22th 2013.

[6] Max-Planck-Institut für extraterrestrische Physik (MPE). Edi: Instrument description. Website, 2004. Available online at http://www.mpe-garching.mpg.de/CLUSTER/Bilder/EDI_Charts1_162.jpg — visited on February 27th 2013.

[7] Max-Planck-Institut für extraterrestrische Physik (MPE). Edi: Instrument description. Website, 2004. Available online at http://www.mpe-garching.mpg.de/CLUSTER/Bilder/GDU1_LW0_klein.jpg — visited on February 27th 2013.

[8] E.Georgescu and the EDI Team. Cluster active archive: Interface control document for edi, April 2012. Document Number: CAA-EDI-ICD-0203 — page 9.

[9] G. Paschmann et al. The electron drift instrument for cluster. *Space Science Reviews*, 79:233–269, 1997.

[10] H.Lewtas, C.Carr, E.Lucek, P.Brown, L.-N.Alconcel, and T.Oddy. User guide to the fgm measurements in the cluster active archive(caa), May 2012. Document Number: CAA-EST-UG-FGM.

[11] H.Lewtas, C.Carr, E.Lucek, P.Brown, L.-N.Alconcel, and T.Oddy. Calibration report of the fgm measurements in the cluster active archive(caa), May 2012. Document Number: CAA-EST-CR-FGM.

[12] NASA MMS. Promotional material: Magnetospheric multiscale (mms) decal. Website, 2013. Available online at http://mms.gsfc.nasa.gov/images/promotional_materials/mms_logo_hi-res.jpg — visited on July 12th 2013.

[13] R. Nakamura, F. Plaschke, R. Teubenbacher, L. Giner, W. Baumjohann, W. Magnes, M. Steller, R. B. Torbert, H. Vaith, M. Chutter, K.-H. Fornaçon, K.-H. Glassmeier, and C. Carr. Inter-instrument calibration using magnetic field data from flux gate magnetometer (fgm) and electron drift instrument (edi) onboard cluster. *Geoscientific Instrumentation, Methods and Data Systems Discussions*, 3(2):459–487, 2013. doi: 10.5194/gid-3-459-2013. URL http://www.geosci-instrum-method-data-syst-discuss.net/3/459/2013/.

[14] NASA. Themis-a mp crossing survey plots. Website, 2013. Available online at http://cdaweb.gsfc.nasa.gov/cgi-bin/gif_walk — visited on July 26th 2013.

[15] H.Vaith et al. Electron gyro time measurement technique for determining electric and magnetic fields. *Geophysical Monograph*, 103, 1998.

[16] E.Georgescu et al. Use of edi time of flight data for fgm calibration check on cluster. *ESA Sp*, 598, 2006. Proceedings Cluster and Double Star Symposium - 5th Anniversary of Cluster in Space(Noordwijk, The Netherlands, 19 - 23 Sept. 2005).

[17] Helmut Zimmermann and Alfred Weigert. *Lexikon der Astronomie (8. Auflage)*. Spektrum Akademischer Verlag Heidelberg Berlin, 1999.

[18] Margaret G. Kivelson and Christopher T. Russell. *Introduction to Space Physics*. Cambridge University Press, The Pitt Building, Trumpington Street Cambridge, 1995.

[19] M.A. Hapgood. Space physics coordinate transformations: A user guide. *Planetary and Space Science*, 40:711–717, 1992. No.5.

[20] Wikipedia. Cluster ii (spacecraft). Website, February 2013. Available online at http://en.wikipedia.org/wiki/Cluster_II_(spacecraft); visited on February 22th 2013.

[21] C.P. Escoubet, M. Fehringer, and M. Goldstein. Introduction: The cluster mission. *Annales Geophysicae*, 19(10/12):1197–1200, 2001. Available online at http://www.ann-geophys.net/19/1197/2001/angeo-19-1197-2001.pdf — visited on February 22th 2013.

[22] European Space Agency. Cluster mission: Summary. Website, December 2012. Available online at http://sci.esa.int/science-e/www/object/index.cfm?fobjectid=31258 — visited on February 22th 2013.

[23] European Space Agency. Cluster mission: Fact sheet. Website, December 2012. Available online at http://sci.esa.int/science-e/www/object/index.cfm?fobjectid=31262 — visited on February 22th 2013.

[24] E.Georgescu and the EDI Team. User guide to the edi measurements in the cluster active archive(caa), April 2012. Document Number: CAA-EST-UG-EDI.

[25] Harald Jeszenszky. User guide to the aspoc measurements in the cluster active archive(caa), February 2009. Document Number: CAA-EST-UG-ASP.

[26] N.Cornilleau-Wehrlin, Yvonne de Conchy, and Rodrigue Piberne. User guide to the staff measurements in the cluster active archive(caa), October 2012. Document Number: CAA-EST-UG-002, updated Version 3.2 (Authors updated previous Version).

[27] Per-Arne Lindqvist, Chris Cully, Yuri Khotyaintsev, and the EWF team. User guide to the efw measurements in the cluster active archive(caa), May 2012. Document Number: CAA-EST-UG-EFW.

[28] S.Walker and K.Yearby. User guide to the dwp measurements in the cluster active archive(caa), November 2011. Document Number: CAA-EST-UG-DWP.

[29] J.G.Trotignon, X.Vallieres, and the WHISPER team. User guide to the whisper measurements in the cluster active archive(caa), April 2011. Document Number: CAA-EST-UG-WHI.

[30] Jolene S.Pickett, Roxane M.Mitten, Ivar W.Christopher, and Joanne M.Seeberger. User guide to the wbd measurements in the cluster active archive(caa), May 2012. Document Number: CAA-EST-UG-WBD.

[31] A.N.Fazakerley and the PEACE Operations Team. User guide to the peace measurements in the cluster active archive(caa), May 2012. Document Number: CAA-EST-UG-PEA.

[32] I.Dandouras, A.Barthe, and the CIS Team. User guide to the cis measurements in the cluster active archive(caa), May 2012. Document Number: CAA-EST-UG-CIS.

[33] Patrick W.Daly and Elena A.Kronberg. User guide to the rapid measurements in the cluster active archive(caa), May 2012. Document Number: CAA-EST-UG-RAP, updated Version 3.1.

[34] A. Balogh et al. The cluster magnetic field investigation: overview of in-flight performance and initial results. *Annales Geophysicae*, 19:1207–1217, 2001.

[35] Hannes Karl Leinweber. *In-flight Calibration of Space-borne Magnetometers*. PhD thesis, Graz University of Technology, Graz, December 2011.

[36] European Space Agency. The cluster active archive goes online. Website, February 2006. Available online at http://sci.esa.int/cluster/38705-the-cluster-active-archive-goes-online/; visited on July 10th 2013.

[37] N.A. Tsyganenko. Magnetospheric magnetic field model with a warped tail current sheet. *Planetary and Space Science*, 37:5–20, 1989.